ROBUST STATISTICAL INFERENCE IN HUMAN BRAIN MAPPING

By

XUE YANG

Dissertation
Submitted to the Faculty of the
Graduate School of Vanderbilt University
in partial fulfillment of the requirements
for the degree of

DOCTOR OF PHILOSOPHY
in
Electrical Engineering
December, 2013
Nashville, Tennessee

Approved:
Professor Bennett A. Landman
Professor Benoit Dawant
Professor Hakmook Kang
Professor Victoria L. Morgan
Professor Richard A. Peters
Professor Jack H. Noble

ACKNOWLEDGEMENTS

My graduate study at Vanderbilt is a very special experience for me for both academic life and personal life. First, I am like to express my greatest thank to my advisor Professor Bennett Landman. Thank you for your mentoring from baby step coding to scientific inspirations. I am impressed by his positive attitudes towards research and helping people. Secondly, I would like to thank my lab members for their help in my research and presentation skills development. Thank you all for learning my presentations again and again. Andrew Asman, thank you for your help on a lot of computer issues. Carolyn Lauzon, thank you for helping me in scientific writing. Thank you Benjamin Yvernaut and Brian Byod, for helping me figure out a lot of XNAT issues. I would like to express my acknowledgements to my collaborators. Thank you Professor Hakmook Kang, for explaining complex statistical theories patiently and kindly help in my job searches. Thank you Professor Victoria Morgan, Allen Newton, Martha Holmes, and Robert Barry for your teach in clinical applications. I also like to thank our collaborators in Johns Hopkins professor Caffo and Professor Crainiceanu in helping me with biostatistics theories and collaborator in NIH Professor Lori Beason-Held and Professor Susan M. Resnick for providing us beautiful datasets.

For my personal life here, I want to thank my parents for their support. They always encourage me to pursue my dream. Thank you mom and dad, I am sorry I have to be more than eleven thousand miles away from you; I always hope to be your proudness. I like to thank my boyfriend Fei Han for always be on my side and bring me happiness. I always feel lucky and thankful to meet you and find my Mr. Right. I also like to express my thanks to my best roommate Jia Bai and all my friends in Vanderbilt. I will never forget the joy we shared together and the time we help each other.

TABLE OF CONTENTS

Page

Chapter

LIST OF TABLES

Table Page

LIST OF FIGURES

LIST OF ABBREVIATIONS

AR	autoregressive
AUC	area under curve
BLSA	Baltimore Longitudinal Study on Aging
BnPM	biological non-parametric mapping
BPM	biological parametric mapping
CNR	contrast to noise ratio
CT	computed tomography
EC	Euler characteristic
FDR	false discovery rate
fMRI	functional magnetic resonance image
FN	false negative
FNR	false negative rate
FOV	field of view
FP	false positive
FPR	false positive rate
FWE	family-wise error
FWER	family-wise error rate
FWHM	full width at half maximum
GLM	general linear model
GM	gray matter
GUI	graphical user interface
LH	left hippocampus
LMS	least median of squares

MC	Monte Carlo
MRI	magnetic resonance image
NMR	nuclear magnetic resonance
OLS	ordinary least squares
PCA	principle component analysis
PET	positron emissions tomography
rBPM	robust biological parametric mapping
RC	regression calibration
ReML	Restricted Maximum Likelihood
RFT	random field theory
RMSE	root mean squared error
ROC	receiver operating characteristic
ROI	region of interest
rRMSE	relative root mean squared error
rs-fMRI	resting state functional magnetic resonance image
SIMEX	SIMulation and EXtrapolation
SnPM	statistical non-parametric mapping
SNR	signal to noise ratio
SPM	statistical parametric mapping
TE	echo time
TN	true negative
TP	true positive
TR	repetition time
VBM	voxel-based morphometry

CHAPTER I

INTRODUCTION

Overview

Structure-function relationships in the human brain provide core insights for disease detection, prevention, and our overall understanding of the brain. Mapping the quantitative relationship between structure and function in the human brain is an important and challenging problem. Researchers have already demonstrated many important micro- and macroscopic structure-function correlations in the brain. (Luerding, Weigand et al. 2008) proved the frontal and anterior cingulate cortex were correlated to working memory performance. The correlations of structural and functional brain changes were established (Jensen, Srinivasan et al. 2013). Brain structures corresponding to mental illness were widely studied (Kaufman and Charney 2001; Antonova, Sharma et al. 2004). While it is undisputed that structure shapes neural dynamics in the human brain, the quantitative causality and specific correlations are unclear (Honey, Thivierge et al. 2010). Numerous volumetric, surface, regions of interest and voxelwise image processing techniques have been developed to statistically assess potential correlations within and between imaging and non-imaging data.

Massively univariate regression and inference in the form of the general linear model (GLM) have transformed the way in which multi-dimensional imaging data are studied. Statistical Parametric Mapping (SPM) is a voxel-wise image analysis approach, through the use of statistical tests, enables exploration of responsible hypotheses without knowing where the responses would occur (Friston, Holmes et al. 1994). SPM was limited to single modality regression with imaging data represented only in the regressand until the extension Biological Parametric Mapping (BPM) was developed to enable multi-modality regression, allowing for imaging data to use considered for both regressors and regressand (Bookstein 2001; Casanova, Srikanth et al. 2007). These models offer great promise for direct, voxelwise assessment of structural and functional relationships with multiple imaging modalities. However, the assumptions in the traditional statistical approaches used in neuroimaging are strict, which hinder the validity of inferences on large (potentially ill-controlled) imaging datasets. Largely, the imaging outliers, artifacts, measurement error and the spatial correlations are not taken into account in current statistical methods commonly used in the imaging community, which may lead to invalid inferences (e.g., artifactual low p-values) due to slight mis-registration or variation in anatomy between subjects (Yang, Beason-Held et al. 2011). Additionally, when the imaging noise/artifact distributions are challenging to characterize (e.g., 7T fMRI), the quantitative *empirical* validation remains elusive *in vivo* as the true connectivity patterns are unknown, which makes it harder to apply an appropriate statistical method.

To enable widespread application of statistical investigations with multiple modality images, we introduced robust regression and non-parametric regression in the neuroimaging context of application of the general linear model (Yang, Beason-Held et al. 2011). Through simulation and empirical studies, we demonstrated that our robust approach reduces sensitivity to outliers without substantial degradation in power. For more realistic multi-parametric assessment (i.e., imaging modalities are used as regressors), distributional consideration of all observations is appropriate. We demonstrated a method for full consideration of observation variability within the confines of a design matrix paradigm and showed how to consider simultaneous treatment of parameters with measurement error alongside traditionally defined fixed parameters (Yang, Lauzon et al. 2012). To access the quantitative performance of robust modern statistics versus the traditional methods on empirical ultra-high field dataset, we turn to the recent innovations in capturing finite sample behavior of asymptotically consistent estimators (i.e., SIMulation and EXtrapolation - SIMEX) that have enabled direct estimation of bias given single datasets. In contrast to increasing noise, we leverage the theoretical core of SIMEX to study the properties of inference methods in the face of diminishing data.

In this dissertation, we proposed robust statistical estimation, model consideration and quantitative evaluation addressing the challenging issues in human brain mapping. To deal with the potential outlier problems we introduced robust and non-parametric mapping in the context of human brain structure-function relationships in **Chapter II.** Further consideration of the structure function relationships analysis indicates in many cases the measurement errors of the explanatory imaging variables cannot be ignored. In **Chapter III**, we derived the Model II regression method in the general linear model framework and implemented it as well as regression calibration in the multi-modality image mapping. **Chapter IV** focuses on the evaluation of inference methods where the truth is unknown. In functional connectivity analysis, the temporal correlations are well modeled but the spatial correlations are ignored in estimation most of the time. In **Chapter V**, we extended a spatio-spectral for ROI-based resting sate functional connectivity analysis and proposed an alternative voxel-wise spatio-temporal model within the SPM framework. An empirical study on structure function relationship using multi-site large scale data was explored in **Chapter VI** with mega-analysis and meta-analysis. The overall impact and perspective of this dissertation were concluded in **Chapter VII**.

Terminology

A **response variable** mentioned here refers to the intensity of a voxel in a brain image. The **explanatory variables** are factors used in explaining the response variable. They can be any experiment measured scalar or indicated variables such as age, sex, and voxel intensity from brain images of interest. A statistical **model** (e.g., general linear model) is an equation we use to explore the relationships between the response variable and the explanatory variables. An **error** term in a model is the part of the response variable that cannot be explained in the statistical equations. A **residual** is the distance between the observed value and the value given by the equation for an observation. A statistical **test** is a method of making inference about a null hypothesis (e.g., a explanatory variable has no effects on the response variable) from the data.

The symbol $\sim$ is used to note “distributed as,” with $\mathcal{N}$ used to represent the multivariate Normal distribution. The hat ($\widehat{\ }$) indicates an estimated value of a random variable and “$\top$” indicates transpose.

NeuroImage Data

Brain Imaging

Medical imaging has provided powerful insights into understanding the structural and functional architecture of human anatomy and is widely used for the diagnosis, intervention, and management of clinical disorders. With modern study designs, it is possible to acquire multi-modal three-dimensional assessments of the same individuals — e.g., structural, functional and quantitative magnetic resonance imaging, alongside functional and ligand binding maps with positron emission tomography. Magnetic resonance imaging (MRI) and positron emission tomography (PET) are used as primary brain imaging modalities in this dissertation work. Computed tomography (CT), which also produces tomographic images, will not be discussed here.

MRI measures the magnetic field generated by nuclear spins (hydrogen in water). Based on the property of nuclear magnetic resonance (NMR), magnetic nuclei in a magnetic field absorb and re-emit electromagnetic radiation. The process that nuclear magnetization prepared in a non-equilibrium state return to the equilibrium distribution is relaxation. Two principal relaxation processes, T1 and T2, refer to the relaxation of the nuclear spin magnetization vector parallel and perpendicular to the external magnetic field, providing contrast between different brain tissues. In brief, MRI makes use of the property of NMR, measures the spin relaxation rates to generate T1-weighted or T2-weighted structure brain images.

PET is a nuclear medicine imaging technique that shows functional activity by measuring the concentrations of a radioactive tracer. An analogue of glucose is a commonly used tracer. If a tissue is activated, it will take more glucose so that the concentration of glucose there increases. Thus, the concentrations of glucose reflect tissue metabolic activity that areas of high radioactivity are associated with brain activity.

Functional MRI (fMRI) is an MRI procedure that detects the change in blood flow, mapping neural activity in the brain. The procedure is similar to MRI but uses blood oxygen-level-dependent

(BOLD) contrast. When neurons become active, local cerebral blood flow to those brain regions increases leading oxygen saturation increases locally. Therefore, the change in blood flow (hemodynamic response) relates to energy used by brain cells.

Preprocessing

Before statistical analysis using brain imaging data, image preprocessing steps should be applied. These include segmentation, normalization and smoothness for structure MRI and PET. For fMRI the standard preprocessing steps are slice timing correction, temporal filtering, realignment, normalization and smoothness.

- Segmentation can classify structural brain MRI into different brain tissue classes. If we are only interested in a specific brain tissue, gray matter (GM) for example, we can segment the structure MRI to acquire GM images.
- Normalization is a method of transforming every subject's brain image into the same shape and the same space using affine or non-linear registration. Normalization algorithms work by minimizing/maximizing a difference/similarity matrix (e.g., sum of squares, correlation ratio, normalized mutual information) between the source brain images and the template images (Ashburner and Friston 1999).
- Smoothness refers to spatial smoothing in neuroimaging. It applies a Gaussian kernel of a specified width, convolving image volume. The effects are blurring the image, softening the hard edges, lowering the overall spatial frequency, and improving image signal-to-noise ratio. Usually, smoothness should be applied after normalization to blur unmatched clusters and thus maximize the overlap between subjects.
- In fMRI, the sample signals at different layers of the brain are in fact acquired at different time points. Slice timing correction interpolates between the sample points, gives the

correct time course that you should get if every voxel is sampled at exactly the same time (Van de Moortele, Cerf et al. 1997).

- Temporal filtering is used to remove temporal noise. High-pass filter can remove linear drifts from a time course while low-pass filter can improve the temporal signal-to-noise ratio.
- Realignment which is also called motion correction mainly aims to remove movement artifacts causing by the move of the subject during the acquisition time (Friston, Williams et al. 1996). Realignment algorithms realign every image time series within single subject to the reference scan through rigid registration, maintaining that the same voxels across time always represent the same location.

This dissertation is not about any new image processing methods but focuses on the statistical interpretations. The image preprocessing methods mentioned above are widely studied and can be applied before statistical analysis aiming to provide clean and clear imaging data.

General Linear Model in Brain Image

The study of brain activation through imaging changes was made possible in 1980s with brain regional differences characterizing by hand-drawn regions of interest (ROI) (Fox, Mintun et al. 1986). Later, the idea of making voxel-specific statistical inferences without predefined ROI emerged and the first statistics map was used in (Lueck, Zeki et al. 1989). The underlying voxel-by-voxel (pixel-by-pixel) statistical inference methodology contributes to the test of hypothesis about regionally specific effects of the explanatory variables (Friston, Frith et al. 1990), introducing statistical parametric mapping (SPM). Then, the problem within statistical test at each voxel was realized and solved through the technology of topological inference introduced in (Worsley, Evans et al. 1992) using random field theory. In the 1990's, many landmark papers were published using PET, and SPM had become the standard method for analyzing PET activation studies in the community (e.g., (Grady, Maisog et al. 1994)). The first presentation of results from fMRI emerged in 1992 by Jack Belliveau at the annual meeting of the Society of Cerebral Blood Flow. FMRI studies were not widely accepted in their early ages because of the challenging theoretical issues. One important problem is about how to model evoked haemodynamic responses in fMRI time-series. This has been resolved by using convolution models following empirically derived haemodynamic responses (Friston, Jezzard et al. 1994). The time serial correlations problem in fMRI was another important issue that attracted much research interest until the solution arrived in (Worsley and Friston 1995). The development of the techniques is still on going and now the approaches using maximum likelihood and empirical Bayes are widely accepted (Friston, Penny et al. 2002). When it turns to make inferences about the population effects in fMRI, the condition is different from PET analysis that requires hierarchical models. Holmes and Friston introduced a hierarchical level analysis which performs a second-level analysis using subject-specific effects estimated in a first-level analysis (Holmes and Friston 1998).

The general linear model (GLM) is an equation that explains the observed response variable in terms of a linear combination of the explanatory variables plus an error term (**Figure 1.1**). Suppose y_i is a response variable measured at one voxel, where $i = 1, \cdots, n$ indexes the observation. Suppose also that for each observation we have a set of J ($J < n$) explanatory variables denoted by x_{ij}, where $j = 1, \cdots, J$ indexes the explanatory variables. The explanatory variables may be covariates, functions of covariates, or variables indicating the levels of an experimental factor (e.g., normal and patient). The GLM at a specific voxel can be expressed as:

$$y_i = x_{i1}\beta_1 + \cdots + x_{ij}\beta_j + x_{iJ}\beta_J + \epsilon_i \tag{1.1}$$

where β_j are unknown parameters, corresponding to each of the J explanatory variables x_{ij}. Typically, the errors ϵ_i are modeled as independent and identically distributed normal random variables with zero mean and variance σ^2, $\epsilon_i \sim \mathcal{N}(0, \sigma^2)$**.** Notice that in the voxel-wise brain image mapping the error assumption means an equal error variance σ^2 across conditions or subjects but not across voxels in the brain (Friston, Holmes et al. 1994).

It can be expressed using matrix notation.

$$\boldsymbol{y} = \boldsymbol{X\beta} + \boldsymbol{\epsilon} \tag{1.2}$$

where $\boldsymbol{y}$ is the column vector of observations, $\boldsymbol{\epsilon}$ is the column vector of error terms, $\boldsymbol{\epsilon} \sim \mathcal{N}(\boldsymbol{0}, \sigma^2 \boldsymbol{I})$, and $\boldsymbol{\beta}$ is the column vector of parameters, X is a $n \times J$ matrix, which is the design matrix. The design matrix has one row per observation, and one column per explanatory parameter (i.e., x_{ij} is the *i*th observation for *j*th explanatory parameter). The mean value can be included by adding a column of ones to *X*.

Though the GLM is only expressed as a simple linear model it can also be used to express polynomial model if we include the polynomial term of the explanatory variables in the design matrix.

Estimation

Under the Gaussian assumptions of error terms (zero-mean, independent, and identically distributed), the likelihood of the observed data, given the model in equation (1.2) is (Press 2007),

$$P(\boldsymbol{y}, \boldsymbol{X} | \boldsymbol{\beta}) = \prod_{i=1}^{n} \frac{1}{\sqrt{2\pi\sigma^2}} e^{\frac{-(y_i - \boldsymbol{X_i}\beta)^2}{2\sigma^2}} \tag{1.3}$$

where $\boldsymbol{X_i}$ is the *i*th row of the design matrix $\boldsymbol{X}$. To maximize the likelihood, which equals minimize the residual sum-of-square, gives the ordinary least squares (OLS) estimates:

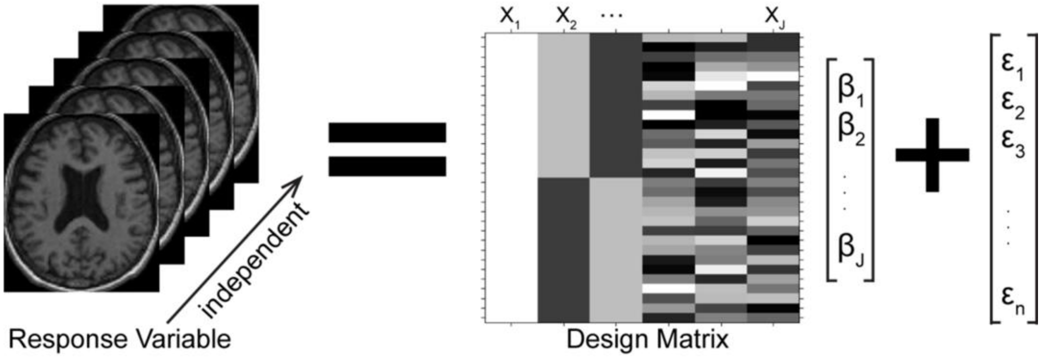

Figure 1.1 GLM in the human brain mapping. For each voxel inside the brain mask, the GLM is applied over subjects (or conditions) as the response variable, and the inference about the effect of the explanatory experiments are test. The first column in the design matrix is a column of ones corresponding to the mean value. The errors are independent identical normal distributed over subjects (or conditions).

$$\boldsymbol{\hat{\beta}} = (\boldsymbol{X}^\top \boldsymbol{X})^{-1} \boldsymbol{X}^\top \boldsymbol{y} \tag{1.4}$$

Inference

Based on the assumption that the error terms in the GLM follow a normal distribution and the explanatory variables are non-random (measured without error), the response variables are also normally distributed. Since the linear transformation of a normal distributed variable still has a normal distribution, it can be shown that the parameter estimates are distributed as normal distribution (Scheffe 1999). If $\boldsymbol{X}^\top \boldsymbol{X}$ is full rank (i.e., $rank(\boldsymbol{X}^\top \boldsymbol{X}) = J$), then for a $J \times 1$ column vector c containing J weights (e.g., $c = [1\ -1\ 0\ \dots\ 0]^\top$), we have:

$$c^\top \hat{\beta} \sim \mathcal{N}(c^\top \beta, \sigma^2 c^\top (X^\top X)^{-1} c) \tag{1.5}$$

The variance of the errors σ^2 can be estimated from the residuals, denoted as $\hat{\sigma}^2$. Furthermore, $\hat{\sigma}^2$ follows a chi-square distribution with n-J degrees of freedom and the estimators $\hat{\beta}$ and $\hat{\sigma}^2$ are independent. Substituting the estimated variance for the true variance we can assess the linear compounds of the model parameters $c^\top \beta$ using a t-distribution (Fisher's law (Fisher 1925)):

$$\frac{c^\top \hat{\beta} - c^\top \beta}{\sqrt{\hat{\sigma}^2 c^\top (X^\top X)^{-1} c}} \sim t_{n-J} \tag{1.6}$$

where t_{n-J} is a Student's t-distribution with n-J degrees of freedom. The null hypothesis $\mathcal{H}_0 \colon c^\top \beta = 0$ can be assessed by computing

$$T = \frac{c^\top \hat{\beta}}{\sqrt{\hat{\sigma}^2 c^\top (X^\top X)^{-1} c}} \tag{1.7}$$

and calculating a p-value by comparing T with a t-distribution having n-J degrees of freedom (Friston, Ashburner et al. 2007).

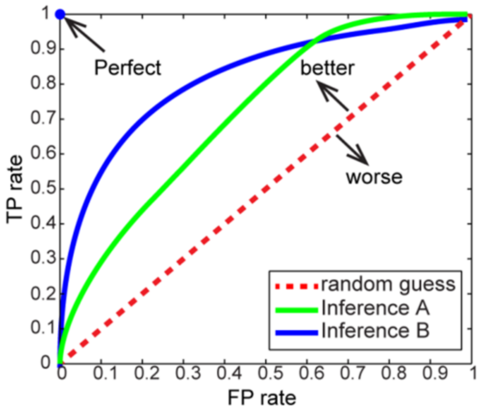

Figure 1.2 ROC curve. The points above the diagonal line are better than random guessing while the points below the line are worse. It is obvious that inference B has higher AUC than inference A that it performs generally better except at high FP rate where A has a slight advantage.

To test against the null hypothesis, we can use the distribution (t-distribution here) to estimate how likely it is that our statistic could have occurred by chance. Then we decide a p-value threshold as a significant threshold. When we find our statistic has a lower chance than the threshold value, we reject the null hypothesis, and accept the alternative hypothesis that there is an effect. We should aware here that we will never have evidence to accept the null hypothesis.

In rejecting the null hypothesis, we must accept a chance that the result has in fact arisen when there is in fact no effect, which is the type I error. Type I error is where a true null hypothesis was incorrectly rejected, the rate is denoted by α. In contrast, type II error is where one fails to reject a false null hypothesis. The rate of the type II error is denoted by β and related to the power of a test (which equals $1-\beta$). The relationship between them is described in **Table 1.1**.

Changing the p-value threshold, one can plot the true positive rate versus the false positive rate, which creates a receiver operating characteristic (ROC) curve (**Figure 1.2**). The ROC curve can be used to access the performance of an inference method (Zweig and Campbell 1993). A perfect prediction

Table 1.1 Relations between the null hypothesis and the inference

	Null hypothesis ($\mathcal{H}_0$) is true	**Null hypothesis ($\mathcal{H}_0$) is false**
Reject null hypothesis	Type I error (α) False positive (FP)	Correct True positive (TP)
Fail to reject null hypothesis	Correct True negative (TN)	Type II error (β) False Negative (FN)

method will yield a point at (0, 1), which represents no false positive and 100% true positive. A random guess inference will produce a diagonal line. Any reasonable estimation methods would result in the curve better than random guess but cannot reach the perfect point.

Commonly, when using ROC to compare inference methods, the area under curve (AUC) is calculated (Delong, Delong et al. 1988; Bradley 1997). The AUC is a portion of the area of the unit square such that its value will always be between 0 and 1. Besides, any reasonable inferences should have an AUC greater than random guessing (i.e., 0.5). Because the points in the AUC represent worse performance than the points along the ROC curve, the inference method has greater AUC gives better average performance. In **Figure 1.2**, it is also shown that an inference with high AUC may perform worse than an inference with low AUC in some regions in the ROC space but overall performs better.

Multiple Comparison

Since each brain voxel has a statistic of the effects of interest and the brain volume is large, the multiple comparison problem arises in voxel-wise brain imaging analysis (Friston, Frith et al. 1991). When deciding if this volume shows any evidence of the effect we need to account the fact that we performed thousands of statistical tests. Without knowing where the effect will occur, the null hypothesis is about the whole volume of statistics in the brain. The risk of error that we are prepared to accept is the family-wise error rate (FWER). To test a family-wise null hypothesis we can find a single test threshold, denoted by z, that the null hypothesis is rejected if any statistic values above the threshold, which is unlikely happen by chance.

In an extreme case that all voxels are independent, Bonferroni correction can be used to decide the single test threshold. In this case, each statistic value has a probability $p(T>z)$ of being greater than threshold z. If there are N tests, the probability that at least one test being greater than z, denoted as $P_{Bonferroni}$, is:

$$P_{Bonferroni} \leq 1 - \left(1 - p(T > z)\right)^N \approx Np(T > z) \qquad (1.8)$$

Thus, for an expected $P_{Bonferroni}$, the single test threshold z can be decided from equation (1.8).

Random Field Theory

The Bonferroni correction always controls the FP but is too conservative in many cases because most brain imaging data have spatial correlations so that not every test is independent. Random field theory (RFT) is a less conservative multiple correction method that is different from Bonferroni correction by accounting spatial correlations, which is suitable in smoothed statistical maps (Worsley, Marrett et al. 1996). Given that the statistic value from one voxel is correlated with nearby voxels there are fewer independent observations than there are voxels. RFT uses resels to approximately represent the independent spatial components in the human brain (Worsley, Evans et al. 1992). The number of resels depends only on the smoothness, encoded by the effective full width at half maximum of a Gaussian kernel, and the number of voxels. Then it considers Euler characteristic (EC) as the number of blobs in a statistic map above the threshold z. At high thresholds, EC is either one or zero. So the FWER here (P_{RFT}) is the expectation of EC:

$$P_{RFT} \approx E[EC] = \sum_{d=0}^{D} Resels_d EC_d(z)$$

where $Resels_d$ is the number of d-dimensional resels in the search region, $EC_d(z)$ is the fixed d-dimensional Euler characteristic density that is given by Worsley (Worsley 1994). For an expected *FWER*, the threshold, z, depends only on the number of resels in our image (in contrast to the number of voxels in the Bonferroni correction).

False Discovery Rate

The false discovery rate (FDR) is the expected rate of false positives among those voxels declared positive (the discoveries). Benjamini and Hochberg introduced a FDR method and proved it to control FDR conservatively (Benjamini and Hochberg 1995). The method starts by calculating the uncorrected p-value for each voxel and order them that the ordered p-values are $P_1 \leq P_2 \leq \cdots \leq P_N$. Next, to control the FDR at α, it finds the largest value k such that

$$P_k \leq \frac{k}{N}\alpha \tag{1.9}$$

The statistical value corresponding to P_k is chosen as the threshold z that all tests greater than or equal to it can reject their null hypotheses. This procedure requires that at least one null hypothesis is true in the multiple tests and it is proved to be conservative if the correlations between voxels are positive, which is a reasonable assumption for most unsmoothed or smoothed imaging data (Yekutieli and Benjamini 1999; Benjamini and Yekutieli 2001).

GLM in Structure Function Relationships Estimation

Exploring structure function relationships requires explaining one modality of neuroimaging data using information from other functional or structural imaging modalities. Recently, biological parametric mapping (BPM) has extended the widely popular SPM approach to enable application of the general linear model to multiple image modalities (both for regressors and regressands) along with scalar valued observations (Casanova, Srikanth et al. 2007). In functional and structural neuroimaging, the *de facto* standard “design matrix”-based general linear regression model and its multi-level cousins have enabled investigation of the biological basis of the human brain.

BPM uses biological information obtained from one or more imaging modalities, as regressors in an analysis of another imaging modality in a massively-univariate model. The statistical concepts are the same as when only response variables are from neuroimage data but using different design matrix in each voxel (**Figure 1.3**). The difference in design matrices is due to allowing image data covariates. The dimensionality of different modality images in a GLM should be the same and the corresponding voxels should represent the same location in the human brain.

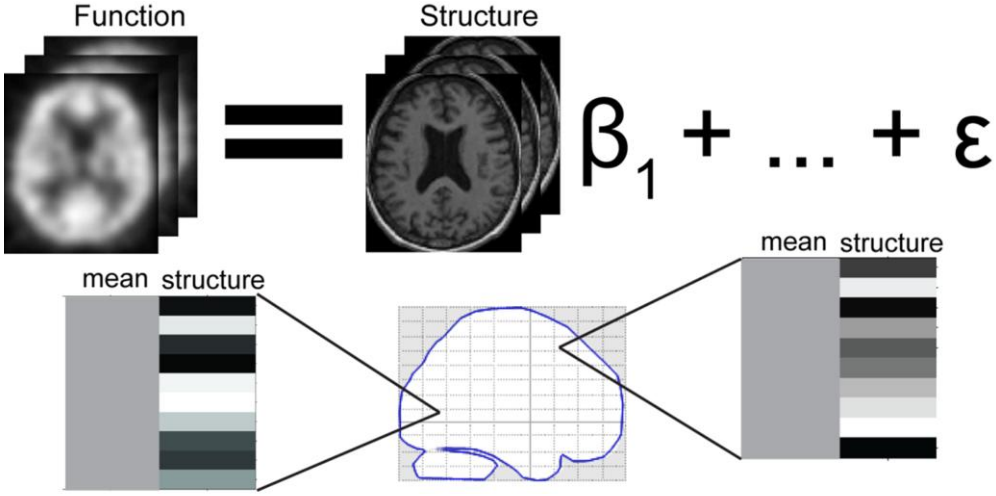

Figure 1.3 Structure function relationship estimation. The response variable comes from structure or function images, and at least one explanatory variable comes from other modality images. The value of the design matrix is different from voxel to voxel.

GLM in Resting-state fMRI Functional Connectivity

fMRI and SPM are widely used to infer spatial-temporal characteristics of brain activity (Friston, Jezzard et al. 1994; Friston, Holmes et al. 1995; Worsley and Friston 1995). In addition to task or event based models, many fMRI studies are now focused on the analysis of resting state activity (van den Heuvel and Hulshoff Pol 2010).

Since functional communication between brain regions plays a key role in understanding brain network and structure-function relationships, the analysis of functional connectivity in the human brain is valued with high importance. The functional connectivity analysis focuses on mapping functional brain network, examines the relationship among changes in one brain region to changes in others when the brain is at rest (**Figure 1.4**). In the resting-state fMRI experiments, volunteers are instructed to relax and not to think of something in particular, and their fMRI images are acquired. The first study of functional connectivity using resting-state fMRI is introduced by Biswal (Biswal, Yetkin et al. 1995; Biswal, Van Kylen et al. 1997), demonstrating functional communication during the left and right hemispheric regions of the primary motor network. The regions of the brain network are not silent during rest, but show lots of spontaneous activity that their fMRI time course are highly correlated (Cordes, Haughton et al. 2000; Lowe, Dzemidzic et al. 2000; Greicius, Krasnow et al. 2003).

ReML

In fMRI analysis, the GLM becomes

$$\boldsymbol{y} = \boldsymbol{X\beta} + \boldsymbol{e}, \qquad \boldsymbol{e} \sim \mathcal{N}\left(\boldsymbol{0}, \sigma_e^2 \boldsymbol{V}\right) \tag{1.10}$$

The error component takes the temporal correlation within one voxel into account and is non-spherical, because the fMRI time series contain correlated neuronal sources that cannot be modeled or filtered. Assuming that

$$\boldsymbol{V} = \sum \lambda_i \boldsymbol{Q_i} \tag{1.11}$$

The priors $\boldsymbol{Q_i}$ can be chose based on any temporal autocorrelation models. A widely used model is the first order autoregressive model (AR(1)) (Friston, Glaser et al. 2002), which the correlated error having the time domain form:

$$e_t = a e_{t-1} + w_t, \qquad w_t \sim \mathcal{N}(0, \sigma_w^2), |a| < 1 \tag{1.12}$$

where w_t is white noise.The covariance matrix $\boldsymbol{V}$ can be estimated by maximizing the negative free energy using restrictive maximum likelihood (ReML) method (Friston, Penny et al. 2002). Then it can be used to pre-multiply the model by a whitening matrix $\boldsymbol{W} = \boldsymbol{V}^{-1/2}$ giving:

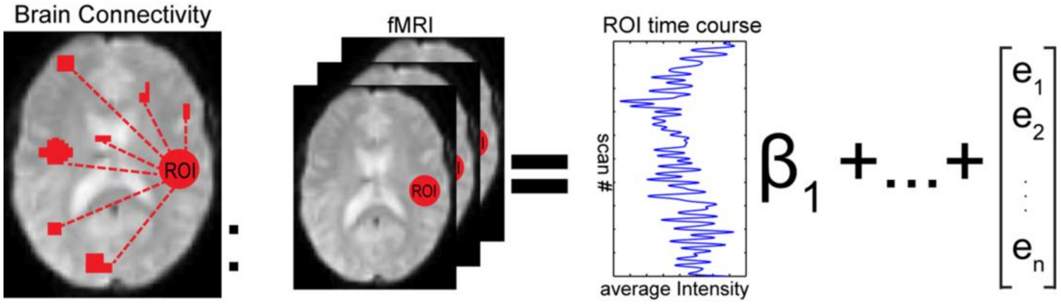

Figure 1.4 Function connectivity estimation. The explanatory variables that we are interested in are the average time course signals from a region of interest (ROI). The ROI time course with other confounds are used to explore the connectivity between the ROI and every other voxels in the human brain.

$$\boldsymbol{W}\boldsymbol{y} = \boldsymbol{W}\boldsymbol{X}\boldsymbol{\beta} + \boldsymbol{\epsilon}, \qquad \boldsymbol{\epsilon} \sim \mathcal{N}(\boldsymbol{0}, \sigma^2\boldsymbol{I}) \tag{1.13}$$

This new model now conforms to sphericity assumptions and can be interpreted in the usual way at each voxel.

Assumptions in Ordinary Least Squares

OLS is the most widely used method in linear regression analysis, which provides a simple consistent close form solution of the estimator. To appropriately use the OLS method in the human brain mapping the assumptions there should be checked beforehand: (1) the errors are independent and identically distributed normal random variables with zero mean; (2) the explanatory variables are measured without error or can be considered as without error comparing to the response variable; (3) the voxels in the brain images are one-to-one correspondence from subject to subject.

Error Assumptions

When there are outliers (e.g., unusual observation), the assumption of normal errors in OLS is violated. Robust regressions are proposed to deal with this situation that the error components are not normally distributed. A lot of robust regression methods have been proposed such as M-estimates (Huber and Ronchetti 1981), Least Median of Squares (LMS) estimates (Rousseeuw 1984), S-estimates (Rousseeuw and Yohai 1984) and MM-estimates (Yohai 1987). Each robust regression method has their advantages and disadvantages. Here we only focus on a popular method: M-estimators. M-estimators assume that the probability density function of the errors is $e^{-\rho}$ (Press 2007). Then Eq (1.3) becomes:

$$P(\boldsymbol{y}, \boldsymbol{X} | \boldsymbol{\beta}) = \prod_{i=1}^{n} e^{-\rho\left(\frac{y_i - \boldsymbol{X}_i \beta}{\sigma}\right)} \Delta y \tag{1.14}$$

where σ is weight factor, usually denotes standard deviation, Δy is small fixed factor on each data point. This model can be considered as a general case of OLS. In OLS, $\rho(r) = \frac{1}{2}r^2$. When outlier comes, r increases causes that $\rho(r)$ increases rapidly, which influence the estimation of the parameters $\boldsymbol{\beta}$ a lot. This is why least squares estimates method is sensitive to outliers. In robust regression, $\rho(r)$ does not increase or increase slowly when r exceeds a threshold, which assigns a small weight to outliers.

In contrast to statistical parametric mapping, non-parametric mapping methods make no assumptions about the probability distributions of the voxel values being assessed, which may be applied in situations where less is known about the distribution or the assumption is violated.

Under the null hypothesis, the explanatory variables have no effect on the response variable such that any orders of the explanatory data will result in the same response. If we assign each explanatory variable a label, the labels on the data will have exchangeability within the constraints of the randomized or weak distributional assumptions. The actual labeling used in the experiment (observed statistic) is randomly chosen from all possible labellings (permutations), so the probability of an outcome is the proportion of statistic values in the permutation distribution greater or equal to that observed. For example, if the observed statistic is the largest of the permutation distribution, the p-value is 1/N, where N is the number of permutations.

For multiple comparisons, the mechanics is computing the maximal statistic of the whole volume for each possible labeling to create a maximum statistic vector with the length of the number of permutations. Then the corresponding corrected p-value for each voxel is the proportion of the value in the maximum statistic vector that is greater than or equal to the voxel statistic.

Regressor Assumptions

When the regressors (explanatory variables) in the GLM are measured with error that cannot be ignored (e.g., allowing image data in the design matrix), the OLS estimator loses power and the estimated parameters are not accurate. Instead of minimizing the sum of squares along the response variable in OLS, Model II regression minimizes a weighted distance along the response and the random explanatory variables. The principle of Model II regression is first proposed by Deming (Deming 1943) and has been widely studied in the 2D case. Regression calibration deals with the measurement error problem by acquiring replicated measurements of the regressors. From these replicated measurements it provides a good estimation of the expectation value of the explanatory variables. Then, the estimated explanatory value are used in the design matrix instead of measured variables (Carroll, Ruppert et al. 2010).

The problem within the measurement error of the regressors is a bias estimation in OLS so that can also be solved by SIMulation and EXtrapolation (SIMEX) method. SIMEX is a general measurement error induced-bias correction method, which is not only suitable for the regression problem. The main idea of SIMEX is adding additional measurement errors, estimating a trend of bias versus the variance of the added errors, and then extrapolating this trend back to predict the results when there are no measurement errors (Carroll, Kuchenhoff et al. 1996).

Voxel-wise Assumptions

The GLM and statistical parametric mapping approach in accessing the neuroimaging inference assumes a voxel-wise model that requires voxels in each image are all one-to-one correspondence. Usually, this requirement is met or approximately met through some preprocessing steps. For group analysis, all subjects are normalized to a template (e.g., MNI-space) and spatially smoothed. For single subject functional connectivity analysis, all scans are realigned to the first scan or the mean scan through motion correction.

However, these preprocessing stories still cannot guarantee that the voxels are one-to-one correspondence unless we have perfect registration algorithms. In the case that a small portion of subjects are mis-registered, we can treat them as outliers and use robust regression. In the case that we need to consider spatial correlations in the estimation we can apply a spatial-spectral model (Kang, Ombao et al. 2012).

Our Contributions

The main contributions in the dissertation work are:

1. **Reliable Statistical Inference in Multi-modality Brain Image Analysis**. We addressed the outlier problems in multi-modality image analysis. Robust statistics have been developed and accepted in statistics field, but have not been applied in the context of neuroimage study. We incorporated robust regression into parametric mapping framework to implement a matlab toolbox with robust estimation and inference methods. We also implemented the non-parametric permutation tests through the use of cluster computer, to accomplish large permutation computations on a large volume of voxels. The OLS, M-estimates and the non-parametric methods are compared in simulation and empirical use. The advantages of the robust regression are demonstrated as a reliable method that tolerates outliers.
2. **Addressing Random Regressors in Multi-Modality Brain Image Analysis**. We took random regressors into account in images on images regression. The statistical theory in solving the problem is not new; identifying an appropriate model in real word is the science work we contributed here. We derived a Model II model solution from previous two variable approach to a general linear model so that the Model II regression can be implemented in the context of neuroimaging. We demonstrated that Model II regression and regression calibration approaches are compatible with the design matrix hypothesis testing and multiple comparison correction frameworks. Besides, we evaluate application of these methods comparing with OLS in simulation and an empirical illustration in the context of multi-modality image regression, demonstrating that the random regressors worth consideration in images on images regression.
3. **Robust Statistics and Empirical Validation in Functional Connectivity Analysis**. We proposed a novel approach for quantitatively evaluating statistical inference methods. This approach can evaluate the performance on empirical data where the truth is unknown and it does not require acquisition of additional data. In simulation, we proved that this approach is consistent with type I error and type II error. In empirical applications, this approach showed that robust regression was not needed in clear empirical 3T rs-fMRI data. However, it acts

better than the ordinary least squares estimation on some 7T rs-fMRI data. This approach can evaluate statistical methods on new problematic empirical dataset without knowing the specific characteristics of the artifacts (e.g., 7T fMRI) and lead to more reliable statistical model development.

4. **Spatial Temporal Models for Resting State fMRI Analysis**. We proposed models that can account the spatial correlations as well as the temporal correlations in the resting state functional connectivity analysis within the general linear model framework. The ROI-based spatio-spectral model for whole brain functional connectivity analysis was extended from a spatio-spectral model for task fMRI analysis. The voxel-wise spatio-temporal models were alternative considerations accounting the spatial correlations within a sliding window. The type I errors were demonstrated to be better controlled using these spatial temporal models than the one ignoring the spatial correlations. With unsmoothed empirical data studies, none of the models resulted in expected significance, but our proposed models provided more accurate estimations and statistical test maps.
5. **Multi-Site Brain Image Study**. We studied intra-modality and inter-modality brain image changes in an empirical multi-site large scale data project using mega-analysis and meta-analysis. We showed that the pre-processed data quality can be assessed through principle component analysis. After excluding outliers, we can acquire reasonable results from mega- or meta-analysis. The correlations and difference of the mega- and meta-analysis were explored. Our robust BPM proved to work well in estimating the relationships between gray matter density maps and the functional connectivity maps.

Previous Publication

Most contributions of this dissertation have been published. Robust and non-parametric regressions are discussed in accessing the human brain structure function relationships (Yang, Beason-Held et al. 2011; Yang, Beason-Held et al. 2011). The applications of the methods are shown (Holmes, Yang et al. 2013). The considerations of the regressor measurement errors in multi-modality neuroimage mapping are published in (Yang, Lauzon et al. 2011; Yang, Lauzon et al. 2012). Distribution issues in fMRI are evaluated from empirical datasets (Yang, Holmes et al. 2012). Quantitative evaluations comparing different inference methods when the truth is unknown are proposed in (Landman, Yang et al. 2012; Yang, Kang et al. 2012; Yang, Kang et al. 2013). The ROI-based spatio-spectral mixed effects model for resting state fMRI analysis are proposed in (Kang, Yang et al. 2013). The voxel-wise spatio-temporal models and the multi-site large scale data studies are under preparation.

CHAPTER II

BIOLOGICAL PARAMETRIC MAPPING WITH ROBUST AND NON-PARAMETRIC STATISTICS

Introduction

The assessment of structure-function relationships plays an important role in developing understanding of the human brain. These relationships appear to transcend scales, with connectivity dynamics appearing at both a micro- (intra-voxel) and macro- (the whole brain) scales (Honey, Thivierge et al. 2010). While there is firm evidence that structure shapes neural dynamics and function, the quantitative relationships and how such relationships might be altered in aging and disease remain an area of active research (Rubinov, Sporns et al. 2009). Statistical parametric mapping and its implementation in SPM software has emerged as a powerful tool to simultaneously study changes within single voxels and spatial patterns of activity or tissue volume changes (Worsley, Taylor et al. 2004; Friston, Ashburner et al. 2007). Recently, biological parametric mapping (BPM) (Casanova, Srikanth et al. 2007) and incorporation of voxel-wise covariates (Oakes, Fox et al. 2007) has enabled multi-modal images to be analyzed in a manner consistent with traditional voxel-based morphometry. BPM enables regression of multi-modal images in the same manner that SPM enables regression of images on scalars. In BPM, both the outcome variables (regressands, “y”) and the explanatory variables (e.g., regressors, “x”) may be images, so the design matrices vary voxel-by-voxel. With the BPM approach, one can directly assess the relationships between images containing functional and structural information. Alternatively, one could assess the explanatory power of one set of imaging modalities for another.

Violations of the distributional assumptions (such as the presence of outliers) can influence the results of a statistical analysis considerably, especially when the sample size is small (Friston, Ashburner et al. 2007). In neuroimaging, outliers can appear both because of imaging artifacts, data processing anomalies, and non-modeled anatomical differences between brains. In SPM, smoothing is used to compensate for “uninteresting” residual anatomical variability after registration. However, these anatomical differences are especially problematic in BPM because they introduce systematic and highly correlated variation in both regressors and regressands. Herein, we implement and evaluate robust and non-parametric statistical approaches for neuroimaging inference in the presence of outliers and distributional violations within the BPM regression model.

First, we consider the use of robust statistics for inference. These methods have been well-established in the statistical literature (Holland and Welsch 1977; Huber and Ronchetti 1981) and are commonly available in statistical analysis packages (Chen 2002). The general principle of robust statistics is to use an estimator that is consistent with a traditional, least-squares estimator, but is less sensitive to distributional assumptions – for example the median is a robust version of the mean. Herein, we extend the BPM approach to use robust inference with M-estimators (Huber 1964) in place of ordinary least squares regression. The resulting statistical parametric maps are compatible with the SPM software and are amenable to standard multiple comparison corrections approaches including random field theory family-wise error and false discovery rate approaches (Friston, Ashburner et al. 2007).

Second, we investigate non-parametric regression in the context of BPM. Non-parametric mapping requires minimal assumptions for validity and has been particularly advocated for small-sample size analysis in the statistical non-parametric mapping (SnPM) implementation (Nichols and Holmes 2002). We apply the SnPM non-parametric regression method within the BPM regression model to develop biological non-parametric mapping (BnPM). As with robust BPM, the uncorrected statistical maps are compatible with SPM software and are amenable to standard multiple comparison corrections approaches if appropriate field theory assumptions are valid. Additionally, the non-parametric approach offers the ability to perform non-parametric multiple comparison correction based on the maximal statistic.

This manuscript is organized as follows. First, we introduce the robust and non-parametric inference theory. Then we describe how these approaches can be used within a voxel-wise framework to develop robust BPM and BnPM. Simulation examples compare the results from original, robust BPM and

BnPM. We close with a discussion of the advantages and limitations of each method and the potential opportunities for continued innovation.

Methods

BPM enables the use of image on image regression by solving the general linear model (GLM) with different design matrices for each voxel. This contrasts with conventional SPM (statistical parametric mapping) which can only use non-image regressors as it uses the same design matrix for a whole image. By choosing “regression” in the BPM interface, we can evaluate one set of images relative to another set of images. BPM has been shown to be a promising technique (Casanova, Srikanth et al. 2007) for multi-parametric analysis.

To illustrate the potential short coming, consider two groups of data from one set of subjects where one subject is mis-registered relative to the remainder of the subjects; **Figure 2.1** shows one set of positron emissions tomography (PET) images and one set of smoothed gray matter (GM) images. If we examine one voxel within the misregistration region, simultaneous BPM analysis of both datasets suffers from greatly increased sensitivity to the outlier data as compared to separate SPM of the individual datasets. In BPM, both regressors and regressands are images which are not fixed, while in SPM, one regresses scalar values on images, which ensures the regressors are fixed. Both robust regression and nonparametric regression are promising methods for addressing this outlier problem. To reduce the effects of outliers, we proposed replacing the ordinary least squares regression method by robust regression, and using the robust variance to perform robust T-tests and F-tests.

Theory: Robust Regression

M-estimators represent a broad class of techniques which can be considered as the generalizations of the maximum likelihood framework (Fox 2002). Under the Gaussian distribution and independence assumptions, ordinary least squares regression is the maximum likelihood estimator. When there are

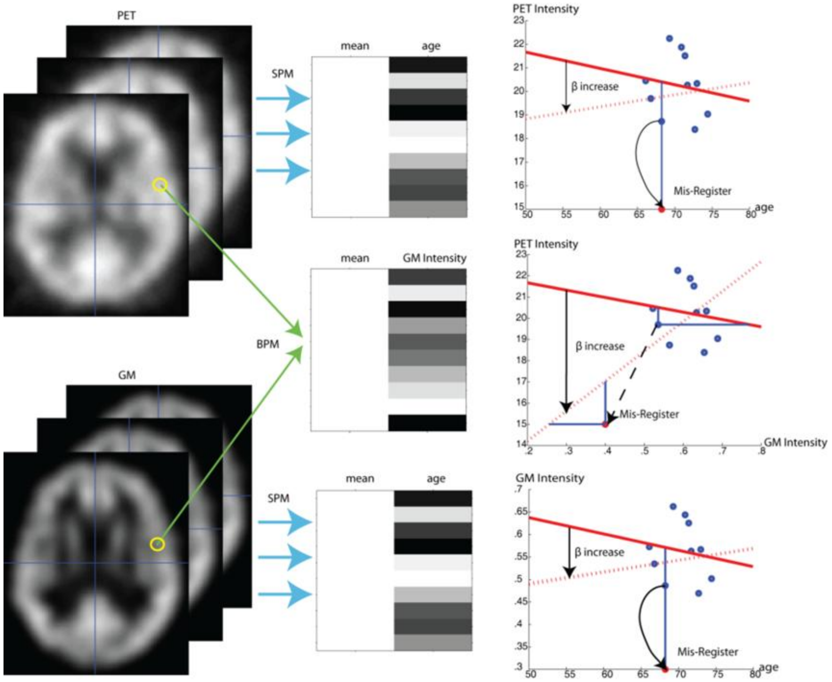

Figure 2.1 Increased sensitivity to outliers with BPM. Considered a simple one regressor situation, model $y = \beta x + \mu$ is used to fit data points in voxel wise analysis. In SPM, the imaging data (left column) lies along the y axis. (i.e., imaging data is treated as y in the fitted model.) The left column shows two sets of images data, PET blood flow maps (top row) and gray matter (GM) tissue density maps (lower row). The middle column shows the design matrix for each regression. Considered one voxel within mis-registration region, in separated analyses of these datasets with SPM (top and lower rows), a mis-registration induced outlier impacts only on data point in the y-direction. In a joint analysis with BPM, the outlier impacts both the x-axis and y-axis, and can result in dramatically different model fits. In the simulation the true β is a small negative value, but the outliers increase the estimated value of β to make it approximately zero or even a large positive number.

outliers, the measurement errors are not normally distributed. Since parameters are fitted to minimize the squared error, a single outlier observation can have very large impact. In the design of an M-estimator, one assumes a form for the conditional probability of the data that allows for large deviations (Press 2007).

$$\mathrm{P(data|model)} = \prod_{i=1}^{n} \{exp[-\rho(\frac{y_i - y(x_i|\beta)}{\sigma_i})]\Delta y\} \tag{2.1}$$

where y_i is the measurement, $y(x_i|\beta)$ is the predicted value based on the model, σ_i is the weighting factor for observation i, ρ is the influence function, and Δy is a small fixed factor for each data point.

The ρ function must be chosen appropriately to achieve the desired effect. If $\rho(r) = \frac{1}{2}r^2$, the M-estimator is equal to the least squares estimator. In this case, when an outlier occurs, $y(x_i|\beta)$ is pulled towards the outlier to minimize $\sum_{i=1}^{n} \rho(\frac{yi - y(x_i|\beta)}{\sigma_i})$, which makes the least squares estimate method sensitive to outliers. In robust regression, $\rho(r)$ does not increase or increases slowly when r is greater than a predefine constant, thus assigning a small weight to outliers which avoids pulling $y(x_i|\beta)$ towards the outlier. Hence, one seeks a ρ that has lower values in the extreme than a squared term. There are many weight functions that have been provided and evaluated. The Bisquare weight function and Huber weight function are both widely used and continuous weight functions. The Huber weight function is monotone, but assigns a bigger weight to possible outliers. Based on preliminary evaluations of sensitivity to outliers (not shown), we choose the Bisquare weight function (Beaton and Tukey 1974):

$$\rho(r) = \begin{cases} \left(\frac{C^2}{2}\right)\left[1 - \left[1 - \left(\frac{r}{C}\right)^2\right]^3\right] & |r| \le C \\ \frac{C^2}{2} & |r| > C \end{cases} \tag{2.2}$$

where C is the tuning constant, usually the value is chosen for 95% asymptotic efficiency when the distribution of observation error is Gaussian distribution.

Given the robust likelihood model in equation (2.1) and (2.2), we can use the maximum likelihood algorithm to estimate β. To maximize $P(\text{data}|\text{model})$, we can equivalently minimize $-\log P(\text{data}|\text{model})$:

$$\sum_{i=1}^{n} \rho(\frac{y_i - y(x_i|\beta)}{\sigma_i}) \tag{2.3}$$

Using maximum likelihood method, β should satisfy:

$$\sum_{i=1}^{n} \rho'(\frac{yi - y(x_i)}{\sigma_i})\left(-\frac{1}{\sigma_i}\right)\left(\frac{dy(x_i|\beta)}{d\beta}\right) = 0 \tag{2.4}$$

To solve this equation, we can use the iteratively reweighted least squares techniques (Holland and Welsch 1977), which can be applied to the general linear model (GLM). A specific algorithm to compute the estimated solution of β is provided in (Street, Carroll et al. 1988).

The least-squared formulas for statistical inference and confidence intervals are not meaningful when the parameters are computed using robust regression. Thus, a robust estimation of the covariance structure is required (Huber and Ronchetti 1981):

$$\operatorname{cov}(\hat{\beta}) = K^2 \frac{\left[\frac{1}{n-m}\right] \sum \psi(r_i)^2}{\left[\left(\frac{1}{n}\right) \sum \psi'(r_i)\right]^2} (X^T X)^{-1}, \;\; K = 1 + \frac{m}{n} \frac{var(\psi')}{(E\psi')^2}, \;\; \psi(r) \overset{\text{def}}{=} \frac{d\rho(r)}{dr} \tag{2.5}$$

and a robust project matrix can be used in place of $X^T X$:

$$\frac{\sum w_i x_{ij} x_{ik}}{\left(\frac{1}{n}\right) \sum w_i} \tag{2.6}$$

where n is the number of observation y, and m is the number of independent β parameters. The robust covariance formula is based on the assumption that $1 << m << n$. Details are discussed in (Huber 1973). In most cases for normal errors, the criteria of $\frac{m}{n} <$ ¼ can ensure agreement of Monte Carlo experiments with theoretical models. With limited degrees of freedom, a more conservative approach which restricts the robust variance estimation to be at worst similar to the variance of the least squares estimation may be appropriate (Dumouchel and O'Brien 1991). However, this can result in greatly reduced power in the presence of large outliers, and the assumption $m << n$ should be satisfied in the practical environment. The robust covariance structure and robust parameter estimates can be combined to perform robust T-tests and F-tests.

If there are no outliers, all distances are in the range of predefined threshold, the results from robust regression are the same as or close to least squares regression. When there are outliers, robust regression reduces the effect of outliers so that these methods suffer from reduced power (e.g., ability to detect true extreme values) compared with least squares regression which considers all data points equally. The assumptions used in SPM to estimate the spatial smoothing kernel are not as problematic with the outliers as information is pooled across the whole image. However, exploration of robust smoothness estimation would be a fantastic area of future research.

Theory: Non-parametric Regression

The least-squares approach is based upon the parameterization of the error distribution as independent and Gaussian. These assumptions are violated by outliers. In contrast, non-parametric methods make minimal assumptions about the error probability distributions and may be applied in situations where such assumptions would be inappropriate. Permutation tests have become a widely popular nonparametric test in neuroimaging through the SnPM software (Nichols and Holmes 2002). Permutation testing is relevant when data are associated with labels. The hypothesis is that if there is no effect in the data attributable to the labels, then the probability of the actual label order is equal to that of any other label permutation. Hence, the statistics associated with each of the possible labelings are also equally likely. The probability of an outcome as extreme or more than the one observed, the p-value, is the proportion of statistic values in the permutation distribution greater than or equal to that observed. The actual labeling used in the experiment is one of the possible labelings, so if the observed statistic is the largest of the permutation distribution, the p-value is 1/N, where N is the number of possible labelings of the initial randomization scheme (including the observed one). Herein, we use the same observed statistic that has been implemented in SnPM5 (Wellcome Department of Cognitive Neurology).

The large number of possible label permutations can be problematic, due to the computations involved. In situations where it is not feasible to compute the statistic images for all the labelings, a random subsample of labelings can be used. The set of N possible labelings is reduced to a more manageable N' consisting of the true labeling and $N' - 1$ randomly chosen from the set of N-1 possible relabeling. Such a test is sometimes known as an approximate permutation test, since the permutation distribution is approximated by a subsample, leading to approximate p-values and critical thresholds (Holmes 1994).

Random field theory family wise error (FWE) (Worsley, Marrett et al. 1996) and false discovery rate (FDR) (Benjamini and Hochberg 1995) corrections for multiple comparisons can be inappropriate for non-parametric methods since there are limited distributional assumptions. Holmes et al. (Holmes, Blair et al. 1996) provided a single threshold test for permutation multiple comparisons.

Variance estimation for t -statistic can be a noisy process, especially with limited sample sizes. Since one would expect the noise field to be relatively smooth, one can use a locally pooled variance to improve accuracy. For parametric methods, use of smoothing would be problematic because it would require knowledge of the variance-covariance of the voxel level variance structure. Permutation testing does not suffer from this limitation.

Implementation

The BPM software package was extended to include support for robust regression with Bisquare M-estimators and non-parametric techniques. In this manner, we extend BPM to form robust BPM (rBPM) and Biological non-Parametric Mapping (BnPM). BnPM uses non-parametric regression for each voxel, based on the permutation tests theory. Non-parametric regression calculates p-value based on randomized permutations (considering the proportion of the numbers with extreme value in permutations) but not based parametric assumptions. Thus, the direct result of non-parametric regression is a p-value rather than a T or F statistic. To report BnPM significance results within the SPM software, we invert the p-value to calculate a T map which can then be mapped back to a p-value in the visualization tools. The p-value is computed according to the sign of T test (i.e., proportion of the larger numbers for positive t-test and proportion of the smaller numbers for negative t-test), so the signs of T scores are preserved.

It is important to realize that the computational burden of non-parametric methods is very high. For a typical image size (e.g., 85*128*64), a modern, single-threaded CPU may require more than thirty days to compute 10000 permutations. To address this situation, we integrated BnPM with a cluster processing environment. With BnPM, a regression task (e.g., “job”) is divided into many smaller sub-jobs, each with a specific set of permutation orders for the whole job. Every sub job is considered a new job submitted to the cluster. The number of sub jobs and the execution wall time (i.e., maximum time allowed for each sub-job completion) is defined by the user and depends on the image size and the performance of the cluster. The description of each job is written in a format that provides compatibility to diverse cluster environments and scheduling priorities.

Experiments

First, to demonstrate BPM, rBPM and BnPM in a framework containing outliers, we created 20 simulated images as imaging regressors and another 20 images as the main modality (regressands). The imaging regressor images were created from one smoothed gray matter image by adding different noise fields which are generated from Gaussian distribution with zero mean. We define SNR as the mean signal divided by the standard deviation of noise. We define CNR as the magnitude of the range of voxel intensities divided by the standard deviation of noise. **Figure 2.2** illustrates representative simulated datasets. The main modality images are created from the regressor images. Inside the head of the caudate region, the simulated true-intensity of the main modality images is "1.5*regressor images – constant". Inside the putamen region, the simulated true-intensity of main modality images is "(-1)*regressor images + constant." Everywhere else the simulated true-intensity equals a constant. All constants are chosen to make SNR = 10 and CNR = 4. To simulate an artifact by mis-registration, one pair of images (e.g.,

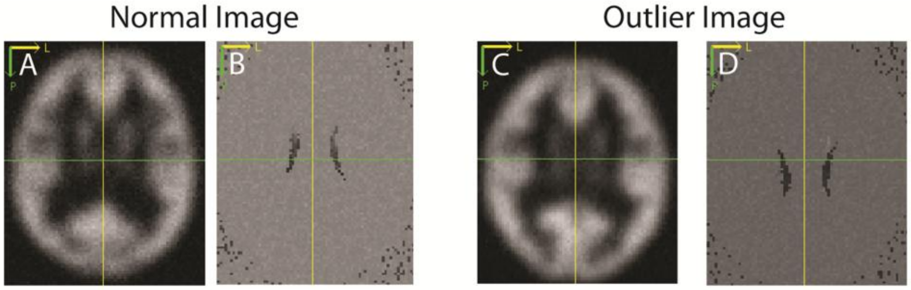

Figure 2.2 Simulation design. The normal image (A) shows the regressor images that are created from one image. The normal image (B) is one of the regressand images. The outlier images (C,D) are rotated around x (left-right axis) by 15 degrees.

representing one simulated subject) are rotated around the x axis (i.e., right-left) by 15 degrees. Then, a linear model ($y = \beta x + \mu$) was fit to evaluate correlations between the pairs of simulated images, and the null hypothesis of $\beta = 0$ was tested.

Second, to evaluate the relative performance of each method on empirical data, we tested the non-robust BPM, robust BPM and BnPM (with 10000 permutations) using a sub-set of the normal aging study of the BLSA neuroimaging project (Resnick, Goldszal et al. 2000). Herein, we used a sub-cohort of 23 healthy participants (14 M/9 F, 60-85 y/o at baseline). Each subject was studied annually for eight years with T1-weighted MRI sequence (1.5T, GE Medical Systems, SPGR, 0.9375x0.9375x1.5 mm, 256x256x124 mm field of view) and PET data (^{15}O, GE 4096+ scanner, 15 slices of 6.5mm thickness, 60s). The baseline scan was denoted as year 1 and the last scan was denoted as year 9. The data were preprocessed with SPM 5 (http://www.fil.ion.ucl.ac.uk/spm/software/spm5) following steps described in (Beason-Held, Kraut et al. 2008). The structural scans were normalized to MNI-space, segmented and smoothed (12 mm Gaussian kernel) to obtain smooth gray matter (GM) density images. PET images were normalized to SPM's spatial normalization, smoothed (12 mm Gaussian kernel) to MNI-space, and calibrated for global blood flow measurements to form quantitative cerebral blood flow measurements. The smoothed gray matter structure images were regressed on the PET data using non-robust BPM, robust BPM and BnPM to explore the potential for gray matter changes to explain changes in PET activation levels. Differences between estimated model fits and significance levels of the covariate were plotted.

Results

As **Figure 2.3** illustrates, rBPM and BnPM were incorporated into the BPM software. With the new user interface, the user has a choice about robust or non-robust regression. If the user chooses robust regression, we use the iteratively reweighted least squares method to perform M-estimation and compute robust variances for the GLM model. Otherwise the BPM analysis method remains the same as the original BPM package. If the user selects BnPM analysis, sub-jobs are created using non-parametric regression method and submitted to the supercomputing cluster. After all sub-jobs are finished, users can call BnPM results to calculate either uncorrected p-value or corrected p-value.

Table 2.1 summarizes the regression methods studied herein and presents a relative comparison of analysis time for the empirical example. All toolboxes that have been implemented are listed in the table with running time compared to the SPM running time. Note that non-parametric methods were set to use 10000 Monte Carlo permutations rather than exhaustive search. For multi-modality regression, BPM is the shortest while the BnPM running is the longest. Computation times are listed in terms of a single threaded CPU. For example, with a grid of 33 computers, the running time for BnPM would be equivalent to that of rBPM. The robust BPM running time is about 20 minutes for 20 subjects with 79*95*69 size images. The RobustWLS toolbox for SPM performs robust estimation to compensate artifacts in fMRI time series data using weighted least squares estimate; this method was not evaluated as this manuscript

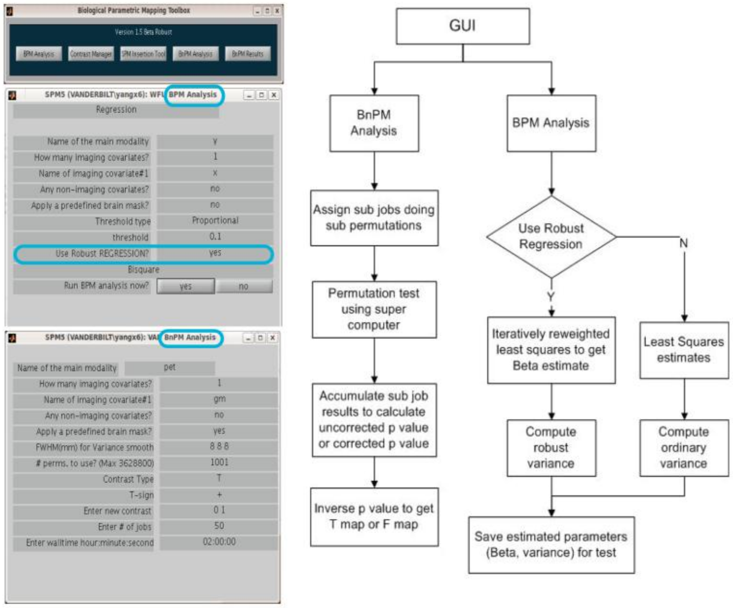

Name of the main modality	Y
How many imaging covariates?	1
Name of imaging covariate#1	X
Any non-imaging covariates?	no
Apply a predefined brain mask?	no
Threshold type	Proportional
threshold	0.1
Use Robust REGRESSION?	yes
Bisquare	
Run BPM analysis now?	

Name of the main modality	pet
How many imaging covariates?	1
Name of imaging covariate#1	gm
Any non-imaging covariates?	no
Apply a predefined brain mask?	yes
FWHM(mm) for Variance smooth	8 8 8
# perms. to use? (Max 3628800)	1001
Contrast Type	T
T-sign	+
Enter new contrast	0 1
Enter # of jobs	50
Enter walltime hour:minute:second	02:00:00

Figure 2.3 Software graphical user interface (GUI) and flowchart. With the new software, the user has a choice between robust regression, non-parametric regression, and traditional least squares regression (shown at left). Both options make slight modifications to the analysis workflow (right) with the end results of all methods prepared for visualization within the SPM software package.

Table 2.1 Comparison of statistical regression methods and available software for neuroimaging

		Regression Technique	
	Ordinary Least-Squares	**Non-parametric: Permutation Test**	**Robust: M-estimator**
Single Modality Software Package	**SPM (Friston, Ashburner et al. 2007)**	**SnPM (Nichols and Holmes 2002)**	**rSPM (Diedrichsen and Shadmehr 2005)**
Assumptions	Modality specific analysis, data are normally distributed.	Modality specific analysis, labels have exchangeability	fMRI time series data analysis
Relative computation time	Time 1.0*	Time 110	-
Inter- Modality Software Package	**BPM (Casanova, Srikanth et al. 2007)**	**BnPM†**	**rBPM†**
Assumptions	Multi-modality analysis, data are normally distributed	Multi-modality analysis, labels have exchangeability	Multi-modality analysis, most data are normally distributed but with some outliers
Relative computation time	Time 10	Time: 8×10^4‡	Time 90

* The total computational time for performing each regression analysis with data corresponding to the experiment shown in **Figure 2.4** (20 subjects, whole brain, 1 mm isotropic resolution, etc.) is reported relative to the computation time for the traditional SPM approach (approximately 15 seconds on our hardware).

† The highlighted methods represent contributions of this work.

‡ BnPM runs in approximately five hours “real time” on our cluster.

focuses on data with a single time point (Diedrichsen and Shadmehr 2005).

Table 2.2 shows the sensitivity and specificity of BPM, rBPM and BnPM on simulated dataset based on uncorrected p-value ($p<0.001$). The type I error is under control when there are no outliers (specificity ≈99.9%). When there are outliers, the specificity of BPM is excessively low (lower than 70%) and the sensitivity is also lower. The specificity of rBPM is slightly lower than the theoretical value. Note that the robust statistics are asymptotically valid, so ability to precisely control type I error improves with sample size. If rBPM is performed over larger sample size or higher tolerated type I error, the specificity can be better controlled. BnPM also results is slightly decreased specificity, but has lower sensitivity than rBPM.

After correcting for multiple comparisons, each of the three regression approaches would lead to a different conclusion based on inter-modality statistical parametric mapping as illustrated in **Figure 2.4**. With traditional BPM, one would see trends towards significant differences in both the region with true difference (i.e., caudate and putamen) and in the region where outliers were present after multiple comparisons. The rBPM approach would observe only the true difference. Finally, the BnPM found only

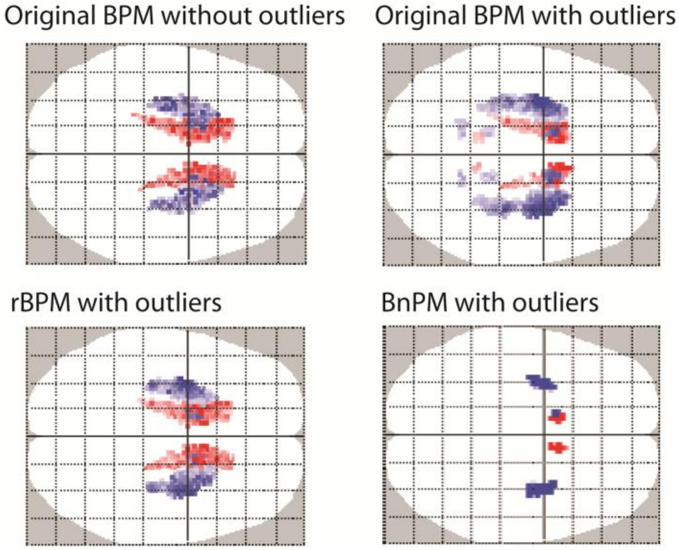

Figure 2.4 Simulation results. Results are displayed in SPM in glass brains. The statistical significance is calculated based on a selected p-value and then projected to three dimensions. Here we display one dimension of glass brains. The results are shown according to corrected p-value based on random field theory with $p<0.05$ and 5 voxels extent threshold to exclude noise. The red region is where there is a positive relationship and the blue region is where there is a negative relationship. Some points seem to overlap because the map collapses the out-of-plane dimension.

a small significant region inside the true difference region after correction for multiple comparisons with the maximum statistic.

To a large extent, the results found by BPM, rBPM, and BnPM were qualitatively similar using the empirical dataset as seen in **Figure 2.5**. However, there were several substantial (and significant) clusters where the methods reported dissimilar results, two of which are detailed in **Figure 2.5**.

Conclusions

The presence of outliers and distributional violations in neuroimaging is not a new phenomenon. Assessing the validity of statistical parametric models in a tractable manner has been paramount in the design of analysis software (Luo and Nichols 2003). Concerns over the validity of parametric models have motivated the development of alternative non-parametric approaches (Nichols and Holmes 2002). These approaches have become widely used for analysis of experiments with small sample sizes. While

Table 2.2 Sensitivity and Specificity on simulated dataset

	Caudate		**Putamen**	
	Sensitivity	**Specificity**	**Sensitivity**	**Specificity**
BPM on data without outliers	99.95% ±0.067%	99.89%±0.11%	97.21%±0.23%	99.87%±0.14%
BPM on data with outliers	66.38%±0.43%	67.41%±0.84%	81.53%±0.34%	58.03%±1.04%
rBPM on data with outliers	99.88%±0.12%	99.79%±0.12%	96.63%±0.41%	99.51%±0.20%
BnPM on data with outliers	72.08%±0.45%	98.77%±0.30%	89.50%±0.36%	98.54%±0.34%

The sensitivity is calculated in the voxels in the true mask and the specificity is calculated in the voxels outside the true mask but inside the rotated mask. They are computed based on uncorrected p-value ($p<0.001$). Here we show the mean value and standard deviation of sensitivity and specificity from 10 simulations (with different Gaussian noise) for each method.

manual data inspection and outlier exclusion are common place, systematic incorporation of these criteria in the estimation process (e.g., through M-estimators) has not been as thoroughly pursued in neuroimaging.

In this study, we incorporated robust regression (M-estimation) into BPM to replace ordinary least-squares regression and implemented BnPM by applying non-parametric permutation tests and using cluster computation. BPM, robust BPM and BnPM are all integrated in one SPM toolbox so that users can choose an appropriate regression method for the task at hand. Both simulation and empirical data suggest increased resilience to outliers in accordance to the theoretical motivationd for these methods.

In the simulation and empirical demonstrations, we demonstrate that these analysis approaches may lead to differing results. rBPM explicitly tolerates outliers by using robust regression, which makes the tool reliable against large outliers. However, rBPM still relies on Gaussian assumptions once outliers are excluded, so the results may not be appropriate for simulations with tenuous distributional assumptions. Meanwhile BnPM is intrinsically robust to distributional assumptions, but does not explicitly handle outliers, so it may suffer for lost power in these cases. Note that it would be straightforward to combine non-parametric and robust regression, i.e., perform permutation testing based on robust statistics, but this would dramatically increase the computation time.

In practical use, the assessment of structure-function relationships will likely involve the presence of outliers. As significant findings or surprising lack of findings are encountered, it is important to probe these datasets with robust tools to reveal the potential influence of outliers or distributional violations. For example, one would want to know if the outliers seen on **Figure 2.5** (near 0.8, 20 at left and 0.2, 38 on

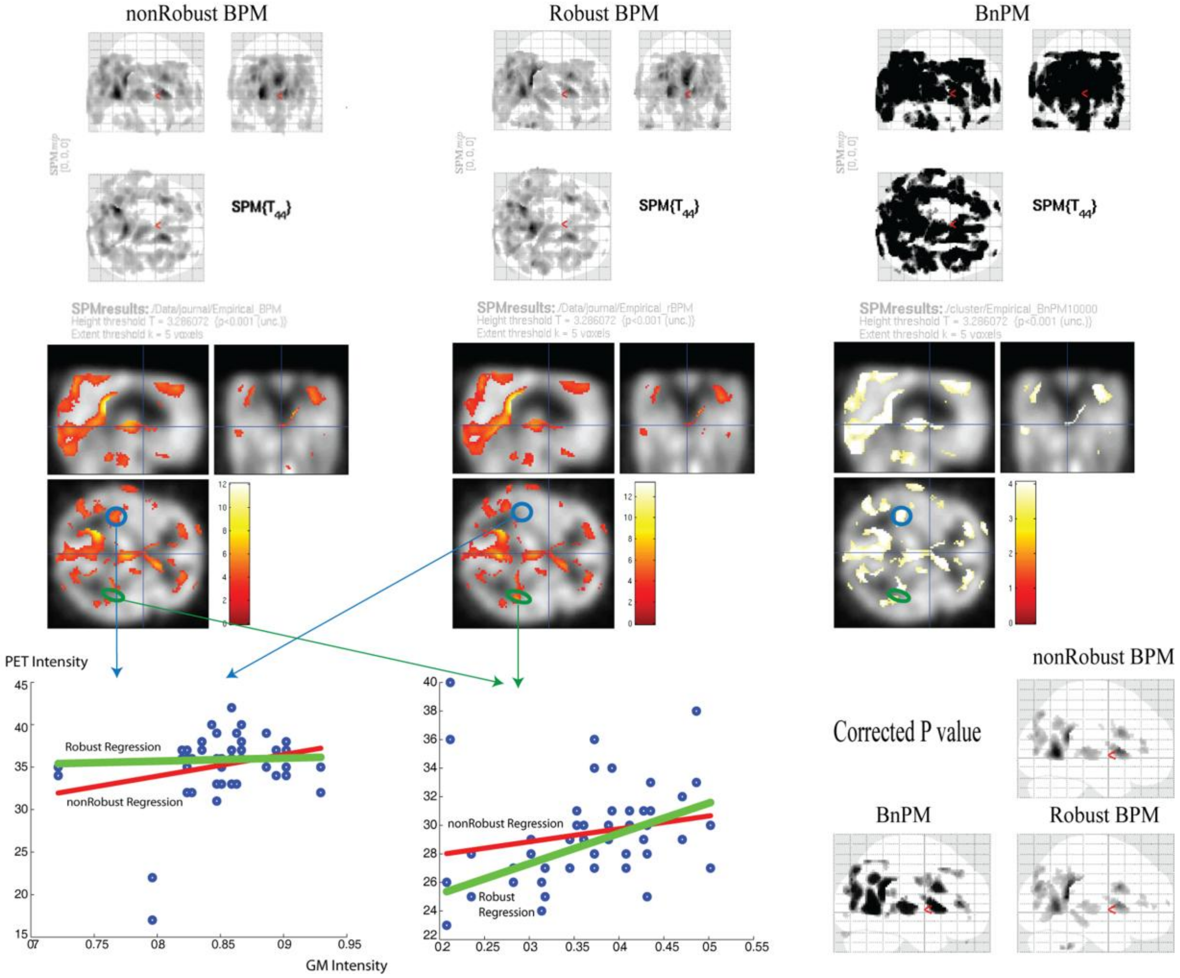

Figure 2.5 Empirical Results. Gray matter structural data of 23 participants from year 1 and year 9 (46 images) were regressed on the PET data of the same subjects. The statistical significance maps are under uncorrected p-value ($p<0.001$)and 5 voxels extent threshold to exclude noise. The two plots are the data for one voxel. The green arrow shows one voxel in the region where non-robust regression indicates non-significance while robust regression indicates significance. The blue arrow shows one voxel in the region where non-robust regression indicates significance while robust regression indicates non-significance. The x axis shows the value of GM structure data and the y axis shows the value of PET data. The red line is the fit of the non-robust regression while the green line is the fit of the robust regression. The maps in the lower right are the significance maps with family wise error correction of $p<0.05$ and 5 voxels cluster threshold.

right) are noise, systematic mis-registration, or seemingly valid data points. If these appear valid, is an important factor missing from the model design? As John Tukey, one of the founders of modern statistics commented, “that just which robust/resistant methods you use is not important-what is important is that you use some. It is perfectly proper to use both classical and robust/resistant methods routinely, and only worry when they differ enough to matter. But when they differ, you should think hard” (Huber 2002). Here we have provided two very different robust approaches for use in the neuroimaging community. The described software is available in open source under the Lesser GNU Public License via the NITRC project “rbpm” (URL: http://www.nitrc.org/projects/rbpm).

CHAPTER III

BIOLOGICAL PARAMETRIC MAPPING ACCOUNTING FOR RANDOM REGRESSORS WITH REGRESSION CALIBRATION AND MODEL II REGRESSION

Introduction

The strong relationship between structure and biological function holds true from the macroscopic scale of multi-cellular organisms to the nano-scale of biomacromolecules. Experience informs the clinical researcher that such structure-function relationships must also exist in the brain and, when discovered and quantified, will be powerful informers for early disease detection, prevention, and our overall understanding of the brain. Brain imaging modalities, such as positron emission tomography (PET) and magnetic resonance imaging (MRI), are primary methods for investigating brain structure and function. Quantification of the structure function relationship using imaging data, however, has been challenging owing to the high-dimensional nature of the data and issues of multiple comparisons.

Statistical Parametric Mapping (SPM) enables exploration of relational hypotheses using the design matrix paradigm (i.e., "$\boldsymbol{y} = \mathbf{X}\boldsymbol{\beta}$") without a priori assumptions of regions of interest (ROIs) where the correlations would occur (Friston, Frith et al. 1990; Friston, Frith et al. 1991). SPM was initially limited to single modality regression with imaging data represented only in the regressand (i.e., only $\boldsymbol{y}$ varied voxel by voxel) until extensions (e.g., Biological Parametric Mapping, BPM) were developed to enable multi-modality regression (i.e., to allow $\mathbf{X}$ to vary voxel by voxel) (Casanova, Srikanth et al. 2007; Oakes, Fox et al. 2007) and provide for inference robust to artifacts (Yang, Beason-Held et al. 2011). These multi-modal methods rely on the traditional ordinary least squares (OLS) approach in which regressors are exactly known (i.e., conditional inference). OLS inference is not inverse consistent; interchanging the regressor and regressand images would yield different estimates of relationships (as reviewed by (Altman 1991)). Although conditional inference may be reasonable in SPM, where scalar regressors are likely to have significantly less variance than the regressand imaging data such an assumption is clearly violated when both regressors and regressand are observations from imaging data (as in BPM).

Regression analysis accounting for errors in regressors would greatly improve the credibility of the BPM model by reasonably considering the randomness of the imaging modality in both the regressors and the regressands. Empirically successful statistical methods accounting for random regressors have been developed including regression calibration (Carroll, Ruppert et al. 2010) and model II regression (York 1966; Ludbrook 2010). The specific contributions of this work are that, (1) we implement these methods (which are established and accepted in statistical community) in the context of neuroimaging, (2) we demonstrate that these approaches are compatible with the design matrix paradigm, contrast-based hypothesis testing, and multiple comparison correction frameworks, and (3) we evaluate application of these methods in simulations and an empirical illustration in the context of multi-modality image regression. Herein, we focus on multi-modality inference; possible extensions to temporal modeling are discussed but left as future work.

Notation

For consistency, we have adopted the following notation. Scalar quantities are represented by italic, lower case symbols (e.g., σ^2). Vectors are represented by bold, italic, lower case symbols (e.g., $\boldsymbol{y}$). Matrices are bold, upper case symbols (e.g., $\mathbf{X}$). The symbol $\sim$ is used to note "distributed as," with $\mathcal{N}$ used to represent the multivariate Normal distribution. Subscripts are used to indicate context. For example, the subscript "obs" indicates the observed value of a random variable. Superscripts are used with matrices to index columns (i.e., $\mathbf{X}^{(i)}$ is the vector corresponding to the ith column of $\mathbf{X}$) and with vectors to indicate entries (i.e., $\boldsymbol{\beta}^{(i)}$ is the ith element of $\boldsymbol{\beta}$). Braces ("{ }") are used to indicate sets, while ":" is used to indicate vector concatenation and "$'$" indicates transpose. The hat ($\widehat{\ }$) indicates an estimated value of a random variable.

Theory

Our aim is to explain the observed intensity from one imaging modality, $\boldsymbol{y}$, with a set of regressors, $\mathbf{X}$, of which at least one member is observed intensity from another imaging modality. We begin with a typical general linear model (GLM) and reformulate it to explicitly reflect the clinical imaging case of both random and non-random regressors. To begin, GLM is formulated as,

$$\boldsymbol{y}_{obs} = \boldsymbol{y} + \boldsymbol{\eta}_y, \qquad \boldsymbol{\eta}_y \sim \mathcal{N}(\mathbf{0}, \sigma_y^2\, \mathbf{I}) \tag{3.1}$$

$$\boldsymbol{y} = \mathbf{X}\boldsymbol{\beta} + \boldsymbol{\varepsilon}, \qquad \boldsymbol{\varepsilon} \sim \mathcal{N}(\mathbf{0}, \sigma_\epsilon^2\, \mathbf{I}) \tag{3.2}$$

where $\boldsymbol{\eta}_y$ is a parameterization of observational error in $\boldsymbol{y}$, $\boldsymbol{\beta}$ is a vector of the fitted coefficients, $\boldsymbol{\varepsilon}$ is the regression error in the model fit, and $\mathbf{I}$ is the identity matrix. The observation error ($\boldsymbol{\eta}_y$) and the equation (or model error) ($\boldsymbol{\varepsilon}$) are assumed to be mutually independent.

Let us consider the columns of the design matrix, $\mathbf{X}$, in two disjoint sets: fixed regressors whose values are considered to be exactly known, $\mathbf{X}_f$, (i.e., the variance in observed values is much less than the variance of the regressand) and random regressors, $\mathbf{X}_r$, whose observations have non-negligible variance (i.e., $\mathbf{X} = [\mathbf{X}_r : \mathbf{X}_f]$). Note, $\boldsymbol{\beta}$ must be correspondingly partitioned into $\boldsymbol{\beta}_f$ and $\boldsymbol{\beta}_r$ (i.e., $\boldsymbol{\beta} = [\boldsymbol{\beta}_r : \boldsymbol{\beta}_f]$). In BPM, all regressors in the design matrix are treated as fixed regressors, but in fact, the image intensities in the design matrix are observed with measurement error. The use of traditional OLS yields a non-inverse consistent fit, as illustrated in **Figure 3.1,** due to the model that only considering measurement errors occur in $\boldsymbol{y}$, but ignoring the errors in $\boldsymbol{x}$. If the roles of $\boldsymbol{x}$ and $\boldsymbol{y}$ are exchanged, the estimated coefficients are altered (i.e., the errors are assumed to lie in $\boldsymbol{x}$ and the fit is not inverse consistent).

In the more realistic regressor measurement error model, the $\mathbf{X}_r$ are not exactly known and instead are estimated from observations, $\mathbf{X}_{r,obs}$, containing measurement error:

$$\mathbf{X}_{r,obs} = \mathbf{X}_r + \boldsymbol{\eta}_x, \qquad \boldsymbol{\eta}_x \sim \mathcal{N}(\mathbf{0}, \mathrm{diag}(\boldsymbol{\sigma}_{x,r}^2)) \tag{3.3}$$

where $\boldsymbol{\eta}_x$ is zero-mean Gaussian distributed measurement error with variances $\boldsymbol{\sigma}_{x,r}^2$. Note diag indicates a matrix with diagonal elements corresponding to the given vector. Herein, we will discuss two methods that, unlike ordinary least squares, can account for the regressor measurement error: regression calibration and model II regression.

Theory: Regression Calibration

Regression calibration is a simple, widely-applicable approach to measurement error analysis described in (Carroll, Ruppert et al. 2010). The random regressors, $\mathbf{X}_r$, are observed multiple times to obtain replicated measurements, $\mathbf{X}_{r,obs_1}, \mathbf{X}_{r,obs_2}, \ldots \mathbf{X}_{r,obs_d}$, for d repeated measurements. To create an estimate of $\mathbf{X}_r$, one could simply average the repeated measurements. However, regression calibration improves upon the average by accounting for the covariance between all regressors (including the fixed regressors). In short, the new estimated values for the random regressors, $\mathbf{M}_r$, are obtained through approximation of $\mathrm{E}(\mathbf{X}_r | \mathbf{X}_f, \{\mathbf{X}_{r,obs_i}\}_{i=1 \ldots d})$, where E indicates the expected value. Using the new

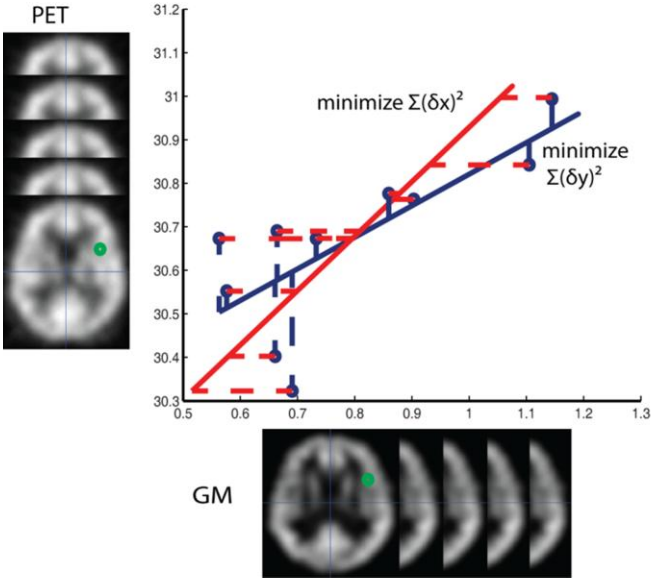

Figure 3.1 Optimal regression fitting depends on how distance is considered. In traditional OLS (blue: regress "x on y"), the sum of squared vertical distance is minimized (blue dash), while in the reciprocal problem with OLS (red: "y on x"), the sum of squared horizontal distance (red dash) is minimized. The resulting regression lines from the two approaches (solid blue and solid red respectively) disagree with each other. The estimation result depends on in which direction we minimize the distance such that a symmetric optimal model cannot be achieved.

approximation of $\mathbf{X}_{\boldsymbol{r}}$, a standard analysis on the estimated general linear model is performed,

$$\boldsymbol{y}_{\boldsymbol{obs}} = \mathbf{M}_r\boldsymbol{\beta}_r + \mathbf{X}_f\boldsymbol{\beta}_f + \boldsymbol{\varepsilon} + \boldsymbol{\eta}_y \tag{3.4}$$

For inference on the significance of $\boldsymbol{\beta}$ estimates, we used the residual bootstrap method as reviewed in (Carroll, Ruppert et al. 2010).

Theory: Model II Regression

In medical image analysis, especially in functional MRI, it is difficult or impossible to obtain replicated measurements for **X**. Additionally, replicated measurements are complicated by the increased resource requirements, increased cost of experimentation, and increased level of volunteer participation. To work within these constraints and avoid the need for replicated measurements, we consider model II regression. model II theory diverges from OLS through incorporation of the noise in random regressors (as in equation (3.3)), and equation (3.2) becomes,

$$\boldsymbol{y} = \mathbf{X}_r\,\boldsymbol{\beta}_r + \mathbf{X}_f\,\boldsymbol{\beta}_f + \boldsymbol{\eta}_y \tag{3.5}$$

Let $\boldsymbol{z}_i$ be a vector concatenating the observational errors in $\boldsymbol{y}^{(i)}$ and in $\mathbf{X}_{r,obs}^{(i)}$. Note that the observational errors, $\boldsymbol{z}_i$**,** are errors across subjects and not conditional errors across an image. Given that each $\mathbf{X}_{r,obs}^{(i)}$ vector is observed from a unique experimental technique, the elements of $\boldsymbol{z}_i$ are independent and that the row vectors $\boldsymbol{z}_i$ are also independent across subjects. Therefore, the errors across $\boldsymbol{z}_i$ follow a multivariate normal distribution (Friston, Holmes et al. 1994):

$$\boldsymbol{z}_{\boldsymbol{i}} = \left[\boldsymbol{y}_{obs}^{(i)} - \boldsymbol{y}^{(i)} \quad : \quad \mathbf{X}_{r,obs}^{(i)} - \mathbf{X}_r^{(i)}\right] \sim \mathcal{N}(\mathbf{0}, \Sigma). \tag{3.6}$$

Under these assumptions (normal, independent, and identically distributed), the log-likelihood of the observed data, given the model in equation (3.5) and equation (3.6) is,

$$\ln P\left(\boldsymbol{y}_{obs}, \mathbf{X}_{r,obs} | \boldsymbol{\beta}, \Sigma, \boldsymbol{y}, \mathbf{X}_r\right) = \sum_{i=1}^{n} \ln\left(2\pi^{-n/2}\left(\det(\Sigma)^{-1/2}\right)\right) - \frac{1}{2}\sum_{i=1}^{n}\left(\boldsymbol{z}_{\boldsymbol{i}}\Sigma^{-1}\boldsymbol{z}_{\boldsymbol{i}}'\right) \tag{3.7}$$

where there are n subjects (rows of **X**).

Maximizing the log likelihood, equation (3.7), is equivalent to minimizing $s = \sum_{i=1}^{n}(\boldsymbol{z}_i \Sigma^{-1} \boldsymbol{z}_i')$. With the assumption of independent observations, the covariance matrix, Σ, is diagonal with entries $[\sigma_y^2 : \boldsymbol{\sigma}_{x,r}^2]$. Hence, s can be re-expressed as,

$$s = \sigma_y^{-2} \|\boldsymbol{y}_{obs} - \boldsymbol{y}\|_{L2}^2 + \sum_{j=1}^{q} \left(\boldsymbol{\sigma}_{x,r}^{(j)}\right)^{-2} \left\|\mathbf{X}_{r,obs}^{(j)} - \mathbf{X}_r^{(j)}\right\|_{L2}^2 \tag{3.8}$$

where there are q regressor random variables and the subscript $L2$ indicates the L^2 norm (i.e., square root of the sum of squares). Equation (3.8) is minimized when its partial derivatives with respect to each dependent variable is zero. We first solve for each $\mathbf{X}_r^{(j)}$ by differentiating s with respect to $\mathbf{X}_r^{(j)}$, setting the result to zero, and using the linear model relation (equation (3.5)). Some manipulation yields,

$$s = \frac{\left\|\boldsymbol{y}_{obs} - \left(\mathbf{X}_{r,obs}\,\boldsymbol{\beta}_r + \mathbf{X}_f\,\boldsymbol{\beta}_f\right)\right\|_{L2}^2}{\sigma_y^2 + \boldsymbol{\sigma}_{x,r}^{2}{}'\,\boldsymbol{\beta}_r} \tag{3.9}$$

Equation (3.9) is now independent of the unknown $\mathbf{X}_r$ and provides an intuitive form as the error in the numerator is balanced by the individual variances in the denominator and mirrors the more readily available multivariate case with non-random $\mathbf{X}$ and the univariate case that accounts for one random regressor (Press 2007). equation (3.9) is a function of two unknown vectors: $\boldsymbol{\beta}$ and $\boldsymbol{\sigma}$.

Hence, the variance ratios need to be known in order to minimize s by solving $\boldsymbol{\beta}$; otherwise the system of equations will be undetermined for $\boldsymbol{\sigma}$ (Carroll and Ruppert 1996). Note that only the relative variance between observations factors into s (as opposed to the absolute variances). If the ratios for $\frac{\boldsymbol{\sigma}_{x,r}^2}{\sigma_y^2}$ are known (or can be reasonably estimated), then the optimization becomes well defined with an equal number of unknown to available equations. We employ numeric Nelder–Mead method to optimize with respect to $\boldsymbol{\beta}$. If we add the further assumption that the ratio of the overall measurement error ratio across subjects is proportional to the ratio of the image noise variance, then we can estimate the measurement error ratio by estimating the ratio of image noise for each modality. We note that the maximum likelihood estimate of $\boldsymbol{\beta}$ are asymptotically normally distributed. As reviewed in (Friston, Ashburner et al. 2007), we can use the Fisher information to construct the asymptotic distribution of contrasts of the parameter estimates (i.e., $\boldsymbol{c}'\widehat{\boldsymbol{\beta}}$) and estimate t-values (and corresponding p-values) for inference.

A common theoretical problem with applications of model II regression is that it is tends to overestimate the influence of the error of the regressors (i.e., $\boldsymbol{\eta}_x$ and $\boldsymbol{\eta}_y$) by ignoring the equation error ($\boldsymbol{\epsilon}$) (Carroll, Ruppert et al. 2010). Here, we partially address this problem by partitioning the total error in an arbitrary (but reasonably justified) manner according to the relative variances of each measurement (i.e., σ_y^2 versus $\boldsymbol{\sigma}_{x,r}^2$). Hemodynamics and/or correlated error models could be addressed in this framework through estimation and pre-whitening as is typically done with restricted maximum likelihood approaches for fMRI time series (Friston, Glaser et al. 2002; Friston, Penny et al. 2002), but secondary noise modeling is beyond the scope of this initial work.

Methods and Results

Regression calibration and model II regression were implemented in MATLAB as an SPM Toolbox and integrated with a cluster processing environment as illustrated in Figure 3.2. Regression calibration and model II regression are incorporated as regression method choices in the BPM toolbox for the SPM software using Matlab (Mathworks, Natick, MA). These modified software and demonstration data corresponding to the simulation examples are released in open source at http://www.nitrc.org/projects/rbpm/.

Single Voxel Simulations

Regression Calibration vs OLS

For each of the following single voxel simulation scenarios, a simulated voxel with 50 observations (i.e., subjects) was studied using a model with one random regressor, one fixed regressor, and a single constant: $\boldsymbol{y} = \boldsymbol{x}_r\beta_r + \boldsymbol{x}_f\beta_f + \beta_1 + \varepsilon$. In each of 500 Monte Carlo trials, regressors ($\boldsymbol{x}_r$ and

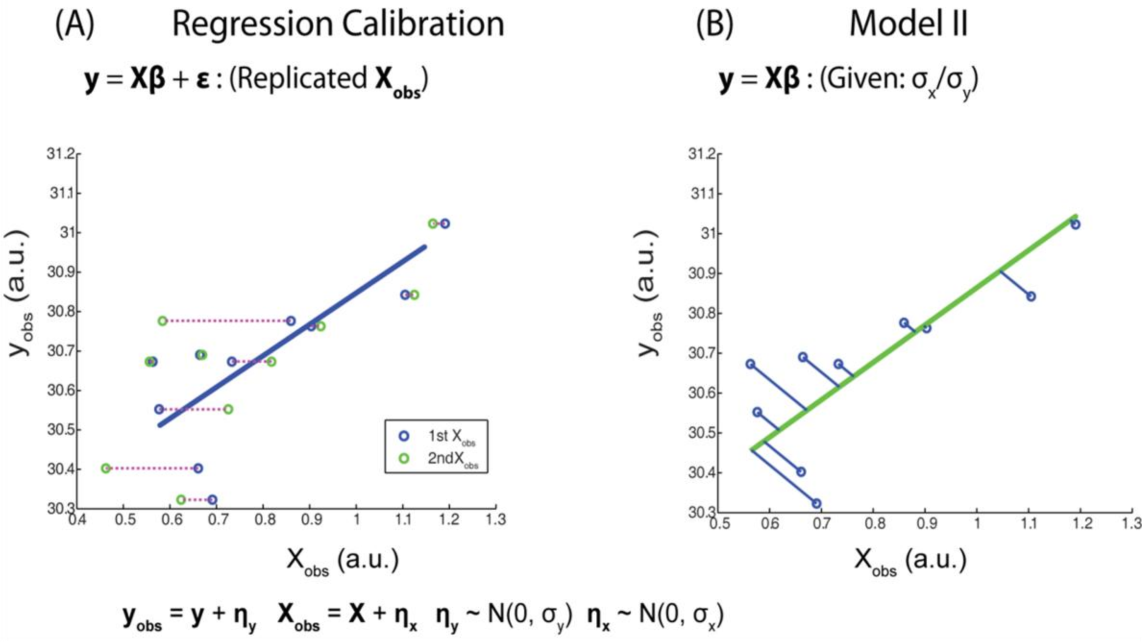

Figure 3.2 Regression calibration (A) and model II regression (B) address uncertainty in multiple variables. Regression calibration uses repeated measures to estimate variance in the regressors, while model II regression relies on an estimation of the relative variance between the regressors and regressands to minimize error.

$\boldsymbol{x}_f$) were chosen randomly from the uniform distribution [0 1], β_T were chosen randomly from the uniform distribution [0 2], and errors were added to $\boldsymbol{y}$ and $\boldsymbol{x}_r$ from a normal distribution with variances σ_y^2 and $\sigma_{x,r}^2$ respectively. Two measurements for each $\boldsymbol{x}_r$, $\left(\boldsymbol{x}_{r,obs_1}, \boldsymbol{x}_{r,obs_2}\right)$ were simulated. OLS was performed using only the first measurement $\boldsymbol{x}_{r,obs_1}$. Regression calibration was evaluated compared to OLS with the relative root mean squared error (rRMSE) in $\boldsymbol{\beta}$ (β_{rRMSE}), defined over each Monte Carlo Simulation for regression calibration (RC) and OLS estimates relative to the true (T) parameters:

$$\beta_{rRMSE} = \frac{\sqrt{\sum_{sn=1}^{500}\left(\widehat{\boldsymbol{\beta}}_{RC,sn} - \boldsymbol{\beta}_{T,sn}\right)^2}}{\sqrt{\sum_{sn=1}^{500}\left(\widehat{\boldsymbol{\beta}}_{OLS,sn} - \boldsymbol{\beta}_{T,sn}\right)^2}} \tag{3.10}$$

A. **Regression calibration vs OLS response to $\boldsymbol{\sigma_{x,r}}$: $\boldsymbol{\sigma_y}$ ratios (Figure 3.3A).** Simulations were performed varying $\boldsymbol{\sigma}_{x,r}$: σ_y. Regression calibration performs equally well as OLS with small $\boldsymbol{\sigma}_{x,r}$: σ_y, but becomes advantageous as more relative error is introduced into $\boldsymbol{x}_r$ observations. This advantage is most notable in random regressor coefficient βr.

B. **Regression calibration vs OLS response to number of random regressors (Figure 3.3B).** The above model was altered by including up to four additional random regressors with randomized coefficients. Over the model complexity range investigated, regression calibration has universally smaller errors in all estimated coefficients compared to OLS. Interestingly, the advantage of regression calibration over OLS for β_f and β_1 increased with increasing model complexity, while the advantage over OLS decreased for β_r.

Regression calibration sensitivity to the number of replicated measurements (Figure 3.3C). To assess the response of regression calibration to the number of replicated measurements, the number of random regressor measurements was increased from two to ten. For the increasing number of replicated measurements, the accuracy of regression calibration for β_r, β_f, and β_1, is improved slightly over OLS. We note that since the noise on the regressors was Gaussian in this simulation, regression calibration (which assumes a Gaussian error model) was able to accurately model the variance with limited numbers of observations.

Model II Regression vs OLS

Model II regression was compared to OLS using a similar model as was used for comparisons with regression calibration. A simple model with one fixed and one random regressor was used $\boldsymbol{y} = \boldsymbol{x}_r\beta_r + \boldsymbol{x}_f\beta_f + \beta_1$. For 50 observations, regressors ($\boldsymbol{x}_r$ and $\boldsymbol{x}_f$) were chosen randomly from the uniform distribution [0 1], $\boldsymbol{\beta}_T$ were chosen randomly from the uniform distribution [0 2] and errors were added to $\boldsymbol{y}$ and $\boldsymbol{x}_r$ from a normal distribution with variances σ_y^2 and $\sigma_{x,r}^2$, respectively. Model II regression and OLS are performed on the same dataset. Relative performance of model II to OLS is quantified by the rRMSE in β (equation (3.10)).

A. **Model II vs OLS response to $\boldsymbol{\sigma_{x,r}}$: $\boldsymbol{\sigma_y}$ ratios (Figure 3.4A).** Simulations were performed varying $\sigma_{x,r}$: σ_y. The performance of model II regression and OLS are comparable for small $\sigma_{x,r}$: σ_y, but model II regression becomes more advantageous as more relative error is introduced into $\boldsymbol{x}_{r,obs}$. The improvement is observed specifically on the random regressor coefficient β_r, whereas the constants not associated with random regressors, β_1 and β_f, remain with approximately equal accuracy in estimation between the two models.

B. **Model II vs OLS response to number of random regressors (Figure 3.4B).** The above model was altered by including up to four additional random regressors with randomized coefficients (randomly drawn from the uniform distribution [0 2]). Model II has smaller errors in the βr estimates than OLS; however, model II becomes less advantageous with increases in the number of random regressors. Note that the number of observations was not increased to compensate for the increased model complexity; therefore less data per regressor is available with more regressors.

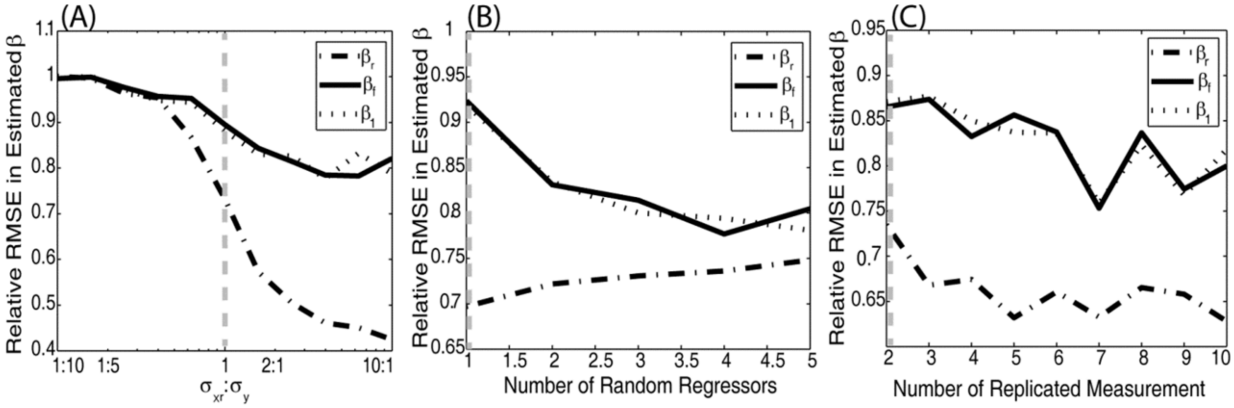

Figure 3.3 The rRMSE of regression calibration to OLS for each estimated coefficient ($\boldsymbol{\beta_r}$, $\boldsymbol{\beta_f}$, $\boldsymbol{\beta_1}$) are plotted as a function of the ratio of the true standard deviations, $\boldsymbol{\sigma_{x,r}}$: $\boldsymbol{\sigma_y}$ (A), the number of random regressors, $\mathbf{X}_{\boldsymbol{r}}^{(j)}$ (B), and the number of replicated measurements (C). (Note, y-axis was visually optimized for each figure and are not common across A, B, and C.) With increasing $\boldsymbol{\sigma_{x,r}}$: $\boldsymbol{\sigma_y}$ ratios, regression calibration has increased relative accuracy in $\boldsymbol{\beta}$r estimates compared to OLS. The common simulation shared in (A, B, C) is indicated by a gray line.

C. **Model II sensitivity to the estimated ratio (Figure 3.4C).** To assess the robustness of model II against varying levels of accuracy in the $\sigma_{x,r}$: σ_y ratio estimates, the estimated ratio of the variance was altered between 1/10th and 10 times its true value, which was set at one. Under the cases simulated here, model II is insensitive to the ratio mis-estimation range 0.5 to 2, and relatively insensitive over the range 0.1 to 3. At extremely incorrect ratio values, the β_r estimate rapidly loses accuracy. Based on this analysis we can apply model II regression using an estimated error ratio, with reasonable confidence in the methods' tolerance to mis-estimation of variance ratios.

Volumetric Imaging Simulation

To explore the performance of these methods on an imaging dataset, we simulated images of two modalities and regressed one modality on the other modality. The true regressor images are simulated from smoothed gray matter (GM) density images of 40 participants in the normal aging study of the

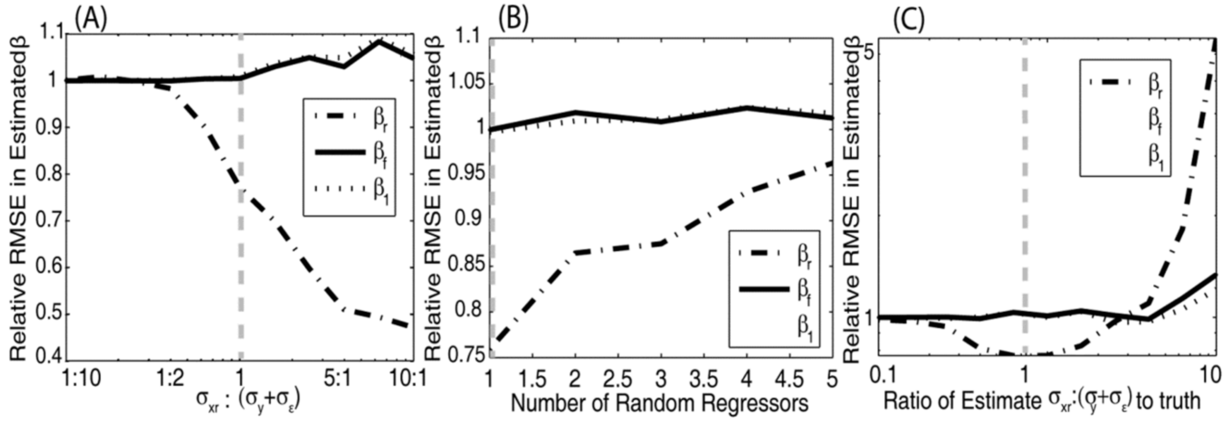

Figure 3.4 The rRMSE of model II to OLS for each estimated coefficient ($\boldsymbol{\beta_r}$, $\boldsymbol{\beta_f}$, $\boldsymbol{\beta_1}$) are plotted as a function of the ratio of the true standard deviations, $\boldsymbol{\sigma_{x_r}}$: $\boldsymbol{\sigma_y}$(A), the number of random regressors, $\mathbf{X}_r^{(j)}$ (B) and the accuracy of the ratio estimate (C). (Note, y-axis were visually optimized for each figure and are not common across A, B, and C.) With increasing $\boldsymbol{\sigma_{x,r}}$: $\boldsymbol{\sigma_y}$ ratios, model II regression has increased relative accuracy in βr estimates compared to OLS with increasing $\boldsymbol{\sigma_{x,r}}$: $\boldsymbol{\sigma_y}$ ratios. In (C), the estimated ratio of$\boldsymbol{\sigma_{x,r}}$: $\boldsymbol{\sigma_y}$was allowed to deviate from the simulated value, $\boldsymbol{\sigma_{x,r}}$: $\boldsymbol{\sigma_y}$= 1. The common simulation shared in (A, B, C) is indicated by a gray line.

Baltimore Longitudinal Study on Aging (BLSA) neuroimaging project consisting of 79x95x69 voxels with 0.94x0.94x1.5 mm resolution (Resnick, Goldszal et al. 2000). To create repeated measurements for regression calibration, we simulated two observed regressor images for each subject. OLS and model II were applied to the first set of measurements. To test the regression methods, a simple model with a single random regressor and constant was used, $\boldsymbol{y} = \beta_r \boldsymbol{x}_r + \beta_1 + \boldsymbol{\varepsilon}$. Inside the caudate region: $\beta_r = 1.5$, inside the putamen: $\beta_r = -0.6$, and for all other brain regions: $\beta_r = 0$. The observed regressand images and the observed regressor images were generated by adding zero mean Gaussian noise across subjects and the standard deviation used for each voxel was chosen to maintain an SNR around 15 for each image (SNR is defined as the mean signal divided by the standard deviation of noise).

Figure 3.5 presents the simulated images, the $\hat{\beta}_r$ from each method, and the t-map for the regressor images (the spatial map of the test statistic for the null hypothesis). For clarity, the number of replicated measurements used for regression calibration was two and the estimated and true ratio for $\sigma_{x,r} : \sigma_y$ was one for model II regression. The simulation method was repeated 10 times to create 10 imaging datasets (each of the 10 imaging datasets contained 40 x 2 $\boldsymbol{x}_r$ images and 40 $\boldsymbol{y}$ images). The

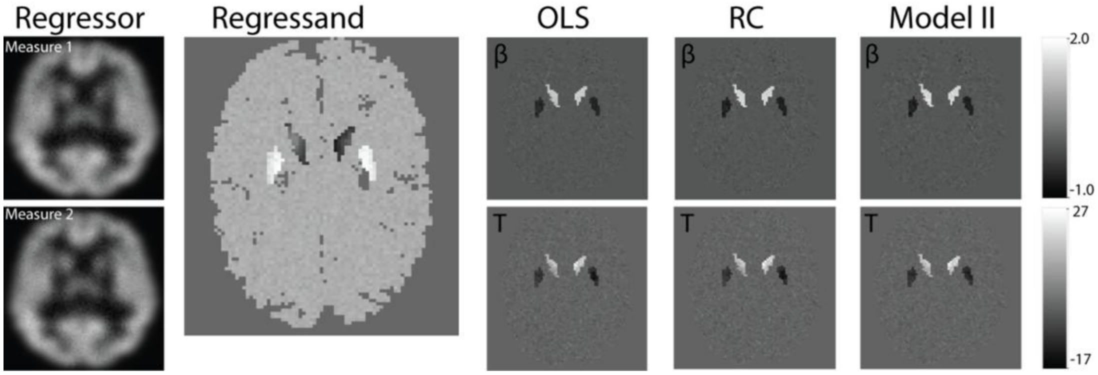

Figure 3.5 Simulated imaging associations. The first column shows two noisy regressor images for one subject, the first measurement is used in OLS regression and model II regression while both of them are used in regression calibration. The second column shows the paired noisy regressand image. The estimated coefficient β map and the positive t-map are displayed in the upper right-hand row of and lower left-hand row respectively. The β and t-maps are shown for OLS, regression calibration (RC) and model II regression. The differences between the methods are difficult to appreciate in a visual comparison; please see Table 1 for a quantitative summary.

Table 3.1 Comparison of methods based on simulated imaging data

	Outside (β=0)		Inside Caudate (β=1.5)		Inside Putamen (β=-0.6)	
	FPR (%)	RMSE	FNR (%)	RMSE	FNR (%)	RMSE
OLS	0.1±0.008	0.05±0.0001	0	0.24±0.003	1.7±0.2	0.12 ±0.0015
RC	0.1± 0.006	0.06±0.008	0.04±0.05	0.11±0.002	1.5±0.2	0.08±0.001
Model II	0.07± 0.006	0.06±0.002	0	0.13±0.004	0.2±0.09	0.09± 0.001

The significance is calculated according to an uncorrected p-value, p<0.001.

average false positive rate (FPR), average false negative rate (FNR), and the root mean square error are calculated using the uncorrected p-value < 0.001. The results are summarized in **Table 3.1**.

In this simple model, both OLS and regression calibration control the type I error rate as expected (FP, Table 3.1). Meanwhile, regression calibration and model II regression improve the true positive rate as compared to OLS regression (100-FNR, **Table 3.1**). For the root mean square error, when the true coefficient is zero ($\beta_r = 0$), the OLS method slightly outperforms the regression calibration and model II regression; when the relationship between $\boldsymbol{x_r}$ and y exists ($\beta_r \neq 0$), both regression calibration and model II regression outperform OLS. Regression calibration is slightly superior to model II regression (but requires additional measurements).

Empirical Demonstration of Model II Regression

Image-on-image regression offers a direct opportunity to study associations between differing spatially located factors. As an illustrative example, consider potential correlations between gray matter (GM) tissue density (a structural measure) and PET signal (a measure of functional activity). A first model would associate tissue presence with greater functional signal. An analysis of modulating factors for this relationship (such as disease condition, intervention, or task) could reveal anatomical correlates of functional reorganization and shed light on the applicability of the structural-functional hypothesis.

Following this approach, we perform regression analysis of the relationship between anatomical MRI GM images and functional PET images (Beason-Held, Kraut et al. 2008). We used a sub-cohort of 23 healthy participants (14 M/9 F, 60-85 y/o at baseline). Each subject was studied annually for eight years with a T1-weighted MRI sequence (1.5T, GE Medical Systems, SPGR, 0.9375x0.9375x1.5 mm, 256x256x124 mm field of view) and PET data (GE 4096+ scanner, 15 slices of 6.5mm thickness, 60s). The baseline scan was denoted as year 1 and the last scan was denoted as year 9. The data were preprocessed with SPM5 (University College London, UK). The structural scans were normalized to MNI-space, segmented and smoothed (12 mm Gaussian kernel) to obtain smooth GM density images. PET images were normalized, smoothed (12 mm Gaussian kernel) to MNI-space, and calibrated for global blood flow measurements to form cerebral blood for measurements and normalized to [0 1] scalar.

Regression was performed in both directions in order to quantify both structure→function and function→structure relationships. The "structure" data was constructed by concatenating all smoothed gray matter data for year 1 and year 9 and all subjects, and the "function" data was constructed by concatenating all corresponding, smoothed, calibrated PET images. Hence, the regression model used one random regressor and one single constant. Note that this analysis is simplified to illustrate the use of these methods; a traditional application would also include confounds (age, gender, pre-existing conditions, year of scan, etc.) and an analysis of time courses and interaction terms. An extended characterization of the BLSA data is ongoing and beyond the scope of this work demonstrating statistical methods.

As is common in practice, only one measurement for each modality image is available and regression calibration cannot be applied. The model II $\sigma_{x,r}\colon\sigma_y$ ratio is estimated following the method in (Rajan, Poot et al. 2010), with the window size for the method selected according to the image modality. The raw data and the resulting OLS and model II regression lines for a single voxel comparison are displayed in **Figure 3.6**. The model II regression model is symmetric, i.e., the mapping PET→GM is the inverse of the mapping GM → PET while OLS is not. The corresponding estimated variances for model II are also smaller than the corresponding estimated variances in OLS forward regression and OLS inverse regression.

Conclusions

Properly accounting for error is essential for valid parameter estimation and statistical inference. Herein, we have demonstrated that a consideration of observation variability is feasible within the confines of a design matrix paradigm. Furthermore, we can readily consider simultaneous treatment of parameters with measurement error alongside traditionally defined fixed parameters. Our formulation of "random observations" remains within the context of a "fixed effects" model as the $\boldsymbol{\beta}_r$ are deterministic parameters, as opposed to the classic "random effects" model where parameters are stochastic. These two approaches are complementary and could be combined for an appropriate experimental framework. Extension of the random regressor concept to time series, hierarchical, and other complex model designs is a fascinating area for continuing research.

We have observed substantial improvements in model fit using regression calibration and model II regression as opposed to OLS (**Figure 3.3A**, **Figure 3.4A**). While performance of regression calibration and model II were robust to increasing model complexity (**Figure 3.3B**, **Figure 3.4B**) and prior estimation of observation variability (applicable to model II only, **Figure 3.4C**), the improvements were not universal. When the OLS is appropriate (i.e., $\boldsymbol{\sigma}_x^2 \ll \sigma_y^2$), OLS performs comparable to regression calibration (**Figure 3.3A**) and for model II there was a slight increase in observed error relative to OLS (**Figure 3.4A**); however, as the relative variance in $\boldsymbol{x}_r$ increased, the OLS assumption of fixed regressors becomes increasingly violated and increased variance could be observed in the OLS estimates. We emphasize that the simulations neglect the many of nuances of empirical studies (e.g., correlations among regressors); these results should be viewed as guide to when alternative regression approaches should be evaluated as opposed to definitive evidence that a particular method is best suited.

On average, differences between the advanced statistical methods and OLS may be subtle as seen in the parameter estimates and statistical maps in **Figures 3.5 and 3.6**. As **Table 3.1** highlights, OLS appears quite robust against false positives; however, this may come at the expensive of reduced power and accuracy. In practice, it is important to consider the impact of the inference approach on individual voxels, as local findings drive interpretation and consideration of the multiple sources of measurement error may lead to different parameters estimates and/or different significance values. Model II and regression calibration can be further adapted to accommodate diverse regression scenarios. For example, a non-parametric method would be more suitable when the distribution assumptions are unknown (Nichols and Holmes 2002) while robust regression methods could be applied in the case of outliers

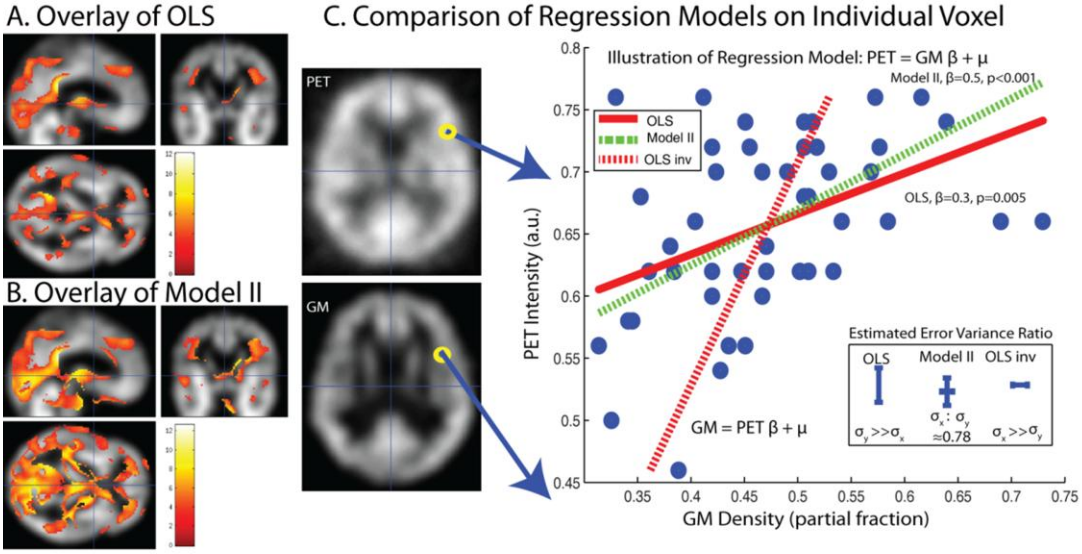

Figure 3.6 Model II and OLS multi-modality regression analysis. OLS (A) and Model II (B) lead to distinct patterns of significant differences (p<0.001, uncorrected) when applied to identical empirical datasets and association models. Inspection of single voxel: PET vs grey matter MRI (GM) illustrates the reasons for the different findings (C). The GLM model used for the forward mapping is $\boldsymbol{y} = \boldsymbol{x_r}\boldsymbol{\beta_r} + \boldsymbol{\beta_1}$, where $\boldsymbol{y}$ represents PET image intensities and $\boldsymbol{x_r}$ represents GM normalized image intensities. On the left-hand side of (C), example images of PET and GM are shown, along with the location of the single example voxel whose regression analysis is displayed in the right-hand plot. The individual data points (blue circles) were fit using OLS (red lines) and model II regression (green dashed line). Note that the inverse mapping for OLS (red dash) is not the same as the forward mapping (red solid line). The model II mapping was found to be reversible and can be represented by the same line. Resulting error bars and corresponding $\boldsymbol{\sigma_{x,r}}$: $\boldsymbol{\sigma_y}$ value estimates are compared between OLS and model II in the lower right-hand insert.

(Huber and Ronchetti 1981; Diedrichsen and Shadmehr 2005; Yang, Beason-Held et al. 2011).

Important areas for further development of model II and regression calibration remain. For parametric regression, other error models besides Gaussian may be more appropriate for specific imaging modalities and warrant further consideration. For model II, interpreting the ratio of model variances is a subject of active consideration as one must consider the potential impact of both the imaging variability and model fit error in multiple dimensions. As discussed, we currently approximate this combined quantity as proportional to the imaging variability alone. Developing methods to relax this assumption would greatly aid in generalization of this approached.

Our presentation of model II regression herein is inverse consistent, provides a logical framework for exploring relationships in multi-modal image analysis, and can help model relative uncertainty in imaging methods. Regression calibration accounts for measurement error and has been shown to improve on OLS in massively-univariate imaging scenarios. The requirement of repeated measurements for regression calibration makes model II a more likely choice for imaging data where repeat scans are uncommon. These methods are readily available in open source as plug-ins for the SPM package. Sample datasets and program documentation are available with the program for download.

CHAPTER IV

EVALUATION OF STATISTICAL INFERENCE ON EMPIRICAL RESTING STATE FMRI

Introduction

The exploration of relational changes within the human brain plays an important role in understanding brain structure and function, helping with disease prediction and prevention. Neuroscience and patient care have been transformed by quantitative inference of spatial-temporal brain correlations in normal and patient populations with millimeter resolution and second precision using three-dimensional structural imaging (magnetic resonance imaging – MRI, computed tomography – CT) and functional imaging (positron emission tomography – PET, functional MRI – fMRI) (Matthews, Honey et al. 2006). Classical statistical approaches allow mapping of brain regions associated with planning/execution, response, and default mode behaviors (through task, event, and resting state paradigms, respectively) (Friston, Ashburner et al. 2007). When the brain is at rest (i.e., not task driven), functional networks produce correlated low frequency patterns of activity that can be observed with resting state fMRI (rs-fMRI). These correlations define one measure of functional connectivity which may be estimated by voxel-wise regression of activity in a region of interest (ROI) against that of the remainder of the brain (van den Heuvel and Hulshoff Pol 2010). The selected ROI is called seed. Connectivity analysis has been widely studied using rs-fMRI and seed method analysis (Bandettini, Jesmanowicz et al. 1993; Biswal, Yetkin et al. 1995). The sensitivity and specificity of connectivity inference techniques hinge upon valid models of the noise in the observed data. Yet, in the quest to evermore specifically map neural anatomy, cognitive function, and potential pathologies, the resolution limitations of the current generation of clinical MRI scanners are becoming painfully clear – especially in imaging of small structures (e.g., (Giove, Garreffa et al. 2004)). The next generation of 7T MRI scanners offers the possibility of greatly increased signal to noise ratio (SNR) along with higher contrast for functional activity (Hutchison, Leung et al. 2011). Yet, as the magnetic field strength increases, the effects of physiological noise (breath, local flow and bulk motion), susceptibility artifacts, and hardware induced distortion are increased (Hutton, Josephs et al. 2011). Hence, artifacts are an increased problem with fMRI at 7T over the current 3T and 1.5T scanners (Triantafyllou, Hoge et al. 2005).

Absolute voxel-wise MRI intensities (arbitrary values) are rarely used in isolation for inference – rather, the temporal and spatial patterns/correlations of changes over time are of primary interest. Statistical analyses enable inference of the probability that observed signals are not observed by chance (i.e., that there exist significant associations between the observed signals and model of brain activity). The techniques in wide-spread use are based on classical distributional properties (e.g., Gaussian noise models, auto-regressive temporal correlation, and Gaussian random fields) and have been shown to be reasonable for well-designed studies at traditional field strengths. Classical statistics here means least-squares centric approach that lies at the heart of the Statistical Parametric Mapping Matlab toolbox (Friston, Jezzard et al. 1994; Friston, Holmes et al. 1995). Note that for low SNR, the MRI noise follows a Rician distribution across an image (Gudbjartsson and Patz 1995; Wink and Roerdink 2006), the Rician distribution needs to be well considered to provide unbiased estimation when the temporal SNR is low (Rowe 2005; Zhu, Li et al. 2009). But for the rs-fMRI time series observations the temporal SNR is usually high enough (>3:1~5:1) so that the approximation of Gaussian distribution assumption is reasonable (Gudbjartsson and Patz 1995). The discussion of ultra-low temporal SNR is beyond the scope of this paper. Violations of statistical assumptions threaten to invalidate or (at best) reduce the power of these experiments. Traditional validation guidance involves careful inspection of residuals and evaluation of distributional assumptions (Luo and Nichols 2003). When artifacts are detected, images must be excluded or the analysis approach must be modified. While imaging techniques continue to improve acquisitions in terms of spatial and temporal characteristics (i.e. resolution, signal characteristics, noise characteristics), it is uncertain if inevitable tradeoffs resulting in altered noise and artifact levels can be controlled or compensated for such that their overall impact will be truly negligible.

Increased ratio of physiological noise to thermal noise (Kruger and Glover 2001) may increase the artifacts on 7T fMRI images compared to 3T fMRI. As the prevalence of artifacts increases, the violations of the Gaussian distribution assumptions over all observations underlying the statistical model may also increase. In a recent pilot study, we investigated the distributional properties of resting state fMRI (rs-fMRI) at 3T and 7T (Yang, Holmes et al. 2012). Increasing static field strength from 3T to 7T provides increased signal and contrast, though this increase is commonly traded for improvements in spatial and temporal resolution. As such, the resulting data do not necessarily have the same noise structures, nor are they necessarily well-described by traditional Gaussian noise distribution assumptions. In fact, the 7T data presented here exhibited substantial non-Gaussian noise structure and spatial correlations not well-modeled by traditional approaches (as would be expected with data known to be susceptible to artifacts) (Triantafyllou, Hoge et al. 2005). The statistics literature is ripe with studies demonstrating “robust/resistant” analysis methods that mimic traditional analyses but are less sensitive to the impacts of artifacts and errors in distributional assumptions. For example, a robust empirical Bayesian estimation of longitudinal data is briefly discussed in (Gill 2000) in a non-imaging context and temporal artifacts have been considered for 3T fMRI by robust estimation of the covariance matrix of the regression errors (Diedrichsen and Shadmehr 2005). We combined these ideas to extend the traditional ReML approach to use a robust autoregressive model. Superior performance was demonstrated in simulation via specificity and sensitivity modeling (e.g., receiver operating characteristic characterization). When applied to empirical 7T fMRI data, clear differences in statistical parameter maps were observed between inferences based on classical and robust assumptions. Yet, there is a fundamental gap between noting empirical differences in statistical parametric maps and concluding that improvement occurred such that one inference method is more appropriate than another. The problem is illustrated on an fMRI dataset with a simulated artifact scan in **Figure 4.1**.

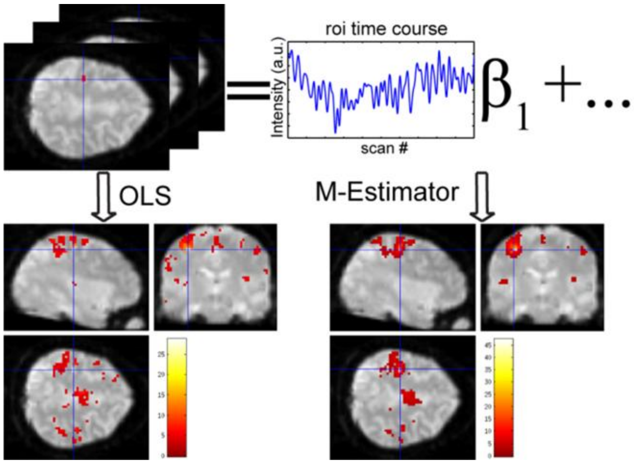

Figure 4.1 When different inference methods result in different connectivity maps, it is difficult to quantify which is more ‘valid.’ For example, connectivity of resting state fMRI can be analyzed by fitting region of interest’s (red mark) time course to all activity. A robust method reduces to influence of violations of distributional assumptions (artifacts), but also reduces statistical power. The focus of this work is how to evaluate the statistical parametric maps from different potential analysis approaches.

Statistical comparison of statistical maps (e.g., t-fields, F-fields, p-values) can be theoretically challenging given the difficulty in modeling distributional assumptions when the null hypothesis is rejected (Garrett, Holmes et al. 1992). When repeated datasets are available, one can measure the reproducibility of estimated quantities when inference is applied to each dataset separately (Genovese, Noll et al. 1997). Data-driven prediction and reproducibility metrics enable such quantitative assessments through resampling/information theory (Strother, Anderson et al. 2002). Prediction evaluates the degree (e.g., posterior probability) to which a model can assign correct class labels to an independent test set, while reproducibility measures the similarity (correlation coefficient) of activation maps generated from independent data sets. These techniques can be used to optimize acquisition protocols (LaConte, Anderson et al. 2003) and post-processing pipelines (Strother, La Conte et al. 2004) when true class labels are known. In a related manner, mutual information metrics between the patterns of task activity and image intensity (Afshin-Pour, Soltanian-Zadeh et al. 2011) can be used to assess relative predictability and reproducibility characteristics of the robust and classical inference methods. Yet, generalization of these approaches to generic rs-fMRI experimental designs within the general linear model paradigm (i.e., resting state fMRI, structural-functional association studies, etc.) is problematic, and to date, no methods have been proposed to quantify relative performance of rs-fMRI inference methods based on typically acquired datasets (i.e., without large numbers of repeated scans for a single subject).

Herein, we characterize empirical, finite sample performance by quantifying the consistency and resilience of empirical estimators under random data loss (i.e., decimation). These metrics are simple to compute, readily applied to compare estimators of differing types (robust, non-parametric, classical, etc.), and provide metrics that enable data-driven estimator selection. These efforts build on recent innovations in SIMulation and Extrapolation (Carroll, Ruppert et al. 2010) (i.e., SIMEX - the notion that the expected value of an estimator diverges smoothly with increasing noise levels; therefore, the mean degree of corruption can be estimated by extrapolating a trend of divergence when synthetic noise is added to empirical data) and randomized data subsampling. We apply this new technique to characterize ordinary and robust inference of rs-fMRI data. The proposed approach does not require acquisition of additional data and is suitable for evaluation on isolated datasets as well as group datasets.

Theory

Terminology

For consistency, we adopt the following notation. Scalar quantities are represented by italic, lower case symbols (e.g., σ^2). Vectors are represented by bold, italic, lower case symbols (e.g., $\boldsymbol{y}$). Matrices are bold, upper case symbols (e.g., $\boldsymbol{X}$). The symbol ~ is used to note “distributed as,” with N used to represent the multivariate Normal distribution. The term “artifacts” refers to unusual observations and the term “noise” is signal not of interest, which may due to physiological or thermal effects. The term “error” refers to the regression error which may or may not contain noise or artifacts.

Regression Model

Within this context, we focus on rs-fMRI data, which can be analyzed with an autoregressive model of order 1 (AR(1)) for a weakly stationary time series (Friston, Penny et al. 2002),

$$\boldsymbol{y}_i = \mathbf{X}\boldsymbol{\beta}_i + \boldsymbol{e}_i, \qquad \boldsymbol{e}_i \sim \mathcal{N}\left(\mathbf{0}, \sigma_i^2 \mathbf{V}\right) \tag{4.1}$$

where $\boldsymbol{y}_i$ is a vector of intensity at voxel i, $\mathbf{X}$ is the design matrix containing seed voxel time series, $\boldsymbol{\beta}_i$ is a vector of regression parameters at voxel i, and $\boldsymbol{e}_i$ is a non-spherical error vector. The correlation matrix $\mathbf{V}$ is typically estimated using Restricted Maximum Likelihood (ReML) method with a AR(1) correlation matrix structure, and $\boldsymbol{\beta}$ is estimated on the whitened data (i.e., the "OLS" approach). Alternatively, a robust estimator (e.g., the "Huber" M-estimator (Huber and Ronchetti 1981)) may be applied after whitening. Both the OLS and Huber methods are available within the SPM software (Yang, Beason-Held et al. 2011). Herein, we used the Huber method with the tuning constant chosen for 95% asymptotic efficiency when the distribution of observation error is Gaussian distribution (Holland and Welsch 1977).

Monte Carlo Assessment of Inference

Empirical characterization of inference performance when the true value is unknown is a circular problem – to quantify error, one must have a baseline against which to compare, but, to compute a baseline from empirical data, one needs an estimator. The SIMEX (Carroll, Ruppert et al. 2010) approach offers a seemingly implausible, but extraordinarily powerful, shortcut around the issue of unknown ground truth. The theoretical core of SIMEX is that the expected value of an estimator diverges smoothly with increasing noise level; therefore, the mean degree of corruption can be estimated by extrapolating a trend of divergence when synthetic noise is added to empirical data (Cook and Stefanski 1994). Assuming that the statistical methods under consideration are consistent (i.e., that estimates improve with increasing information), one can use the marginal sensitivity to information loss (e.g., increasing noise) to compute the expected estimator bias based on synthetic noise and a single dataset. SIMEX was developed as a

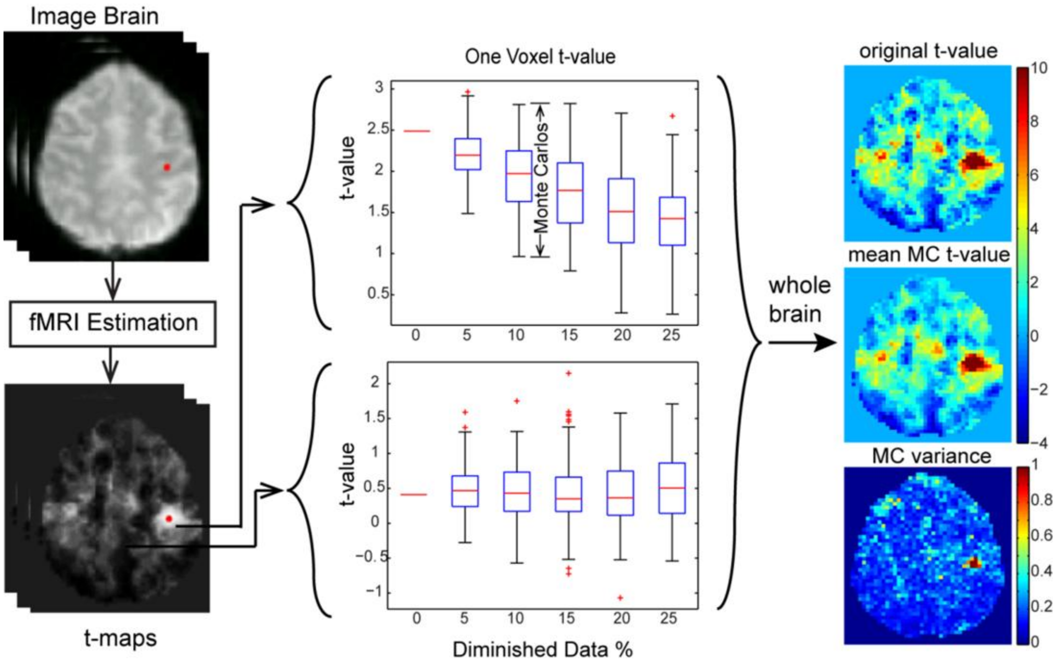

Figure 4.2 Representative one voxel t-values as data is randomly decimated. An rs-fMRI dataset is randomly diminished into N data size levels with M subsets in each level. Inference methods are applied to each subset to estimate voxel-wise t-maps. The highlighted point (left) indicates the rs-fMRI seed region.

general method that is highly adaptable, which has been extended into classification settings (Kuchenhoff, Mwalili et al. 2006) as well as applied in MRI diffusion tensor imaging (Lauzon, Crainiceanu et al. 2013). In the context of this study, it is not reasonable to add noise because the noise distributions are uncertain — especially in the context of artifacts.

If we apply the SIMEX assumption of smooth convergence to the problem of imaging inference with unknown noise / artifact distributions, we can probe the marginal reduction in sensitivity of an estimator by removing data. We define resilience as the ability of an inference method to maintain a consistent parametric map estimate despite a reduction in data. Over the time course of an rs-fMRI experiment (5-10 mins), the active brain regions vary. Hence, reproducibility of inferences based on sampled time periods (e.g., first versus second half) are not meaningful. Therefore, we focus on diminishing random data samples as opposed to structured temporal resampling. The number of diminished scans is small and Monte Carlo simulations procedures are used to estimate the mean marginal impact using many different randomly decimated data. Examples of subsampling for one voxel t-value are displayed in **Figure 4.2**.

The scans are randomly deleted after all pre-processing steps so that the changes of scan intervals do not affect the slice timing correction or low pass filtering. Recall that the temporal covariance of fMRI time series is estimated using ReML with a AR(1) correlation structure. To address the scan interval changes we modified the temporal correlation matrix according to the number of time points between every two image. In SPM, low frequency confounds are removed before estimation using residual formatting matrix. To address random data removal, we generated the low frequency filtering matrix for the whole data then deleted the time points corresponding to the scans removed.

Resilience

An intuitive way to assess the resilience of an inference method to a reduction in data might be to calculate the absolute value of the difference between the mean t-values (across Monte Carlo simulations) as a function of data size. However, this method will result in higher difference when the t-value with all data is high versus the t-value with all data is low as data reduction will universally pull t-values away from significance. Such an approach will strongly depend on the true effect size and the mean t-value cannot reflect the resilience to the artifacts if any (Yang, Kang et al. 2012). Hence, it is important to also consider the variance of the estimated parametric maps – we advocate evaluating the resilience in terms of consistency and variance.

Small reductions in data result in approximately linear reductions in t-value (due to smooth loss of power – not shown), so we advocate focusing on a specified diminished data size (e.g., randomly diminished by 10% and 20%) rather than on a large number of different data decimations. At a single data size with 10% decimation we have three parametric maps of data across all spatial locations; one t-map of the starting t-values, one t-map of the mean t-value from the Monte Carlo repetitions, and one variance map from the Monte Carlo repetitions. The right subplots in **Figure 4.2** show one slice of the t-map fields with the mean and the variance of the t-value over the subsamples.

Consistency assesses the bias of the computed parametric map of the decimated data relative to the same map computed with complete data. A priori, one would expect to see small reductions in parametric map values between the complete and decimated datasets due to power loss, but there would be few large changes as both classical and robust inference methods are reasonably unbiased. We summarize consistency by pooling information across all in-brain voxels using linear regression:

$$\begin{gathered} \boldsymbol{t}_{\overline{\boldsymbol{MC}}} = \beta_{mean} \times \boldsymbol{t}_{\boldsymbol{all}} + \boldsymbol{\epsilon} \\ r_{con} = \beta_{mean} - 1 \end{gathered} \tag{4.2}$$

where $\boldsymbol{t}_{\boldsymbol{all}}$ is a vector containing one t-value for each in-brain voxel where the t-value is estimated using the overall time series, $\boldsymbol{t}_{\overline{\boldsymbol{MC}}}$ is the mean t-value of all subsamples (across Monte Carlo iteration) and the slope β_{mean} reflects the pooled consistency (**Figure 4.3**). If the inference method is consistent, β_{mean} should be close to one and the fitting error would be small. The value of r_{con} can therefore be viewed as a reflection of bias with the sign indicating positive or negative bias and the R-squared can assess the

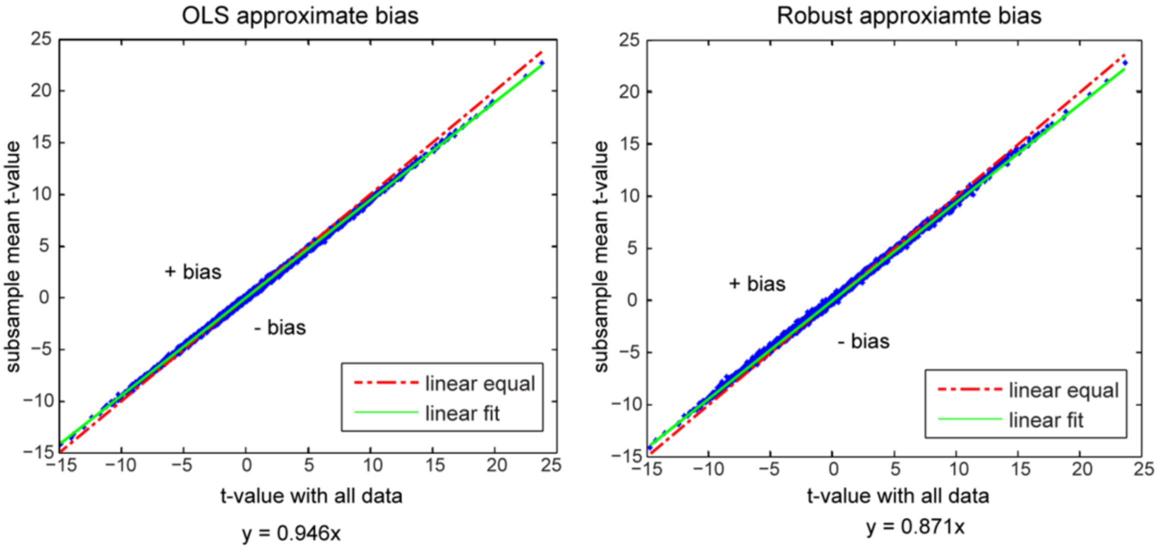

Figure 4.3 Illustration of consistency estimation. The mean t-value of random subsamples with 10% diminished data (vertical) is plotted versus the t-value with all data (horizontal). The left plot displays the OLS estimates and the right shows the M-estimates. The dashed line indicates equality ($y = x$); the data points above the dashed line have positive bias and the points below the dashed line have negative bias. The solid line is the estimated regression line from all the data points in each plot.

goodness of fit relative to the random error ($\boldsymbol{\epsilon}$). As we are losing data, we can expect lower t-values for significant voxels, thus β_{mean} will not equal one but should be close to one. Hence, a statistical test is not appropriate – we know the true distributions are different – rather, we must use the numerical value of β_{mean}in a qualitative assessment.

The variance of the Monte Carlo t-values can reflect how resistant an estimation method is to artifacts in the dataset. If a method is affected by artifacts, the variance will increase when artifacts exist. This is because the artifacts may appear in some subsamples while not in others which will result in varied t-value estimates. Although the inference method with overall smaller variances is more resistant to artifacts, the artifacts may exist only in some brain regions. These regional effects are difficult to detect from looking directly at a variance map as in **Figure 4.2**. To account for the influence of regional or a small number of artifacts, the variances from two inference methods are compared directly (**Figure 4.4**). The collection of variance values across spatial locations for inference method-1, $\boldsymbol{var1_{MC}}$, (e.g., OLS) is plotted against those of inference method-2, $\boldsymbol{var2_{MC}}$, (e.g., robust) and their variances are compared by

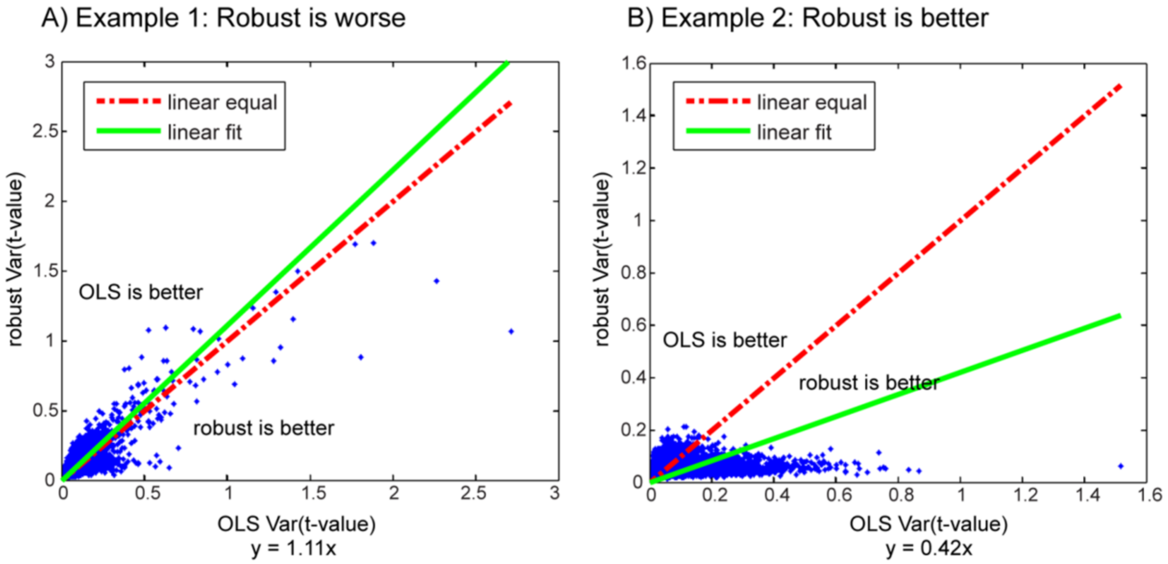

Figure 4.4 t-value variance comparison. The variance of subsample t-values with 10% diminished data from OLS (horizontal) and robust estimation (vertical) methods are compared. The dashed line ($y = x$) shows when the variance from the OLS and robust method are equal. The solid line is the estimated regression line.

computing the slope β_{var} between them under consideration of random error ($\boldsymbol{\epsilon}$).

$$\boldsymbol{var2_{MC}} = \beta_{var} \times \boldsymbol{var1_{MC}} + \boldsymbol{\epsilon} \tag{4.3}$$

If these two methods are equivalent, the slope will be close to one. If the slope is larger than one, the method-1 is superior; on the contrary, if the slope is smaller than one, the method-2 is superior. The slope is impacted when one method contains spatial locations with larger variance which may due to the impact of artifacts. **Figure 4.4** displays two examples, and **Figure 4.5** presents corresponding brain images indicating the spatial locations where the variance from robust estimation is lower than the variance from OLS.

When using robust regression, we have to pay the price that it is 95% asymptotically Gaussian when there are no artifacts (i.e., 5% reduction in power). To compare the OLS and robust variance, we selected the variance from OLS as $\boldsymbol{var1_{MC}}$ and the variance from Huber estimation as $\boldsymbol{var2_{MC}}$ in (equation (4.3)), if the slope is less than one, the robust estimation is practically superior to OLS estimation.

Methods and Results

Simulation Experiments

Simulation Data

To investigate the properties of our method in a controlled environment, we first performed simulation experiments. In the simulation a simple regression model is used:

$$\boldsymbol{y_{obs}} = \beta_0 + \boldsymbol{x_{obs}} \times \beta_1 + \boldsymbol{e}, \boldsymbol{e} \sim N(\boldsymbol{0}, \sigma^2 \boldsymbol{V}) \tag{4.4}$$

where $\boldsymbol{x_{obs}}$ simulates the seed voxel time course, β_1 is the connectivity coefficient, and $\boldsymbol{V}$ is the normalized covariance matrix. $\boldsymbol{x_{obs}}$ is simulated from an empirical 3T unsmoothed fMRI data. (The source fMRI data are preprocessed through slice timing correction, realignment and normalized to MNI space.) We selected a voxel inside the right motor cortex and acquired its time series. The time series was demeaned to simulate the value of $\boldsymbol{x_{obs}}$. The mean value of the original (un-demeaned) voxel time course is about 905 (arbitrary intensity units), and the standard deviation is about 11. So we designed the simulated temporal signal to noise ratio (TSNR) to be 80:1 (≈ 905/11). We used $\beta_1 = 0.8$ for other voxels ($\beta_1 = 1$ for the seed voxel) inside the right side of gray matter (GM), $\beta_1 = -0.6$ for the voxels inside the left side of GM, and $\beta_1 = 0$ for the rest of the brain. The mean value of a white matter voxel time course is about 800 so β_0 is set to make the whole brain mean value to be around 800. We calculated $\boldsymbol{y_{true}}$ based on these parameters.

$$\boldsymbol{y_{true}} = \beta_0 + \boldsymbol{x_{obs}} \times \beta_1 \tag{4.5}$$

For each voxel, we generated Gaussian noise $N(\boldsymbol{0}, \sigma^2 \boldsymbol{I})$ for the first time point, and then convolved the Gaussian noise to generate autoregressive noise with correlation 0.2 across time. σ is chosen to make TSNR ≃ 80:1. We added the autoregressive noise to the $\boldsymbol{y_{true}}$ to simulate fMRI images. In this simulation, the AR(1) parameter is constant for all voxels, but the estimation method does not estimate the AR(1) parameter, instead, it estimates the covariance matrix of the temporal noise (Worsley, Liao et al. 2002). The seed voxel time course is considered as the design matrix.

To simulate artifacts, we created an outlier scan by adding Gaussian noise with higher standard

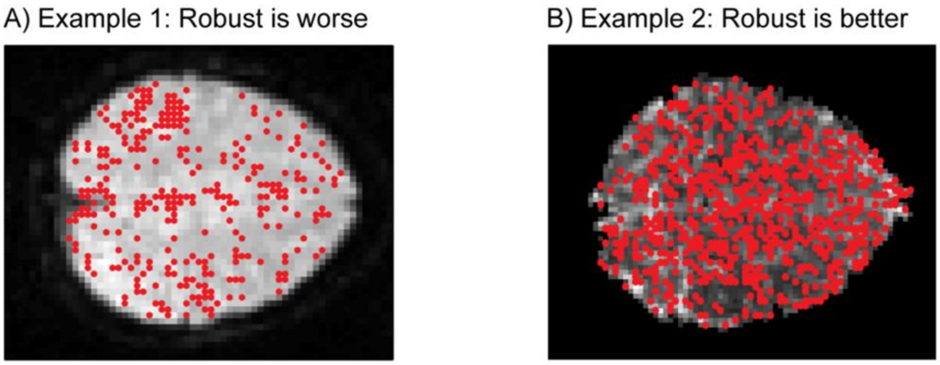

Figure 4.5 t-value variance comparison corresponding brain images. The red points represent where variance from robust estimation that is lower than the variance from OLS. (A) corresponds to **Figure 4.4A** and (B) corresponds to **Figure 4.4B**.

deviation to a simulated scan. The outlier scan is chosen with the highest seed intensity and the noise is only added to a region of the brain. The added Gaussian noise is zero mean with standard deviation 10 times the standard deviation of the original simulated scan. Other simulated scans are kept the same.

Subsample Parameters and Simulation Result

User controlled parameters for implementing our method include (i) the number of Monte Carlo simulations and (ii) the diminished data size. To decide the number of Monte Carlo simulation and the diminished data size, we evaluate their influence on the consistency and the variance on simulation data as shown in **Figure 4.6**. To decide the number of Monte Carlo simulations, we plotted the r_{con} for the OLS consistency (equation (4.2)) and $1 - \beta_{var}$ for the variance comparison (equation (4.3)). Plots were made for two variance comparison across five similar simulations when 10% of scans are randomly diminished. When there is only one Monte Carlo simulation, the range of the boxplot is large and it decreases as the number of Monte Carlo simulations increase.

The consistency from the OLS and the robust (not shown in the figure) inference are similar with and without outliers if the number of Monte Carlo simulations is over 50. When there are no outliers, the variance slope β_{var} is greater than one, which suggests the OLS method is better than the robust method. When there are outliers, the β_{var} is less than one, which suggests the robust method is better than the OLS method.

Empirical Experiments

Empirical Data

For illustrative purposes, we consider 15 distinct in vivo datasets.

Seven representative healthy subject rs-fMRI acquired at 3T were downloaded from http://www.nitrc.org/projects/nyu_trt/ (197 volumes, FOV = 192 mm, flip θ = 90°, TR/TE = 2000/25 ms, 3x3x3 mm, 64x64x39 voxels) (Shehzad, Kelly et al. 2009). Prior to analysis, all images were corrected for slice timing artifacts and motion artifacts using SPM8 (University College London, UK). All time courses were low pass filtered at 0.1 Hz using a Chebychev Type II filter, spatially normalized to MNI space, spatially smoothed with an 8 mm FWHM Gaussian kernel, linearly detrended, and de-meaned. The 3T data are smoothed, a typical pre-processing step for 3T fMRI to increase spatial SNR. Two voxels inside the right primary motor cortex for each subject were manually selected as the region of interest (ROI) by experienced researchers through exploring the unsmoothed images and comparing with the standard atlas. The design matrix for the general linear model was defined as the ROI time courses, the six estimated motion parameters, and one intercept. To create whole-brain connectivity maps, every labeled brain voxel underwent linear regression using the design matrix.

Eight normal subjects were studied at 7T after informed consent. Subjects were instructed to both close their eyes and rest. Briefly, the resting state images were acquired for 500s using single shot

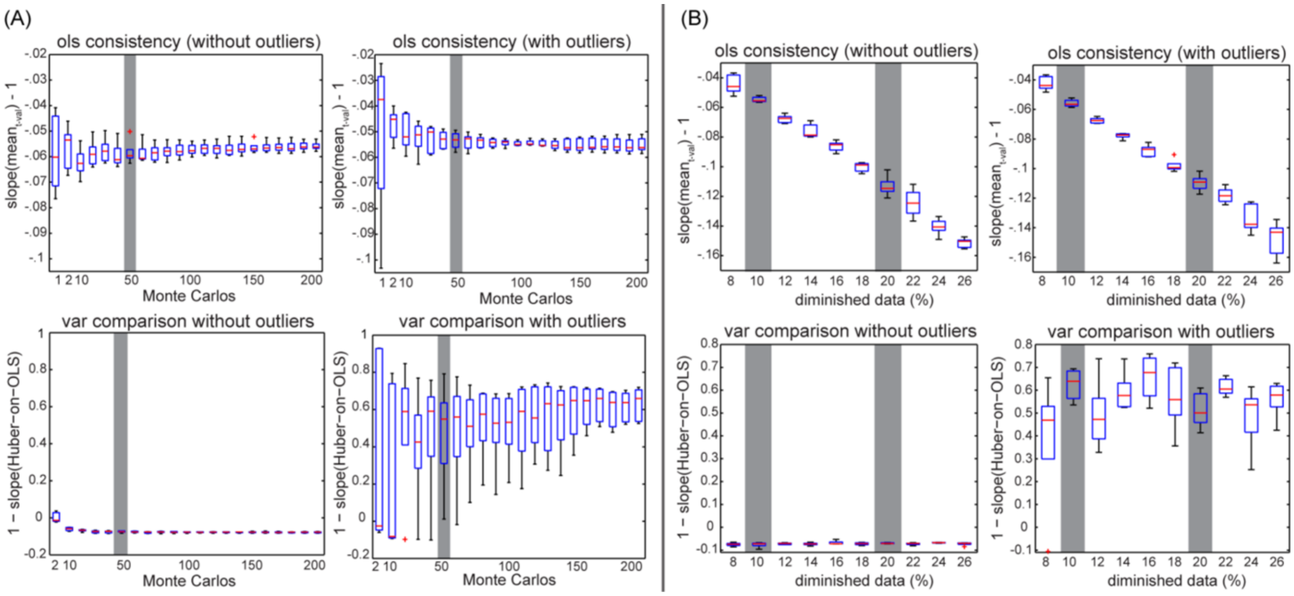

Figure 4.6 Influence of resilience parameter. (A) shows the impact of the number of Monte Carlo repetitions with 10% diminished data. (B) shows the impact of the diminished data size level when we performed 50 Monte Carlos each time. The OLS consistency plots display the slope $\beta_{mean} - 1$ in equation (4.2). The variance comparison plots display $1 - \beta_{var}$, where β_{var} is the slope of variance from robust estimation on OLS. “With\without artifacts” indicates if there are simulated outlier scans in the simulation.

gradient echo EPI (500 volumes, FOV = 192mm, flip θ = 53.8°, TR/TE = 1000/28ms, SENSE factor = 3.92, full k-space acquisition, resolution 2x2x2mm, 96x96x13 voxels). Prior to analysis, all images were corrected for slice timing artifacts and motion artifacts using SPM8 (University College London, UK). All voxels' time courses were low pass filtered at 0.1Hz using a Chebychev Type II filter, linearly detrended, and de-meaned. The 7T data are not smoothed because the spatial SNR are much higher in 7T than 3T, and we are only interested in single subject results that smoothness is not necessary. The seed voxel was defined as a single manually selected voxel located in primary motor cortex along the central sulcus that was also significantly activated by a conventional finger tapping task contrasting bimanual, self-paced finger tapping against a resting condition (FWE corrected, $p < 0.05$, minimum cluster size = 1 voxel) (Newton, Rogers et al. 2012). The design matrix for the general linear model was defined as the seed voxel time course, the six estimated motion parameters and the intercept. Each voxel's BOLD time course underwent linear regression of the design matrix to create connectivity maps.

Comparative Analysis of Classical and Robust Inference

rs-fMRI analysis was performed on each dataset in SPM8 using ordinary "OLS" and robust ("Huber") regression methods. For each decimation level (10% and 20%), 50 Monte Carlo simulations were performed. For each Monte Carlo simulation, a subset of either 90% or 80% of the total data was randomly selected, the OLS and Huber estimation methods were applied, and the t-maps on the coefficient for the ROI time courses were stored. Consistency was assessed between the mean of the decimated maps and the map using all data, while the relative variance was assessed between Monte Carlo simulations with each method. For the resilience variance metrics, OLS was on the x-axis and Huber on the y-axis. Note that both OLS and Huber were fit to the same subsample of the data (i.e., the random subsamples are paired).

Empirical Results

Representative statistical parametric maps from OLS and robust regression of one 3T fMRI and two 7T fMRI are displayed in **Figure 4.7**. Noted that the results are shown on uncorrected p-value without cluster size threshold, the difference between results from OLS and robust regression may be more obvious than the results after cluster threshold. The results of all subjects are shown in **Table 4.1**. Next, we discuss how the qualitative metrics may be used for selection of inference method.

- For subjects 1 to 7, 10, 13, the consistency estimates are similar and close to zero for both OLS and Huber, while the R2 value is high. This indicates that neither method is particularly biased by the decimation process. The variance matrices for both 10% and 20% decimation are negative except 20% decimation for subject 3, which indicates that OLS was more resilient than Huber. The variance metric for 20% decimation for subject 3 is positive, but the value is too small (<0.01) to show any interest.

  – Conclusion: Robust inference is not necessary; OLS is preferable. When there are no outliers, the OLS method is better than the robust method because the robust method is only approximately 95% as statistically efficient as the OLS method. The evaluation conclusion indicates that there are relatively few outliers in this data set.

- For subjects 8, 15, the consistency estimates are similar and close to zero for both OLS and Huber, and the R2 value is high. Hence, neither method is particularly biased by the decimation process. The variance metric for both 10% and 20% decimation is positive, which indicates that Huber was more resilient than OLS.

  – Conclusion: Robust inference yields higher resilience and should be used. It indicates that there are outliers in this data set. Since the probability of the existence of outliers increase at 7T compared to 3T it is not surprising that the robust inference method is better than the OLS.

- For subjects 9, 11, 12, 14, the consistency estimates are similar and close to zero for both OLS and Huber, and the R2 value is high. Hence, neither method is particularly biased by the decimation process. The biases at 20% decimation are always higher and the R2 value is lower than at 10% decimation for all these subjects. For subject 9, 12, 14, the variance metric for the 10% decimation is

Table 4.1 Summary of Resilience Measures for All Subjects

subject	diminished data	Method	Consistency		Variance
			$\beta_{mean} - 1$	R^2	$1 - \beta_{var}$
1 (3T)	10%	OLS	-0.016	0.992	-0.113
		Huber	-0.018	0.991	
	20%	OLS	-0.050	0.984	-0.179
		Huber	-0.049	0.981	
2 (3T)	10%	OLS	-0.078	0.975	-0.067
		Huber	-0.071	0.980	
	20%	OLS	-0.138	0.950	-0.244
		Huber	-0.133	0.951	
3 (3T)	10%	OLS	-0.019	0.989	-0.083
		Huber	-0.022	0.990	
	20%	OLS	-0.051	0.961	0.006
		Huber	-0.053	0.965	
4 (3T)	10%	OLS	-0.108	0.965	-0.034
		Huber	-0.110	0.962	
	20%	OLS	-0.189	0.888	-0.067
		Huber	-0.195	0.882	
5 (3T)	10%	OLS	-0.040	0.983	-0.123
		Huber	-0.044	0.973	
	20%	OLS	-0.095	0.946	-0.013
		Huber	-0.101	0.939	
6 (3T)	10%	OLS	-0.074	0.968	-0.165
		Huber	-0.076	0.970	
	20%	OLS	-0.161	0.898	-0.148
		Huber	-0.169	0.891	
7 (3T)	10%	OLS	-0.074	0.964	-0.052
		Huber	-0.076	0.963	
	20%	OLS	-0.140	0.911	-0.056
		Huber	-0.142	0.904	
8 (7T)	10%	OLS	-0.054	0.999	0.579
		Huber	-0.057	0.999	
	20%	OLS	-0.119	0.997	0.280
		Huber	-0.120	0.995	
9 (7T)	10%	OLS	-0.051	0.995	0.029
		Huber	-0.049	0.995	
	20%	OLS	-0.115	0.964	-0.106
		Huber	-0.107	0.968	
10 (7T)	10%	OLS	-0.091	0.996	-0.373
		Huber	-0.107	0.981	
	20%	OLS	-0.175	0.986	-0.389
		Huber	-0.177	0.963	
11 (7T)	10%	OLS	-0.066	0.999	-0.328
		Huber	-0.056	0.998	
	20%	OLS	-0.126	0.995	0.177
		Huber	-0.106	0.995	
12 (7T)	10%	OLS	-0.125	0.980	0.550
		Huber	-0.089	0.987	
	20%	OLS	-0.176	0.962	-0.158
		Huber	-0.156	0.964	
13 (7T)	10%	OLS	-0.037	0.997	-0.250
		Huber	-0.031	0.997	
	20%	OLS	-0.050	0.990	-0.088
		Huber	-0.033	0.989	
14 (7T)	10%	OLS	-0.170	0.980	0.285
		Huber	0.050	0.968	
	20%	OLS	-0.223	0.962	-0.054
		Huber	0.038	0.932	
15 (7T)	10%	OLS	-0.059	0.996	0.220
		Huber	0.012	0.977	
	20%	OLS	-0.113	0.990	0.169
		Huber	-0.046	0.959	

variance metric for the 10% decimation is negative while the variance metric for the 20% decimation is positive. The mixed results indicate that neither method is clearly superior and that careful data inspection is warranted.

- Conclusion: Robust inference may be desirable, but OLS could be suitable. The similar performance of the robust and the OLS methods may due to the fact that there are outliers but the number is small. In that situation, the OLS is better in most brain regions but the robust inference is much better in some small regions. Both methods yield acceptable results.

Discussion and Conclusions

The proposed resilience metrics provide a quantitative basis on which to compare inference methods. The simulation results suggest that a comparison of methods based on resilience would yield similar conclusions as one based on the sensitivity and specificity matrix. Yet, resilience is accessible for empirical data, when the ground truth (necessary for sensitivity and specificity) is rarely known. It is reassuring to see that resilience also indicates that OLS would outperform the robust inference approach on the 3T dataset where few outliers exist. For the 7T dataset the robust approach would outperform OLS since the achievable signal to noise ratio increases and the propensity for artifacts increases.

In simulations, it is easy to construct realistic datasets demonstrating that classical assumptions are sufficient or insufficient. However, in reality, it is very difficult to assess the stability of the robust/non-robust decision to variations in artifacts. Hence, creating representative artifact-prone distributions is a substantial endeavor. It is possible to acquire a massive reproducibility dataset and use this dataset to produce a highly robust ground truth estimate. Given such data, one may map artifact distributions. However, such acquisitions are exceedingly resource intensive and may not be representative of other sites and/or acquisitions. Hence, generalization of artifact findings is problematic.

However, the proposed resilience consistency and variance metrics provide a quantitative basis on which to judge individual datasets, allowing one to evaluate suitability of particular inference mechanisms on initial pilot data. This could be done in case studies, or as part of multi-level analysis to evaluate the tradeoffs between improved power (when classical assumptions are met) and reduced susceptibility to artifacts, based on actual empirical data.

Consistency in statistics is defined as convergence in probability, i.e., a consistent estimator of parameter converges to its true value as sample size grows. However, in practice it is not feasible to prove the consistency of an estimator because the truth remains unknown. What we assessed in this paper is not the absolute consistency but rather the relative consistency as it related to resilience of estimator, which could be achieved when estimated values were relatively stable regardless of the amount of data used as

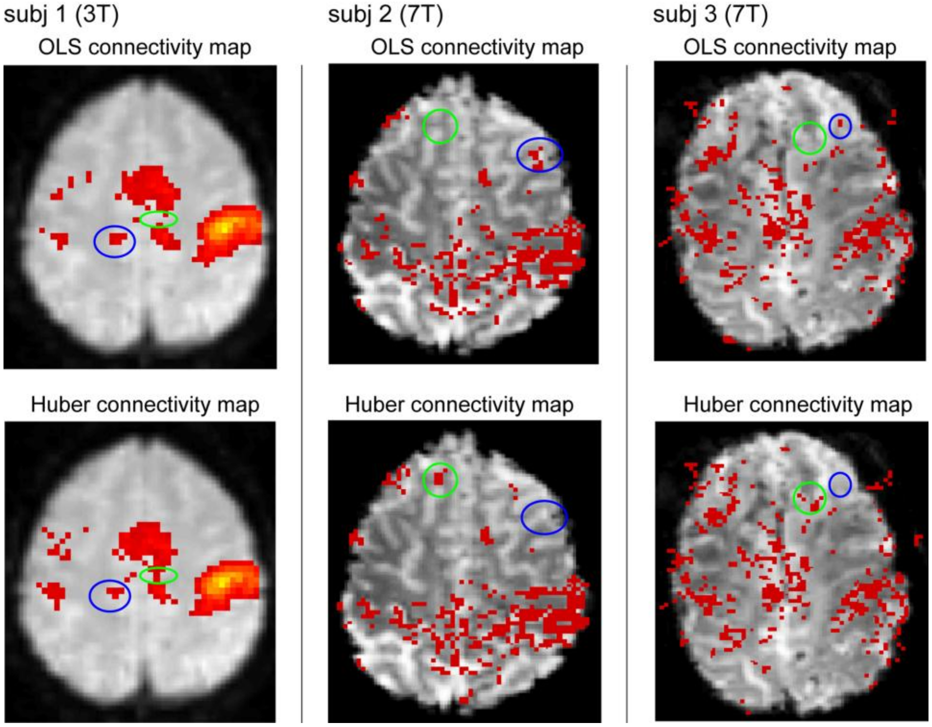

Figure 4.7 Representative overlays of significant for three subjects (columns) with OLS (top row) and robust (lower row) estimation methods. The connectivity maps are computed from one-sided t-test on the ROI time course coefficients ($p < 0.001$, uncorrected). The blue circle shows the OLS result is significant while the robust result is not or less significant. The green circle shows the robust result is significant while the OLS result is not or less significant. Resilience measures are tabulated in **Table 4.1**.

illustrated in Section II. We are not intending to empirically prove that the robust estimator is a absolutely consistent, but we want to show that estimates based on the robust estimator can be more (or less) consistent (or invariable) than another as decimated data are utilized.

Generally, the evaluation result depends on the number of effective outliers in the brain. In some cases, the evaluation is location dependent such that one estimator is good for one seed but not good for another, especially when outliers exist in one region but not in others. The resilience method still can be used to evaluate inference methods (e.g., see **Figure 4.5**), albeit without the increased power gained by pooling regions.

The random decimation procedure can be problematic for aspects of temporal estimation. We initially sought to examine split half (either temporal: early/late or frequency: even/odd). Unfortunately, both lead to systematic differences in the quantities being estimated by rs-fMRI. Temporal subsampling dramatically reduces the sensitivity to low-frequency correlations (which are of primary interest) and focuses analysis on short time periods with potentially different biological states. Frequency subsampling reduces the intrinsic sensitivity to temporal frequencies and imparts differing sensitivity to artifact. We examined a number of different random decimation methods and propose random decimation as a compromise between empirical power (i.e., we see differences where ones are known to exist) and ease of use.

Implementation of this approach requires the ability to decimate (remove) data randomly, loop over multiple possible data subsets, and calculate summary measures of the resulting statistical fields. With modern multi-core and cluster environments, a 50-100 fold increase in the computational burden of a traditional analysis is not typically problematic for off-line analysis. For example, the experiments presents one OLS analysis takes approximately 40 seconds and one Huber analysis takes 100 minutes. With proper parallelization, the total wait time would not be substantively longer than the time for a single analysis.

In conclusion, we have presented a novel approach for quantifying inference methods based on empirical data. We evaluated the resilience of the ordinary (OLS) and a robust method (23) for both simulated and empirical data. Resilience provides a simple, but powerful method for comparing a proxy for accuracy of inference approaches in empirical data where the underlying true value is unknown. Statistical theories characterizing finite sample statistical behavior are undergoing rapid and exciting developments in the statistical community. These statistical methods, encompassing SIMEX, bootstrap, and Monte Carlo approaches, offer the potential to understand both the uncertainty and bias in metrics estimated from imaging data. Given the abundance of computational power generally available, these methods can now be feasibly applied on routine basis.

CHAPTER V

WHOLE BRAIN FMRI CONNECTIVITY INFERENCE ACCOUNTING TEMPORAL AND SPATIAL CORRELATIONS

Introduction

Neuroscience and patient care have been transformed by quantitative inference of spatial-temporal brain correlations in normal and patient populations with millimeter resolution and second precision using functional MRI (fMRI) (Matthews, Honey et al. 2006). Classical statistical approaches allow mapping of brain regions associated with planning/execution, response, and default mode behaviors (through task, event, and resting state paradigms, respectively) (Friston, Ashburner et al. 2007). When the brain is at rest (i.e., not task driven), functional networks produce correlated low frequency patterns of activity that can be observed with resting state fMRI (rs-fMRI). These correlations define one measure of functional connectivity which may be estimated by regression of activity in a region of interest (ROI) against that of the remainder of the brain (van den Heuvel and Hulshoff Pol 2010).

Absolute voxel-wise MRI intensities (arbitrary values) are rarely used in isolation for inference – rather, the temporal and spatial patterns/correlations of changes over time are of primary interest. Statistical analyses enable *inference* of the probability that observed signals are not observed by chance (i.e., that there exist *significant* associations between the observed signals and model of brain activity). The techniques in wide-spread use (e.g., Gaussian noise models, auto-regressive temporal correlation) ignore spatial correlations in estimating model parameters (Friston, Holmes et al. 1994). Ignoring intrinsic spatial correlation will underestimate standard errors, leading to Type I errors in the presence of positive spatial correlation or Type II errors in the presence of negative spatial correlation (Dubin 1988). Traditionally, pre-processing and post-processing steps in the statistical parametric mapping pipeline partially account for the spatial correlations. For example, data are spatially smoothed with a Gaussian kernel before estimation (Worsley, Marrett et al. 1996) and the correlation is taken account in the inference procedures through random field theory (Worsley, Evans et al. 1992).

Recently, Kang et al. (Kang, Ombao et al. 2012) proposed a spatio-spectral mixed-effects model to overcome the main barrier of incorporating spatial correlations in fMRI data analysis. This model consists of fixed and random effects that capture within ROI correlations and between ROI correlations. The authors demonstrated capturing the spatial and temporal correlation through simulation and empirical experiments, but the framework was limited to consideration of three ROIs.

Herein, we proposed new functional connectivity analysis models accounting both the temporal correlation and the spatial correlation for ROI-based and voxel-wise analysis.

ROI-based Spatio-spectral Mixed Effects Model

The ROI-based, mixed effects model can incorporate the voxel-wise general linear model and ROI connectivity results (**Figure 5.1**). We expand the Kang et al spatio-spectral mixed effects model for an arbitrary number of ROIs to a generalized model for the whole brain rs-fMRI connectivity analysis. Briefly, (1) the whole brain is shattered into small ROIs, (2) estimation is performed on each voxel accounting for within ROI and between ROI correlations, and (3) significance is inferred on the ROI level. We evaluate our model through simulation and empirical experiments on the whole gray matter.

Model

We consider the following general spatio-spectral mixed-effects model for rs-fMRI:

$$y_{cv}(t) = \beta_{cv}^{0} + (\beta_{c}^{s} + b_{cv})\boldsymbol{x}_{seed}(t) + \sum_{p=1}^{P} \beta_{cv}^{p}\boldsymbol{x}_{\boldsymbol{p}}(\boldsymbol{t}) + d_{c}(t) + \epsilon_{cv}(t) \tag{5.1}$$

where $y_{cv}(t)$ is the rs-fMRI intensity at voxel v in ROI c at time point t, $\boldsymbol{x}_{\boldsymbol{p}}$ can be any confounds, e.g., motion parameters, $t = 1, \dots, T$, $c = 1, \dots, C$, and $v = 1, \dots, V_c$ in ROI c. Additionally, $\boldsymbol{x}_{seed}$ is the mean time course within the seed region, β_{cv}^{0} is the constant value at voxel v in ROI c across time, β_{c}^{s} is the connectivity between the seed ROI and ROI c, β_{cv}^{p} $(p = 1, \dots, P)$ is the coefficient associated with the p-

th confounder at voxel v in ROI c, b_{cv} is a zero-mean voxel-specific random deviation of the seed connectivity within an ROI c and this random deviation is assumed to be independent across ROIs, $d_c(t)$ is a zero-mean ROI-specific random effect which models the remaining connectivity of all other ROIs after regression of the seed ROI connectivity, and $\epsilon_{cv}(t)$ is noise that takes into account intra-voxel temporal correlation.

Under the assumption of the stationary error series $\{\epsilon_{cv}(t)\}$, the spectrum, analogous to temporal covariance matrix in the time domain, is a diagonal matrix in the Fourier domain. Therefore, we transform the model in the time domain to the frequency domain. Let the Fourier coefficients of the series $\{x_{seed}(t)\}$,$\{x_p(t)\}$, $\{d_c(t)\}$, and $\{\epsilon_{cv}(t)\}$ be $x_{seed}(\omega), x_p(\omega), d_c(\omega)$ and $\epsilon_{cv}(\omega), (\omega = \omega_1, \omega_2, \dots, \omega_T)$, respectively. Then, using matrix notation in the frequency domain,

$$\boldsymbol{y}(\omega) = X(\omega)(\boldsymbol{\beta} + \boldsymbol{b}) + K\boldsymbol{d}(\omega) + \boldsymbol{\epsilon}(\omega) \tag{5.2}$$

where $\boldsymbol{y}(\omega) = \left[y_{11}(\omega), \dots, y_{1V_1}(\omega), y_{21}(\omega), \dots, y_{CV_C}(\omega)\right]^T$ is a $V_{tot} \times 1$ response vector at a frequency ω, ($V_{tot} = \sum_{c=1}^{C} V_c$, V_c is the number of voxels in ROI c), $X(\omega) = [\mathbb{I}_{V_{tot}} \otimes x_{seed}(\omega), \mathbb{I}_{V_{tot}} \otimes$

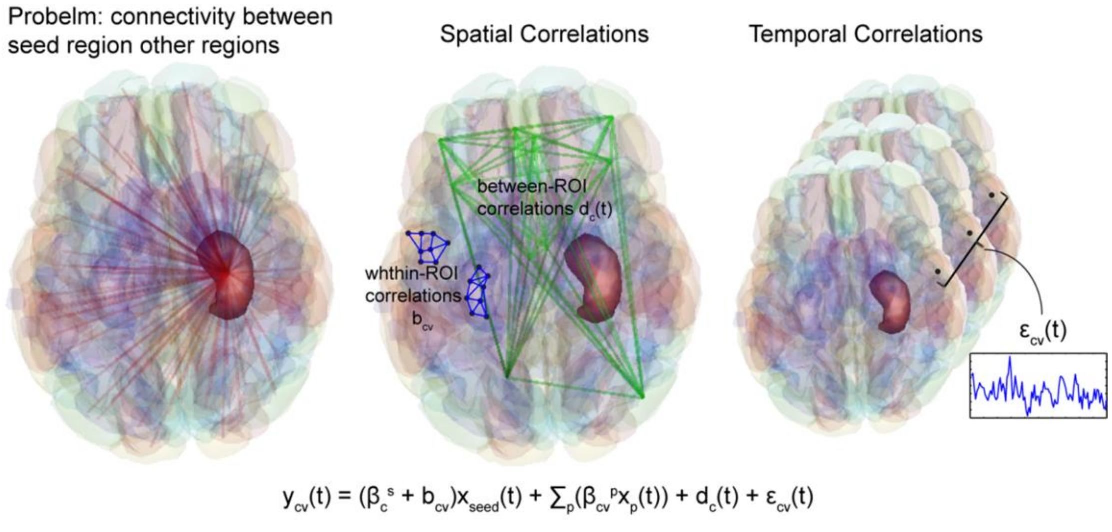

Figure 5.1 ROI-based spatial temporal model. Our goal is to discover the connectivity between a seed region and every other region in the brain. Spatial correlations model within ROI correlations and inter-ROI correlations – these are not typically addressed in rs-fMRI. Temporal correlations are voxel-wise correlations across time – these are typically addressed in rs-fMRI analysis.

$x_0(\omega), \mathbb{I}_{V_{tot}} \otimes x_1(\omega), \dots, \mathbb{I}_{V_{tot}} \otimes x_P(\omega)]$, $\mathbb{I}_n$ denotes an $n \times n$ identity matrix, $\boldsymbol{\beta} = \left[\boldsymbol{\beta^s}, \boldsymbol{\beta^0}, \boldsymbol{\beta^1}, \dots, \boldsymbol{\beta^P}\right]^\top$ is a $V_{tot}(P+2) \times 1$ vector, $\boldsymbol{\beta^s} = [\beta_1^s, \dots, \beta_1^s, \beta_2^s, \dots, \beta_2^s, \dots, \beta_C^s]^\top$, $\boldsymbol{\beta^p} = \left[\beta_{11}^p, \beta_{12}^p, \dots, \beta_{1V_1}^p, \beta_{21}^p, \dots, \beta_{2V_2}^p, \dots, \beta_{CV_c}^p\right]^\top$ for $p \in \{0,1,\dots,P\}$, $\boldsymbol{b} = \left[b_{11}, b_{12}, \dots, b_{1V_1}, b_{21}, \dots, b_{CV_C}, 0, \dots, \dots, \dots, 0\right]^\top$ is a $V_{tot}(P+2) \times 1$ vector, $\boldsymbol{b}_c^* = \left[b_{c1}, b_{c2}, \dots, b_{cV_c}\right]^\top \sim \mathcal{N}(0, \Sigma_{bc})$, $\boldsymbol{d}(\omega) = [d_1(\omega), \dots, d_C(\omega)]^\top$, $d_j(\omega) = d_j^R(\omega) + i d_j^I(\omega)$. Note that $\mathcal{N}(\mu, \tau)$ denotes a Gaussian distribution with mean $\mu$and variance τ, and $\boldsymbol{d^j}(\omega) \sim \mathcal{N}\left(0, \Sigma_d^j(\omega)\right), j \in \{R, I\}$, $\boldsymbol{d^R}(\omega)$ and $\boldsymbol{d^I}(\omega)$ are independent where R and I denote the real and imaginary part of a complex number, respectively. $K = K_1 \oplus K_2 \oplus \dots \oplus K_C$, where $\oplus$ denotes direct sum and $K_j = [1, \dots, 1]^\top$ is a vector of length V_j whose elements are all one, $j = 1, \dots, C$. $\boldsymbol{\epsilon}(\omega) = \left[\epsilon_{11}(\omega), \dots, \epsilon_{1V_1}(\omega), \epsilon_{21}(\omega), \dots, \epsilon_{CV_C}(\omega)\right]$ and $\boldsymbol{\epsilon}(\omega) = \boldsymbol{\epsilon^R}(\omega) + i\boldsymbol{\epsilon^I}(\omega)$. *N.b.* $[\boldsymbol{\epsilon^R}(\omega), \boldsymbol{\epsilon^I}(\omega)]^\top \sim N\left(0, \frac{1}{2} f(\omega) \mathbb{I}_{2V_{tot}}\right)$, where $f(\omega)$ is the spectrum at frequency ω.

Estimation

We define $\boldsymbol{\gamma_{cv}} = [\gamma_{cv}^s, \beta_{cv}^0, \beta_{cv}^1, \dots, \beta_{cv}^P]^\top, \gamma_{cv}^s = \beta_c^s + b_{cv}^s$. The ordinary least square (OLS) estimator of $\boldsymbol{\gamma}$ is

$$\widehat{\boldsymbol{\gamma}} = \left[\sum_{k=1}^{T} X^\top(\omega_k) X(\omega_k)\right]^{-1} \left[\sum_{k=1}^{T} X^\top(\omega_k) \boldsymbol{y}(\boldsymbol{\omega_k})\right] \tag{5.3}$$

Now we need to estimate $\boldsymbol{\beta^s}$ and $\boldsymbol{b}$. To simplify, rewrite $\boldsymbol{\beta^{s*}} = [\beta_1^s, \beta_2^s, \dots, \beta_C^s]^\top, \boldsymbol{b}^* = \left[b_{11}, b_{12}, \dots, b_{1V_1}, b_{21}, \dots, b_{CV_C}\right]^\top$, $\Sigma_b = \Sigma_{b1} \oplus \Sigma_{b2} \oplus \dots \oplus \Sigma_{bC}$, and $\widehat{\boldsymbol{\gamma}}^s = K\boldsymbol{\beta^{s*}} + \boldsymbol{b}^*$**.**

To estimate $\boldsymbol{\beta}$, we do not need to estimate the exact value of $\boldsymbol{b}$ but the covariance. The covariance of $\boldsymbol{b}$ can be estimated using spatial variogram (Banerjee, Carlin et al. 2004). If we used empirical variogram estimation, the estimation of Σ_b will only depends on the variance of $\widehat{\boldsymbol{\gamma}}^s$ across voxels within each ROI, which can be noisy. We model the spatial dependence using an exponential variogram and estimate the parameters using restricted maximum likelihood (Lark and Cullis 2004).

$$\widehat{\boldsymbol{\beta}}^{s*} = \left[K^{\top}\widehat{\Sigma_b}^{-1}K\right]^{-1}[K^{\top}\widehat{\Sigma_b}^{-1}\widehat{\boldsymbol{\gamma}^{s}}] \tag{5.4}$$

Estimation of $Cov(\boldsymbol{d}(\omega))$ and $f(\omega)$

Define $z_{cv}(\omega) = y_{cv}(\omega) - X(\omega)\boldsymbol{\gamma_{cv}}$. $z_{cv}(\omega)$ can be expressed as $d_c(\omega) + \epsilon_{cv}(\omega)$.

$$\widehat{\mathrm{Var}}(d_c(\omega)) = \left[\frac{1}{N(V_c)}\right]\sum_{v\neq v'}\{\widehat{\mathrm{Cov}}(z_{cv}(\omega), z_{cv'}(\omega))\} \tag{5.5}$$

where given locally stationary spatial process within an ROI, we compute the variance of $\boldsymbol{z_c}(\omega)$ at each frequency, which guarantees that the estimated variance is always greater than or equals to zeros.

When $c \neq c'$,

$$\widehat{\mathrm{Cov}}(d_c(\omega), d_{c'}(\omega)) = \widehat{\mathrm{Cov}}\left(\bar{y}_c(N(\omega)), \bar{y}_{c'}(N(\omega))\right) \tag{5.6}$$

where $\bar{y}_c(\cdot)$ denotes the average of y across all the voxels in ROI c and $N(\omega)$ denotes the frequencies around a frequency ω. The size of neighborhood of a frequency ω, i.e., $N(\omega)$, can be arbitrarily chosen between 1 and $T/2$ and we choose $T/8$.

The resulting covariance matrix of $\boldsymbol{d}(\omega)$ is guaranteed to be semi-positive definite. The spectrum for the real part or imaginary part is

$$\hat{f}^{j}(\omega) = [1/V_{tot}]\sum_{c=1}^{C}\sum_{v=1}^{V_c}\{\widehat{\mathrm{Var}}(z_{cv}(\omega)) - \hat{\sigma}_{d_c}^2\} \tag{5.7}$$

where $\hat{f}^{j}(\omega) = \frac{1}{2}f(\omega), j \in \{R, I\}$, using either the real parts or the imaginary parts of $z_{cv}(\omega)$ and $\widehat{\mathrm{Var}}(d_c(\omega)) \equiv \hat{\sigma}_{d_c}^2$, respectively. Then, a more robust estimator of the spectrum will be $\hat{f}(\omega) = \frac{1}{2}\left(\hat{f}^{R}(\omega) + \hat{f}^{I}(\omega)\right)$.

Estimation of $Cov(\widehat{\boldsymbol{\beta}})$

One of the limitations of the spatio-spectral mixed effects model in (Kang, Ombao et al. 2012) is the procedure for estimating $\mathrm{Cov}(\widehat{\boldsymbol{\beta}})$ scales quadratically with the number of ROIs. Since we are interested in the coefficients for the seed time course $\boldsymbol{\beta}^{\boldsymbol{s}*}$, we can simplify the covariance equations to perform the analysis on the whole brain. From OLS estimation, $\mathrm{Cov}(\widehat{\boldsymbol{\gamma}})$ is:

$$\mathrm{Cov}(\widehat{\boldsymbol{\gamma}}) = \left[\sum_{k=1}^{T} X^T(\omega_k)X(\omega_k)\right]^{-1}\left[\sum_{k=1}^{T} X^T(\omega_k)\mathrm{Cov}\big(\boldsymbol{y}(\boldsymbol{\omega_k})\big)X(\omega_k)\right]\left[\sum_{k=1}^{T} X^T(\omega_k)X(\omega_k)\right]^{-1} \tag{5.8}$$

The $\mathrm{Cov}(\widehat{\boldsymbol{\gamma}})$ can be arranged so that each regressor is separated: $\mathrm{Cov}(\widehat{\boldsymbol{\gamma}}) = \begin{bmatrix} \mathrm{Cov}(\widehat{\boldsymbol{\gamma}}^s) & \Sigma(\widehat{\boldsymbol{\gamma}}^s, \widehat{\boldsymbol{\gamma}}^{0\sim P}) \\ \Sigma(\widehat{\boldsymbol{\gamma}}^s, \widehat{\boldsymbol{\gamma}}^{0\sim P}) & \mathrm{Cov}(\widehat{\boldsymbol{\gamma}}^{0\sim P}) \end{bmatrix}$, from which we can write the covariance of the estimated seed coefficients as

$$\mathrm{Cov}(\widehat{\boldsymbol{\beta}}^{\boldsymbol{s}*}) = \left[K^T\widehat{\Sigma_b}^{-1}K\right]^{-1} K^T\widehat{\Sigma_b}^{-1}\mathrm{Cov}(\widehat{\boldsymbol{\gamma}}^S)\widehat{\Sigma_b}^{-1}K\left[K^T\widehat{\Sigma_b}^{-1}K\right]^{-1} \tag{5.9}$$

Let's define terms to further simplify equation (5.9) to achieve computational efficiency:

(1.) $\boldsymbol{x}(\boldsymbol{\omega}) = [x_{seed}(\omega), x_0(\omega), x_1(\omega), \dots, x_P(\omega)]$

(2.) $X^* = [\boldsymbol{x}(\boldsymbol{\omega_1}) \quad \boldsymbol{x}(\boldsymbol{\omega_2}) \quad \cdots \quad \boldsymbol{x}(\boldsymbol{\omega_T})]^T$,

(3.) $\left({X^*}^T X^*\right)^{-1}\left(\sum_{k=1}^{T}\left(x_{seed}(\omega)^2\big(\boldsymbol{x}(\boldsymbol{\omega_k})^T\boldsymbol{x}(\boldsymbol{\omega_k})\big)\right)\right)\left({X^*}^T X^*\right)^{-1} = A, \left({X^*}^T X^*\right)^{-1} = G,$

(4.) $\left(\left({X^*}^T X^*\right)^{-1}\boldsymbol{x}(\boldsymbol{\omega_k})^T\boldsymbol{x}(\boldsymbol{\omega_k})\left({X^*}^T X^*\right)^{-1}\right) = H(\omega_k),$

(5.) $\left({X^*}^T X^*\right)^{-1}\sum_{k=1}^{T}\big(f(\omega_k)\boldsymbol{x}(\boldsymbol{\omega_k})^T\boldsymbol{x}(\boldsymbol{\omega_k})\big)\left({X^*}^T X^*\right)^{-1} = Q,$

(6.) $A = \{a_{i,j}\}, G = \{g_{i,j}\}, H(\omega_k) = \{h(\omega_k)_{i,j}\}, Q = \{q_{i,j}\}.$

Defined an operator $sum(\mathbf{M})$ adds up all the elements in a matrix $\mathbf{M}$. Then after simplification and using the notations (1.) – (6.) above, we arrive at:

$$\mathrm{Cov}(\widehat{\boldsymbol{\beta}}^{s*}) = a_{11}\begin{bmatrix} sum\left(\widehat{\Sigma_{b1}}^{-1}\right) & 0 & 0 \\ 0 & \ddots & 0 \\ 0 & 0 & sum\left(\widehat{\Sigma_{bC}}^{-1}\right) \end{bmatrix}^{-1} + \sum_{k=1}^{T}\left(h(\omega_k)_{11}\widehat{\Sigma_d}(\omega_k)\right) + \hat{q}_{11}\begin{bmatrix} sum\left(\widehat{\Sigma_{b1}}^{-2}\right) & 0 & 0 \\ 0 & \ddots & 0 \\ 0 & 0 & sum\left(\widehat{\Sigma_{bC}}^{-2}\right) \end{bmatrix} \tag{5.10}$$

Inference

The t-test can be performed based on the estimated coefficient parameters and the covariance. Since we considered both the spatial correlations and the temporal correlations, the standard errors are not underestimated. Since there are more than one ROI, it is still necessary to do multiple comparisons corrections. Two widely used multiple correction methods are random field theory (RFT) and false discovery rate (FDR). RFT is based on the estimation of number of resels which is not suitable here. FDR is based on the p-value order which is reasonable here. Herein, we employed the FDR method for the inference on the whole brain ROIs.

Methods and Results

Simulation

We simulated rs-fMRI images from gray matter (GM) labels with one seed ROI and 95 other ROIs. One ROI was selected as the seed ROI. The mean connectivity coefficient for each ROI was randomly chosen from {-0.8, 0, 0.8} and no confounds are included. The connectivity coefficient for each voxel is the mean coefficient plus a zero-mean voxel-specific correlated random effect with standard deviation 0.1. The number of voxels and the coordinates vary from ROI to ROI but the within ROI Euclidian distance correlation structures are the same (i.e., the variogram function is the same). The between ROI covariance is defined by a positive semi-definite matrix in which the mean correlation was 0.2859, and minimum and maximum were -0.3652 and 0.8821, respectively. The temporal correlation was modeled by an autoregressive model (AR(1)) with the model coefficient of 0.3. The temporal signal to noise ratio (SNR) was simulated from 10 to 100 with the step size 10. The temporal SNR is defined as the ratio between mean intensity of the images to the standard deviation of the noise across time. It is noteworthy that the SNR mentioned here is the temporal SNR that is typically high in rs-fMRI experiments. For each SNR level, 100 Monte Carlo simulations were performed. We calculated the false positive rate (FPR) and the false negative rate (FNR) while controlling FDR at 0.05. The accuracies of estimated ROI connectivity coefficient $\widehat{\boldsymbol{\beta}}^{\boldsymbol{s}}$, within ROI covariance $\hat{\Sigma}_b$, and between ROI correlations were evaluated with root mean square error (RMSE) (**Figure 5.2)**.

The RMSE of $\boldsymbol{\beta}^{\boldsymbol{s}}$ decreases exponentially as the SNR increases. The FPR of FDR correction is under control for all SNR settings. The FNR of FDR is 1 when SNR is very low (SNR = 10), then it decreases exponentially and reaches a low level when SNR is high. The RMSEs of Σ_b and Σ_d decrease exponentially as SNR increases.

The widely accepted seed-based method in which the time series in each ROI are averaged across voxels and functional connectivity is defined as correlation between a seed time series and the average time series in an ROI, was also applied to the simulated data at SNR = 80. Because of high SNR, the conventional method results in FNR = 0 as our method does. However, in terms of FPR, the spatio-spectral mixed effects model outperforms the conventional approach, i.e., FPR of 0.0327 from the conventional approach and 0.0287 from our method. This 12 percent gain in FPR confirms that ignoring

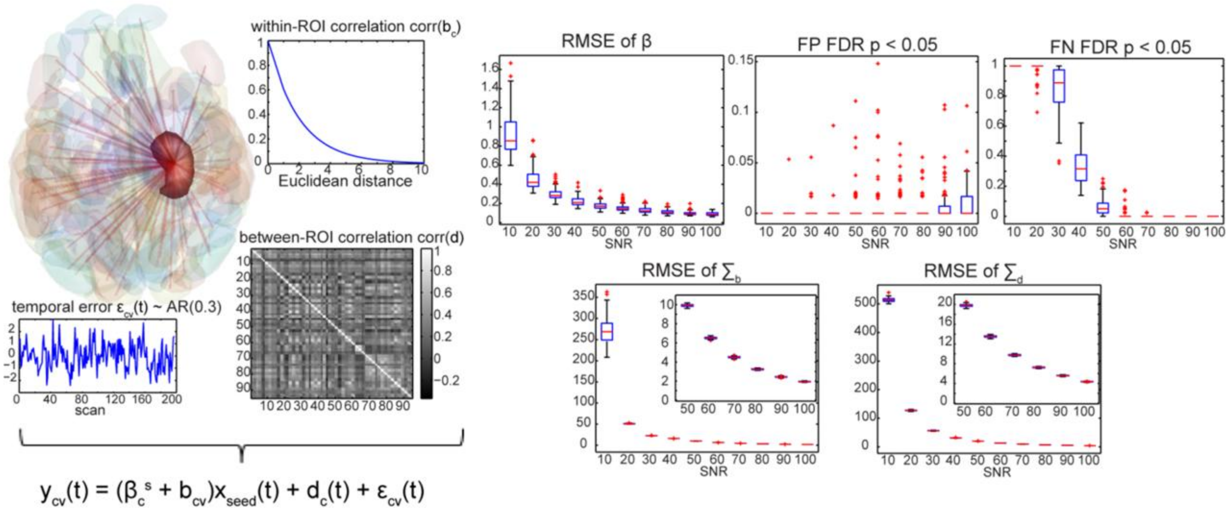

Figure 5.2 Simulation setting and results. The left part displays the setting of the simulation experience. The red region is selected as the seed region, and our interest is the connectivity between the seed region to every other 95 regions. The within ROI correlation is plotted as a function of Euclidean distance, the between ROI correlation is a 95 by 95 matrix, and the temporal error follows the AR(1) model with 0.3 correlation. The RMSE of $\boldsymbol{\beta}^{\boldsymbol{s}}$, Σ_b and Σ_d, the FP and FN with FDR correction are plotted in the right part as a function of SNR. The RMSE plots of Σ_b and Σ_d are enlarged for SNR from 50 to 100.

the underlying positive correlation in an ROI tends to inflate false positive findings

To further improve estimation accuracy, we considered incorporating a connectivity prior for the ROIs. In the above simulations the between ROI correlations $\hat{\Sigma}_d$ could be decomposed in three components as shown in **Figure 5.3**. We used these three components (but not their magnitudes) as a basis for $\hat{\Sigma}_d$ in the estimation for 100 Monte Carlo simulations when SNR is 80 and compared the results with the previous results. In **Figure 5.3**, the box plots labeled as 'no components' are our previous results and the box plots labeled as 'components' using the prior information to estimate the between ROI-correlations. As expected, the estimation of $\hat{\Sigma}_d$ becomes more accurate while the estimation of $\hat{\boldsymbol{\beta}}^{\boldsymbol{s}}$ and $\hat{\Sigma}_b$ stay the same. Employing the component priors reduces FPR but increases FNR compared to 'no component'. However, the gain and loss in terms of FPR and FNR seem to be negligible. This simulation results demonstrate that utilizing additional information enhances estimation accuracy in terms of RMSE, given that the prior information of between-ROI functional connectivity is accessible and reliable.

Empirical Data Analysis

To illustrate that our spatio-spectral model can be used in empirical studies, we applied the model on a public 3T dataset with 25 healthy subjects. The rs-fMRI images acquired at 3T were downloaded

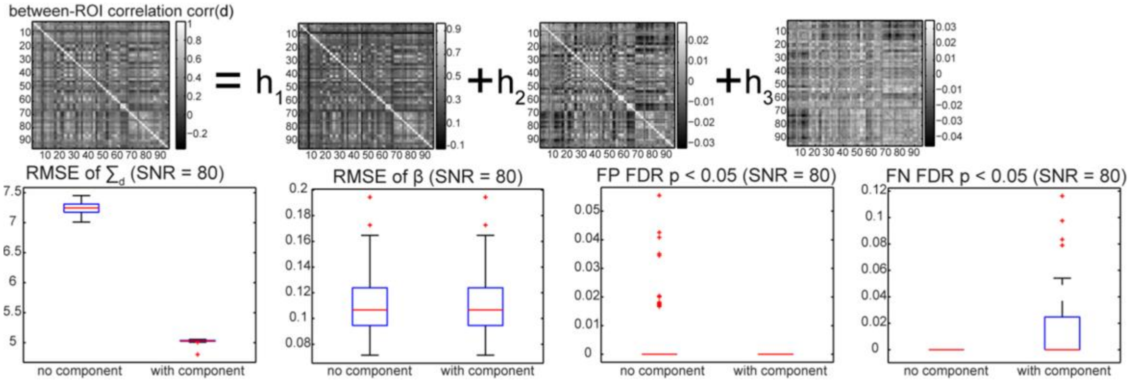

Figure 5.3 Estimation with component priors. The first line shows the predefined between ROI correlations can be decomposed by three components. The second line displays the results comparing the previous estimation without priors and the estimation with priors.

from http://www.nitrc.org/projects/nyu_trt/ (197 volumes, FOV = 192 mm, flip θ = 90°, TR/TE = 2000/25 ms, 3x3x3 mm, 64x64x39 voxels) (Shehzad, Kelly et al. 2009). Prior to analysis, all images were corrected for slice timing artifacts and motion artifacts using SPM8 (University College London, UK). All time courses were low pass filtered at 0.1 Hz using a Chebychev Type II filter, linearly detrended, and de-meaned. The corresponding high resolution T1-weighted anatomical images (FOV = 256mm, flip θ = 8°, TR/TE = 2500/4.3 ms, TI = 900 ms, 176 slices) were segmented to acquire label images (Asman and Landman 2012; Asman and Landman 2013). The right hippocampus was selected as the seed region for each subject. The six estimated motion parameters were used as confounds. The mean estimated seed connectivity coefficient $\widehat{\boldsymbol{\beta}}^{\boldsymbol{s}}$ and the mean between ROI correlations $\hat{\Sigma}_d$ across 25 subjects are shown in **Figure 5.4**. Although neither our multi-scale spatio-spectral random effects model nor the conventional approach (not presented here) can claim statistically significant functional connection to the seed region at FDR = 0.05, we demonstrate the capacity for performing the whole-brain analysis while properly considering both spatial and temporal correlations in rs-fMRI data.

Alternative Voxel-wise Spatio-temporal Model

Widely used voxel-wise functional connectivity analysis model addresses the temporal correlations well but ignores intrinsic spatial correlations (e.g., model implemented in SPM). Ignoring the

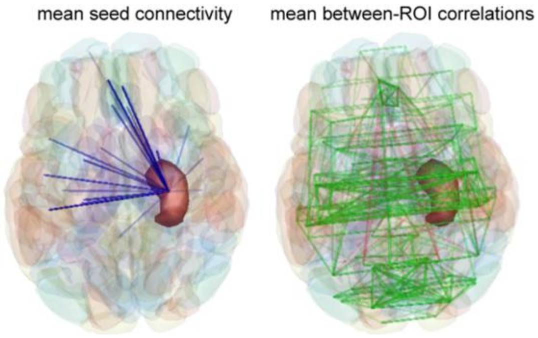

Figure 5.4 Empirical Results. The red region is the seed region. The left brain shows the mean connectivity coefficient across 25 subjects. The right brain shows the mean between ROI correlations across 25 subjects.

spatial correlations will still get an un-biased estimation of coefficients but will result in a biased statistical test. However, estimating the spatial covariance of all voxels within the brain is impractical that requires too much memory and too many degrees of freedom to get an accurate estimation. Therefore, we applied a spatial window for each voxel, the correlations within the window are considered for more accurate variance estimation (**Figure 5.5**).

Theory

In the voxel-wise spatio-temporal model, for each voxel, we consider the spatial correlations within its neighbor window w. Thus, for each voxel v inside window w, the voxelwise autoregressive fMRI model is

$$y_{wvAR}(t) = X_{AR}(t)\boldsymbol{\beta}_{wv} + e_{wvAR}(t) + \epsilon_{wvAR}(t) \tag{5.11}$$

where $y_{wvAR}(t)$ is the intensity for voxel v in window w at time t, $X_{AR}(t) = [\, x_0(t), \cdots, x_P(t)]$ contains the regressors at time t, $\boldsymbol{\beta}_{wv} = [\beta_{wv}^0, \beta_{wv}^1, \cdots, \beta_{wv}^P]^\top$, $\epsilon_{wvAR}(t)$ is the noise that takes into account temporal correlations within a voxel, $e_{wvAR}(t)$ is the noise that takes into account the voxel's neighbor spatial covariance. Assuming that the temporal correlations for each voxel are the same $\boldsymbol{\epsilon}_{wvAR} \sim \mathcal{N}(\mathbf{0}, \Sigma_{AR})$, we can estimate the temporal correlation using a restricted maximum likelihood estimation. After the estimation of temporal correlations, we can whiten the temporal noise and $\boldsymbol{\beta}_{wv}$ can be estimated for each voxel. Define $W = \Sigma_{AR}^{-1/2}$ as a temporal whitening matrix, then we can rewrite $W y_{wvAR}(t) = y_{wv}(t)$, $W X_{wvAR}(t) = X(t)$, $W \epsilon_{wvAR} = \epsilon_{wv}(t)$. After estimating the temporal correlations for each voxel, we have

$$y_{wv}(t) = X(t)\boldsymbol{\beta}_{wv} + e_{wv}(t) + \epsilon_{wv}(t) \tag{5.12}$$

where $\epsilon_{wv}(t)$ is a white noise and $e_{wv}(t)$ is used to model the spatial covariance for the window. i.e.,

$$\underset{v \neq v'}{\operatorname{corr}}\big(\epsilon_{cv}(t), \epsilon_{cv'}(t)\big) = 0, \underset{v \neq v'}{\operatorname{corr}}\big(e_{cv}(t), e_{cv'}(t)\big) = \rho_{vv'}^2(t) \tag{5.13}$$

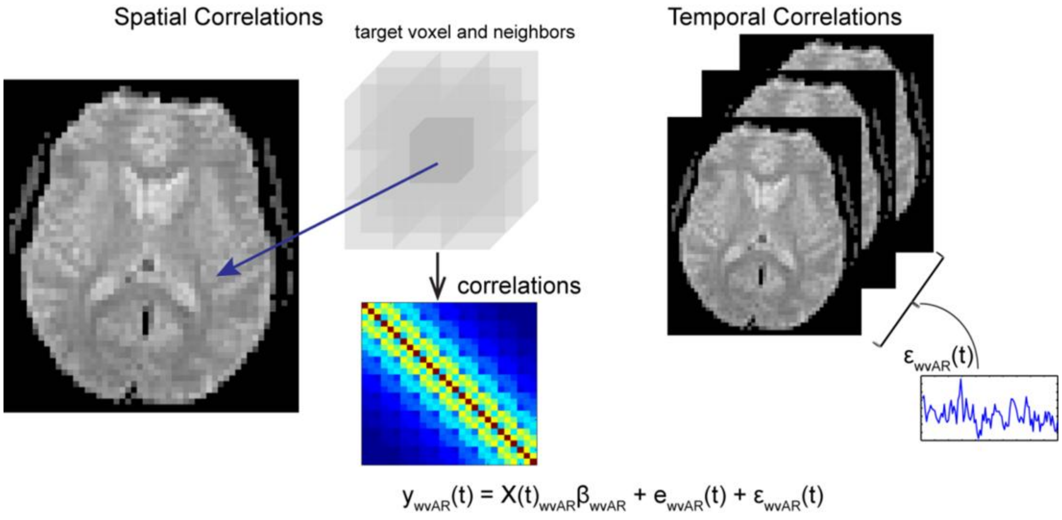

Figure 5.5 Voxel-wise spatio-temporal model. The spatial correlations are modeled for each voxel within its neighbor voxels. The gray box shows an example window containing 3×3×3 voxels. The centered voxel is the voxel under analysis, the spatial covariance within this window is considered in the centered voxel's general linear model. Temporal correlations are voxel-wise correlations across time, which are typically addressed in rs-fMRI analysis.

For all voxels within the window, we have

$$\boldsymbol{y}_w(t) = \boldsymbol{X}_w(t)\boldsymbol{\beta}_w + \boldsymbol{e}_w(t) + \boldsymbol{\epsilon}_w(t) \tag{5.14}$$

where $\boldsymbol{y_w}(\boldsymbol{t}) = \left[y_{w1}(t), y_{w2}(t), \cdots, y_{wV_w}(t)\right]^{\mathsf{T}}$, V_w is the number of voxels within window w. $\boldsymbol{X}_w(\boldsymbol{t}) = X(t) \otimes \mathbb{I}_{V_w}$, $\mathbb{I}_n$ denotes an $n \times n$ identity matrix, $\boldsymbol{\beta_w} = \left[\beta^0_{w1}, \beta^0_{w2}, \cdots \beta^0_{wV_w}, \beta^1_{w1}, \cdots, \beta^1_{wV_w}, \cdots, \beta^P_{w1}, \cdots, \beta^P_{wV_w}\right]^{\mathsf{T}}$is a $V_w \times (P+1)$ vector, $\boldsymbol{e_w}(\boldsymbol{t}) = \left[e_{w1}(t), e_{w2}(t), \cdots, e_{wV_c}(t)\right]^{\mathsf{T}}$, $\boldsymbol{\epsilon_w}(\boldsymbol{t}) = \left[\epsilon_{w1}(t), \epsilon_{w2}(t), \cdots, \epsilon_{wV_w}(t)\right]^{\mathsf{T}}$.

Assuming the spatial covariance is the same for each time point, the model can be simplified as

$$\underset{v\in w}{\mathrm{Cov}}\left(\boldsymbol{e}_w(\boldsymbol{t})\right) = \Sigma_e\,, \underset{v\in w}{\mathrm{Cov}}\left(\boldsymbol{\epsilon}_w(\boldsymbol{t})\right) = \mathrm{diag}\left(\sigma^2_{\epsilon_v}\right) \tag{5.15}$$

$$\underset{v\in w}{\widehat{\mathrm{Cov}}}\left(\boldsymbol{y}_w(t)\right) \equiv \underset{v\in w}{\widehat{\mathrm{Cov}}}(\boldsymbol{y}_w) = \hat{\Sigma}_e + \mathrm{diag}\left(\hat{\sigma}^2_{\epsilon_v}\right) \tag{5.16}$$

where Σ_e is a $V_w \times V_w$ matrix modeling the spatial covariance, $\mathrm{diag}\left(\sigma^2_{\epsilon_v}\right)$ denotes a $V_w \times V_w$ diagonal matrix with $\sigma^2_{\epsilon_v}$ in the diagonal corresponding to voxel v. Applying the assumption of intrinsic stationary, the spatial covariance can be estimated through nonparametric or parametric variogram estimation assuming that the correlation between two voxels depends on their distance. There are several widely used variogram functions that have been demonstrated, and we used the exponential variogram in our estimation. The Variational Bayesian method can be used in estimating variogram parameters; details are described in **Appendix**. Since the spatial covariance is assumed to be the same across time, we can use pooling information across time series to get more accurate variogram estimation.

Then we can estimate the covariance of the estimated coefficients for t-test.

$$\underset{v\in w}{\mathrm{Cov}}\left(\widehat{\boldsymbol{\beta}}_w\right) \equiv \Sigma_\beta = (X^\top X)^{-1} \otimes \underset{v\in w}{\widehat{\mathrm{Cov}}}(\boldsymbol{y}_w) \tag{5.17}$$

The t-value can be calculated as

$$t = c^\top \widehat{\boldsymbol{\beta}}_w / c^\top \sqrt{\mathrm{Cov}\left(\widehat{\boldsymbol{\beta}}_w\right) c} \tag{5.18}$$

where c is a vector indicates the tested regressor for the target voxel in the window, $\widehat{\boldsymbol{\beta}}_w$ is estimated for each voxel separately after the temporal whitening. We called this method winCov.

Another method considers combing the statistics within the neighbor window for each voxel. For functional connectivity analysis, instead of testing the estimated connectivity for each voxel, we can test the mean conectivity in the voxel's neighbor window. Then the model becomes:

$$\boldsymbol{y}_w(t) = \boldsymbol{X}_{ws}(t)(K\mu_{ws} + \boldsymbol{b}_{ws}) + \boldsymbol{X}_{wp}(t)\boldsymbol{\beta}_{wc} + \boldsymbol{e}_w(t) + \boldsymbol{\epsilon}_w(t) \tag{5.19}$$

where K is a vector with all elements equal 1, μ_w is a scalar. $\boldsymbol{X}_{ws}(t)$ is the seed time course regressor $\boldsymbol{X}_{ws}(t) = x_s(t)\mathbb{I}_{V_w}$, and $\boldsymbol{X}_{wp}(t)$ are other regressors. $\boldsymbol{b}_{ws}$ is used to model the difference across voxels within the window following a Gaussian distribution $\boldsymbol{b}_{ws} \sim \mathcal{N}\left(0, \sigma_b^2 \mathbb{I}_{V_w}\right)$.

Considering the random effects in the coefficients, variance of $\boldsymbol{y}_w(t)$ becomes

$$\underset{v\in w}{\widehat{\mathrm{Cov}}}\left(\boldsymbol{y}_w(t)\right) = \boldsymbol{X}_{ws}(t)\sigma_b^2 \mathbb{I}_{V_w} \boldsymbol{X}_{ws}^\top(t) + \hat{\Sigma}_e + \mathrm{diag}\left(\hat{\sigma}_{\epsilon_v}^2\right) \tag{5.20}$$

The covariance of the mean effects is:

$$\underset{v\in w}{\mathrm{Cov}}(\hat{\mu}_{ws}) = \left[\sum_{t=1}^{N} \boldsymbol{X}_w^\top(t)\boldsymbol{X}_w(t)\right]^{-1} \left[\sum_{t=1}^{N} \boldsymbol{X}_w^\top(t) \underset{v\in w}{\widehat{\mathrm{Cov}}}\left(\boldsymbol{y}_w(t)\right) \boldsymbol{X}_w(t)\right] \left[\sum_{t=1}^{N} \boldsymbol{X}_w^\top(t)\boldsymbol{X}_w(t)\right]^{-1} \tag{5.21}$$

After simplification, we have

$$\underset{v\in w}{\mathrm{Cov}}(\hat{\mu}_{ws}) = (X^{\top}X)^{-1} \otimes \left(\hat{\Sigma}_e + \mathrm{diag}\left(\hat{\sigma}^2_{\epsilon_v}\right)\right) + \left((X^{\top}X)^{-1}\left[\sum_{t=1}^{N} x_s^2(t)\, X^{\top}(t)X(t)\right](X^{\top}X)^{-1}\right) \otimes \sigma_b^2 \mathbb{I}_{V_w} \tag{5.22}$$

Using equation (5.22), we can estimate the combined coefficients in the voxel's neighbor window for each voxel and its covariance. The method is called winBeta in the following experiments.

Methods and Results

Simulation Experiments

Since it is impractical to estimate a covariance matrix of all voxels within brain, we performed the simulation on one slice. To create a simulated image, we used one scan of an empirical fMRI study as the constant image across time. An ROI time course calculated in the empirical data was used as the seed time course in the simulation, all voxels within the thalamus proper region are simulated to be connected to the seed time course while other voxels are not connected. The connected coefficient was set to be 0.8 and no confounds were simulated. The simulated images have 197 scans with 64×64 voxels in each scan. The spatial correlations were simulated using the exponential variogram function if the distance between two voxels within the 3×3 window size and equaled to 0 otherwise. The temporal correlation was modeled by an autoregressive model (AR(1)) with the model coefficient of 0.5. The temporal SNR was simulated around 50. The truth setting overlaid with one simulated slice is shown in **Figure 5.6**.

We performed 50 Monte Carlo simulations using the same setting. The connectivity map was estimated by regressing the seed time course on every other voxels within the brain mask using SPM8 (University College London, UK), winBeta and winCov. The representing results from one Monte Carlo simulation were shown in **Figure 5.6** on the significant t-map under uncorrected p-value threshold at $p < 0.001$ with one simulated image. The type I error and the type II error were calculated under uncorrected p-value threshold at 0.001 and 0.05, which are displayed in **Figure 5.7**. The winCov method used the

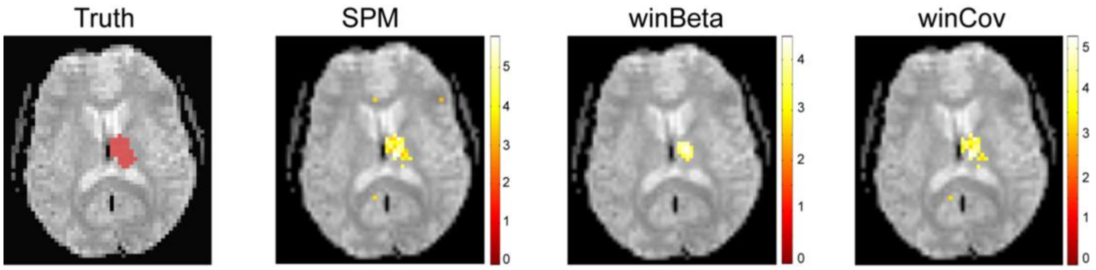

Figure 5.6 Simulation truth and representing results. The image labeled "Truth" is a simulated scan with the red region indicates positive connectivity to the seed time course. Other regions are not connected to the seed time series. Other images show the significant t-maps under uncorrected p-value threshold at $p < 0.001$ from SPM, winBeta, and winCov estimation.

same connected coefficient estimation as SPM while the winBeta method not. We compared the root mean square error (RMSE) of the estimated seed coefficients in **Figure 5.7**.

From the simulation results, we can see that if the spatial correlations exist in the data, the traditional estimation model cannot control the type I error because of ignoring the positive correlations. The mean type I error of SPM results across 50 Monte Carlo simulation is larger than 0.001 when the p-

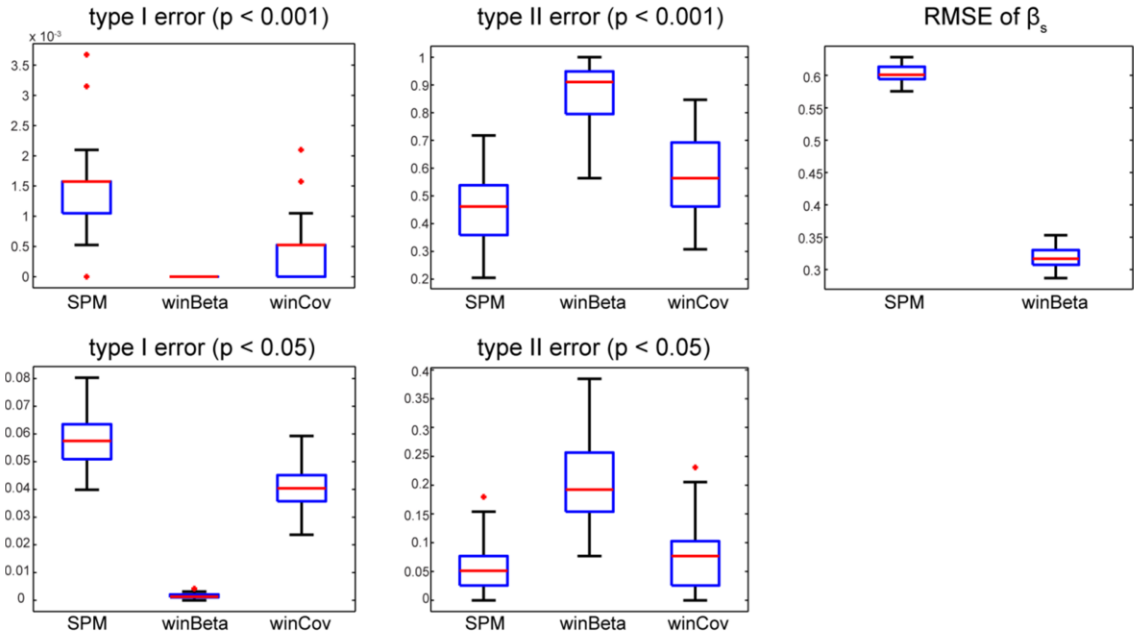

Figure 5.7 Quantitative simulation results. The left column shows the type I error across Monte Carlo simulations under uncorrected p-value threshold at $p < 0.001$ and $p < 0.05$. The middle column shows the typ II error across Monte Carlo simulations under uncorrected p-value threshold at $p < 0.001$ and $p < 0.05$. The right image shows the RMSE of the estimated seed connectivity coefficient from SPM and winBeta estimation.

value threshold is set to be 0.001 and it is larger than 0.05 when the p-value threshold is set to be 0.05. The type I error of the winBeta and winCov results are all under control. The type I error of the winBeta results are very small while the type II error are very large. This may because the estimated coefficients within the neighbor window are not similar enough to provide a significant test. But if we look at the value of the estimated coefficients, the winBeta method provides a better estimation than other two methods.

Empirical Experiments

We illustrated our proposed spatio-temporal model with one empirical 7T subject. This subject was from a 7T study described in (Newton, Rogers et al. 2012). The subject was instructed to both close their eyes and rest. Briefly, the resting state images were acquired for 500s using single shot gradient echo EPI (500 volumes, FOV = 192mm, flip $\theta = 53.8°$, TR/TE = 1000/28ms, SENSE factor = 3.92, full k-space acquisition, resolution 2x2x2mm, 96x96x13 voxels). Prior to analysis, all images were corrected for slice timing artifacts and motion artifacts using SPM8 (University College London, UK). All voxels' time courses were low pass filtered at 0.1Hz using a Chebychev Type II filter, linearly detrended, and de-meaned. The 7T data are not smoothed because the spatial SNR are much higher in 7T than 3T, and we are only interested in single subject results that smoothness is not necessary. The seed voxel was defined as a single manually selected voxel located in right primary motor cortex along the central sulcus that was also significantly activated by a conventional finger tapping task contrasting bimanual, self-paced finger tapping against a resting condition (FWE corrected, $p < 0.05$, minimum cluster size = 1 voxel) (Newton, Rogers et al. 2012). The design matrix for the general linear model was defined as the seed voxel time course, the six estimated motion parameters and the intercept. Each voxel's BOLD time course underwent linear regression of the design matrix to create connectivity maps.

The right motor cortex connectivity map was estimated using SPM8, winBeta and winCov. The significance was tested under uncorrected p-value threshold at $p < 0.001$ and shown on one dimension of the glass brain in **Figure 5.8**.

The left and right primary motor cortex and the premotor cortex show significance in the results, which is consistent with the motor network shown in (Newton, Rogers et al. 2012). However, the result from the SPM estimation is very noisy that a lot of voxels outside the motor network show significance. The numbers of the false positive voxels are much less in the winBeta and winCov results. The winBeta result is much conservative but still gets clear significant voxels within the motor network regions.

Discussion

The proposed ROI-level analysis enables inference of brain activity associations taking into account voxel- and ROI-level dependence structure in rs-fMRI data, while typical ROI analyses narrow the problem to focus on the average time series, which ignores within- and between-ROI correlations. ROI analyses are easier to interpret since the significant regions can be located in the anatomy structure but averaging the voxel intensities ignores some voxelwise specificity. The proposed spatio-spectral model overlaps voxel-based and ROI-based analyses so that inference is tested on the ROI-based level while the voxelwise effects are incorporated through the random effects.

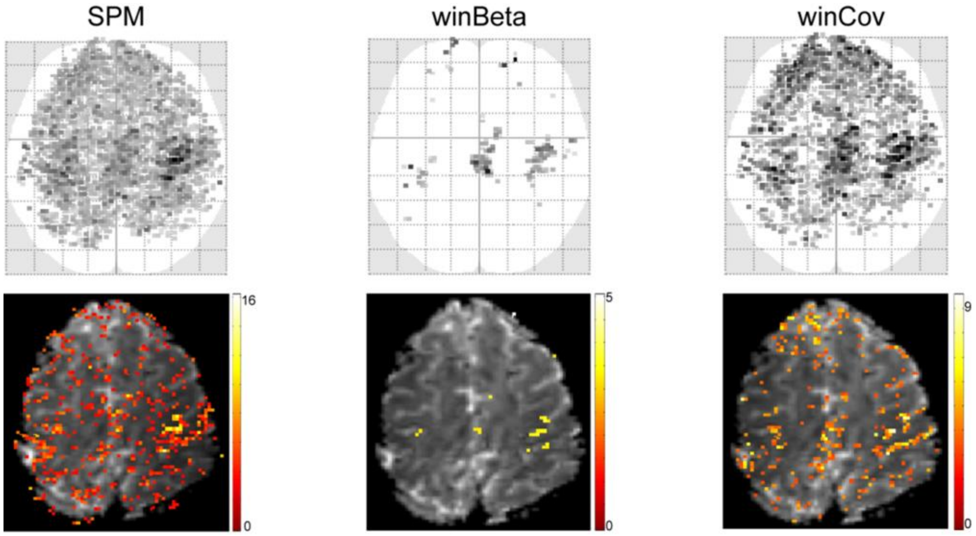

Figure 5.8 Empirical results. The top row shows the significant results under uncorrected p-value threshold at $p < 0.001$ in one dimension of the glass brain from SPM, winBeta, and winCov estimation. The bottom row displays one slice of the estimated t-map overlaid with one fMRI scan.

The proposed ROI-based spatio-spectral model is a sophisticated linear regression model that accounts for both spatial and temporal correlations. Spatial correlations are considered as voxel-specific random effects with within and between ROI correlations. The advantages of the spatio-spectral mixed-effects model compared with traditional ROI-base analysis have been demonstrated through task fMRI analysis on a small number of ROIs (Kang, Ombao et al. 2012). We extended this model to the resting state fMRI analysis on the whole brain. The primary theoretical contributions are that (1) the covariance of the estimated coefficients can be simplified to enable whole-brain analysis, (2) estimation of the temporal covariance can be simplified in the frequency domain, and (3) structural information on $\widehat{\Sigma_d}$ can be used to improve estimation. Together, these contributions enable efficient and practical whole brain spatio-spectral inference. Although the proposed framework is based on different theoretical underpinnings, the mixed effect general linear models of scientific interest may be used interchangeably with traditional massively univariate statistical parametric mapping.

Our model to incorporate component prior information regarding between-ROI functional dependence deserves further research in order to utilize structural information in multi-modal MRI, e.g., diffusion tensor images and rs-fMRI. However, it requires caveat to use this component-based approach because non-reliable or incorrect prior information can severely distort the results, even though this can be considered as one of a few non-Bayesian approaches to directly combine functional and structural connectivity information.

The two proposed voxel-wise spatio-temporal models are extensions of the idea within the spatio-spectral model to voxel-wise analysis. Without any pre-defined region of interest, we used a sliding window and considered the spatial correlations within the window. This makes the computation of the spatial covariance possible noting that calculating the spatial covariance of all voxels within the brain is impractical. The simulation results show that the traditional voxel-wise statistical inference implemented in SPM lose the control of type I error when spatial correlations exist. Our two voxel-wise spatio-temporal models winBeta and winCov can control the type I error by accounting the spatial correlations. The winCov results are similar to traditional methods with lower type I error and higher type II error. The winBeta method seems too conservative resulting in very low type I error but high type II error. In the empirical study, we did not achieve reasonable results due to low CNR. However, there are many random significant voxels outside our expected region in the SPM results while less in the winCov results and nearly no false positive voxels in the winBeta results. Therefore, with the consideration of spatial correlations, our proposed spatio-temporal model can better control the type I error and provide better estimations than traditional first level analysis model.

Appendix: Spatial Covariance Estimation with Exponential Variogram Function

For each window

$$\boldsymbol{y} = X\beta + \boldsymbol{b}, \boldsymbol{b} \sim N(0, V)$$

X is a vector whose elements are all one with length equals the number of voxels inside this window.

$$V = \hat{\Sigma}_e + \operatorname{diag}\left(\hat{\sigma}^2_{\epsilon_v}\right)$$

where $\sigma^2_{\epsilon_v}$ has been estimated

Assume variogram for Σ_e, $r(h) = \begin{cases} \tau^2 + \sigma^2\left(1 - exp(-\phi h)\right), h > 0 \\ 0, h = 0 \end{cases}$

$$V_{i,j} = \begin{cases} \sigma^2 exp\left(-\phi h_{i,j}\right), h_{i,j} > 0 \\ \tau^2 + \sigma^2 + \sigma^2_{\epsilon_v}, h_{i,j} = 0 \end{cases}$$

$$V = \tau^2 \mathbb{I} + \operatorname{diag}\left(\hat{\sigma}^2_{\epsilon_v}\right) + \sigma^2 exp(-\phi D)$$

where D is distance matrix

The negative free energy function is

$$F(\beta, \lambda) = \int q(\beta) \ln p(\beta, \boldsymbol{y}|\lambda)\, d\beta - \int q(\beta) \ln q(\beta)\, d\beta$$

with $\lambda = [\tau \quad \sigma \quad \phi]$

Define $\mu_{\beta|y} = \mathrm{E}\left(\hat{\beta}\right); \Sigma_{\beta|y} = \mathrm{Cov}\left(\hat{\beta}\right); \boldsymbol{r} = \boldsymbol{y} - X\mu_{\beta|y}$

$$F = \frac{1}{2}\ln|V^{-1}| - \frac{1}{2}\boldsymbol{r}^\top V^{-1}\boldsymbol{r} - \frac{1}{2}\operatorname{tr}\left\{\Sigma_{\beta|y} X^\top V^{-1} X\right\} + \frac{1}{2}\ln\left|\Sigma_{\beta|y}\right| + const$$

The parameter λ can be estimated using a gradient decent method. The estimated λ can be updated until converge according to

$$\Delta\lambda = H^{-1}g$$

where $g_i = \frac{\partial F}{\partial \lambda_i}$, and $H_{i,j} = \mathrm{E}\left\{-\frac{\partial^2 F}{\partial \lambda_i \partial \lambda_j}\right\}$.

$$\frac{\partial F}{\partial V^{-1}} = \frac{1}{2}V - \frac{1}{2}\boldsymbol{r}\boldsymbol{r}^\top - \frac{1}{2}X\Sigma_{\beta|y}X^\top$$

Define $P = V^{-1} - V^{-1}X(X^\top V^{-1}X)^{-1}X^\top V^{-1}$, then $PVP = P$

$$\frac{\partial P}{\partial \lambda_i} = -P\frac{\partial V}{\partial \lambda_i}P$$

$$g_i = \frac{\partial F}{\partial \lambda_i} = \mathrm{tr}\left\{-\frac{\partial F}{\partial V^{-1}}V^{-1}\frac{\partial V}{\partial \lambda_i}V^{-1}\right\} = -\frac{1}{2}\mathrm{tr}\left\{P\frac{\partial V}{\partial \lambda_i}\right\} + \frac{1}{2}\boldsymbol{y}^\top P\frac{\partial V}{\partial \lambda_i}P\boldsymbol{y}$$

Note that $\mathrm{E}\{\boldsymbol{y}\boldsymbol{y}^\top\} = V$, we can calculate

$$H_{i,j} = \mathrm{E}\left\{-\frac{\partial^2 F}{\partial \lambda_i \partial \lambda_j}\right\} = \frac{1}{2}\mathrm{tr}\left\{P\frac{\partial V}{\partial \lambda_i}P\frac{\partial V}{\partial \lambda_j}\right\}$$

Using $\frac{\partial V}{\partial \tau} = 2\tau\mathbb{I}$, $\frac{\partial V}{\partial \sigma} = 2\sigma exp(-\phi D)$, and $\frac{\partial V}{\partial \phi} = \sigma^2\big(exp(-\phi D).\times(-D)\big)$, where $.\times$ denotes multiple the corresponding elements in two matrix. Then we have

$$g_1 = \frac{\partial F}{\partial \tau} = -\mathrm{tr}\{\tau P\} + \tau\boldsymbol{y}^\top P^T P\boldsymbol{y}$$

$$g_2 = \frac{\partial F}{\partial \sigma} = -\mathrm{tr}\{\sigma P exp(-\phi D)\} + \sigma\boldsymbol{y}^\top P^\top exp(-\phi D)P\boldsymbol{y}$$

$$g_3 = \frac{\partial F}{\partial \phi} = -\frac{1}{2}\mathrm{tr}\big\{P\sigma^2\big(exp(-\phi D).\times(-D)\big)\big\} + \frac{1}{2}\boldsymbol{y}^\top P^\top \sigma^2\big(exp(-\phi D).\times(-D)\big)P\boldsymbol{y}$$

$$H_{11} = \mathrm{E}\left\{-\frac{\partial^2 F}{\partial \tau^2}\right\} = 2\tau^2\mathrm{tr}\{PP\}$$

$$H_{12} = \mathrm{E}\left\{-\frac{\partial^2 F}{\partial \tau \partial \sigma}\right\} = 2\tau\sigma\mathrm{tr}\{PP exp(-\phi D)\} = H_{21}$$

$$H_{22} = \mathrm{E}\left\{-\frac{\partial^2 F}{\partial \sigma^2}\right\} = 2\sigma^2\mathrm{tr}\{P exp(-\phi D)P exp(-\phi D)\}$$

$$H_{13} = \mathrm{E}\left\{-\frac{\partial^2 F}{\partial\tau\partial\phi}\right\} = \tau\sigma^2 \mathrm{tr}\left\{PP\left(exp(-\phi D).\times(-D)\right)\right\} = H_{31}$$

$$H_{23} = \mathrm{E}\left\{-\frac{\partial^2 F}{\partial\sigma\partial\phi}\right\} = \sigma^3 \mathrm{tr}\left\{Pexp(-\phi D)P\left(exp(-\phi D).\times(-D)\right)\right\} = H_{32}$$

$$H_{33} = \mathrm{E}\left\{-\frac{\partial^2 F}{\partial\phi^2}\right\} = \frac{1}{2}\sigma^4 \mathrm{tr}\left\{P\left(exp(-\phi D).\times(-D)\right)P\left(exp(-\phi D).\times(-D)\right)\right\}$$

Note that since we assume the spatial covariance stay the same across time, the y here can be pooled across time series.

CHAPTER VI

ASSESSMENT OF INTER MODALITY MULTI-SITE INFERENCE WITH THE 1000 FUNCTIONAL CONNECTOMES PROJECT

Introduction

The relationship between structure and biological function exists in the human brain from the macroscopic scale to the microscopic scale (Honey, Thivierge et al. 2010). This relationship, when discovered and quantified, may provoke powerful informers for early disease detection, prevention, and our overall understanding of the brain. Not surprisingly, researchers have already demonstrated many important micro- and macroscopic structure-function correlations in the brain including neuronal structure and dynamics (Rubinov, Sporns et al. 2009), the structure of the auditory cortex and its Fourier transform properties (Zatorre, Belin et al. 2002), and brain structure and mental illness (Kaufman and Charney 2001; Antonova, Sharma et al. 2004).

The structure-function relationship can be analyzed using structural magnetic resonance image (MRI) and functional MRI (fMRI). The analysis of fMRI has been widely conducted to infer spatial-temporal characteristics of brain activity. In addition to task or event based models, many fMRI studies are now focused on the analysis of resting state activity (van den Heuvel and Hulshoff Pol 2010). When the brain is at rest (i.e., not task driven), functional networks produce temporal correlated low frequency patterns of activity that can be observed with resting state fMRI (rs-fMRI) (Bandettini, Jesmanowicz et al. 1993; Biswal, Yetkin et al. 1995). These correlations imply that the functional brain networks can be studied using rs-fMRI and voxel-wise regression with no prior hypothesis (Friston, Holmes et al. 1994). Besides, rs-fMRI is more sensitive resources to explore the reorganization of functional brain networks related to age or sex rather than comparing differences in task activity (Meier, Desphande et al. 2012).

Recently, various brain imaging studies have been conducted in institutes over the world. With these structural and functional brain MRI studies, a data sharing strategy is badly needed. The idea of sharing data was proposed over a decade ago with objective of enabling investigators to confirm and extend the findings of published studies and facilitating discovery science approaches (Van Horn, Grethe et al. 2001; Van Horn and Gazzaniga 2002; Van Horn, Grafton et al. 2004). Accordingly, the 1000 Functional Connectomes Project was formed in 2009 to aggregate existing rs-fMRI data from collaborating centers throughout the world (http://www.nitrc.org/projects/fcon_1000/). An initial demonstration of the feasibility of data pooling and data exploration across centers with the aggregate rs-fMRI dataset has been published in (Biswal, Mennes et al. 2010). To date, there are over 30 institutes involved in this study and over 1000 subjects are scanned. The project has proven successful towards sharing multi-scale data (Mennes, Biswal et al. 2012). With this database, researchers have discovered complex functional brain networks and the covariates related reorganizations in the human brain (Rubinov and Sporns 2011; Tomasi and Volkow 2011; Meier, Desphande et al. 2012).

Combining brain image projects together is a powerful idea that provides “big data” sets across large population and multi-modality brain images. The variance in functional connectivity across individuals and studies has been studied and characterized (Yan, Craddock et al. 2013). However, how to combine large scale studies from various sites in a reasonable way is still a challenging problem. Mega-analysis and meta-analysis are two powerful methods in analyzing multi-site studies (Jahanshad, Kochunov et al. 2013). Mega-analysis is a fixed-effects analysis that allows pooling the raw information from individual subject to increase statistical power while maintaining consistent quality control (Serretti, Cusin et al. 2006; Ripke, Wray et al. 2013). The meta-analysis can be used as a random-effects model that accounts both the between-site and within-site variability (Etkin and Wager 2007; Seifuddin, Mahon et al. 2012). Herein, we characterized mega- and meta-analysis methods with structure function relationships inference on the 1000 functional connectomes data.

Theory

Mega-Analysis

Mega-analysis jointly analyzes all studies by combining all data together and fits a single model. This method is a fixed effect model that can fit a model on all data on hand ignoring the between site variability. It can be described in a general linear model (GLM) treating the factor sites as other regressors:

$$\boldsymbol{y} = \beta_{mean} + \boldsymbol{x}_{site1}\beta_{site1} + \boldsymbol{x}_{site2}\beta_{site2} + \cdots + \boldsymbol{X}_r\boldsymbol{\beta}_r + \boldsymbol{\epsilon} \tag{6.1}$$

In this GLM, the first column of the design matrix is the overall intercept, the x_{sitei} are the site factors for site i, and the $\boldsymbol{X}_r$ are other regressors.

The existence of the site difference can be tested using F-test. The null hypothesis is:

$$\text{H0}: \beta_{site1} = \beta_{site2} = \cdots$$

which equals to

$$\text{H0}: c^{\top}\boldsymbol{\beta} = \boldsymbol{0}, with\ c = \begin{bmatrix} 0 & 1 & -1 & 0 & \cdots & 0 \\ 0 & 0 & 1 & -1 & \ddots & \vdots \\ \vdots & \vdots & \ddots & \ddots & \ddots & 0 \\ 0 & 0 & \cdots & 0 & 1 & -1 \end{bmatrix} \tag{6.2}$$

With this equation we can generate a reduced model assuming the null hypothesis is true, and the F-statistics can be calculated from the reduced model and the full model.

The significant effects of each covariate can be tested using t-tests.

Meta-Analysis

Meta-analysis can be used to summarize the coefficients from individual site studies (van Houwelingen, Arends et al. 2002; Becker and Wu 2007). There are fixed effects model and mixed effects model in meta-analysis ignoring or accounting the site variability respectively (Konstantopoulos 2006). Here, we focus on the mixed effects model in meta-analysis. Considering each site study to be an independent random sample from a normal population, we have

$$
\begin{gathered}
\hat{\beta}_{pi} \sim N(\beta_{pi}, v_{pi}) \\
\beta_{pi} \sim N(\beta_p, \sigma_p^2)
\end{gathered}
\tag{6.3}
$$

where β_{pi} is the coefficient for regressor p in site i, $\hat{\beta}_{pi}$ is an estimation of β_{pi}, β_p is the mean coefficient for regressor p of the population. v_{pi} is the within-site variance and σ_p^2 represents the between-site variance.

To test the existence of the site difference on each covariate, the null hypothesis is:

$$H0: \beta_{p1} = \beta_{p2} = \cdots$$

which equals to test the significance of the between-site variance $\sigma_p^2 = 0$. It can be tested using chi-square test (Hedges and Pigott 2004; Konstantopoulos 2006).

$$
\begin{gathered}
Q_p = \sum\nolimits_i \left(\hat{\beta}_{pi} - \hat{\beta}_p\right)^2 / \hat{v}_{pi} \\
\hat{\beta}_p = \frac{\sum_i w_{pi} \hat{\beta}_{pi}}{\sum_i w_{pi}}
\end{gathered}
\tag{6.4}
$$

where $w_{pi} = 1/\hat{v}_{pi}$. Under the null hypothesis, Q_p follows chi-square distribution with K-1 degrees of freedom (K is the number of sites).

The significance of the covariate effects can be tested using t-test. In the mixed effects model, the generalized coefficients are:

$$
\begin{gathered}
\hat{\beta}_p^* = \frac{\sum_i w_{pi}^* \hat{\beta}_{pi}}{\sum_i w_{pi}^*} \\
w_{pi}^* = \frac{1}{\hat{s}_{pi}^2 + \hat{\sigma}_p{}^2}
\end{gathered}
\tag{6.5}
$$

where $\hat{\beta}_p^*$ is an estimation of $\hat{\beta}_p$ accounting the within-site and between-site variability. The between site variance can be estimated as:

$$
\hat{\sigma}_p = \begin{bmatrix} \dfrac{Q-(k-1)}{a} & if\ Q \geq (k-1) \\ 0 & if\ Q < (k-1) \end{bmatrix}, \ a = \sum\nolimits_i w_{pi} - \frac{\sum_i w_{pi}^2}{\sum_i w_{pi}}
\tag{6.6}
$$

The variance of this estimation is:

$$\mathrm{var}(\hat{\beta}_p^*) = \left(\sum\nolimits_i w_{pi}^*\right)^{-1} \tag{6.7}$$

With the mean and variance estimation, we can test the significance of the coefficient by calculating its t-value. The theory of mega-analysis and meta-analysis are illustrated in **Figure 6.1**.

An alternatively way of combining statistics is to fit a second level analysis and estimate the mean effect. However, this approach assumes the variance of the estimated covariates for every site are the same, i.e., v_{pi} are the same for each i. This assumption can hold true for a group study, where every subject are scanned using the same scanner and the same parameters, but it is not reasonable for different site studies. The property of accounting both the between-site variance and different within-site variance makes meta-analysis a very important statistical method in multi-site studies.

Data Quality Assessment

Before statistical analysis, the MRI data must go through pre-processing steps, at least including

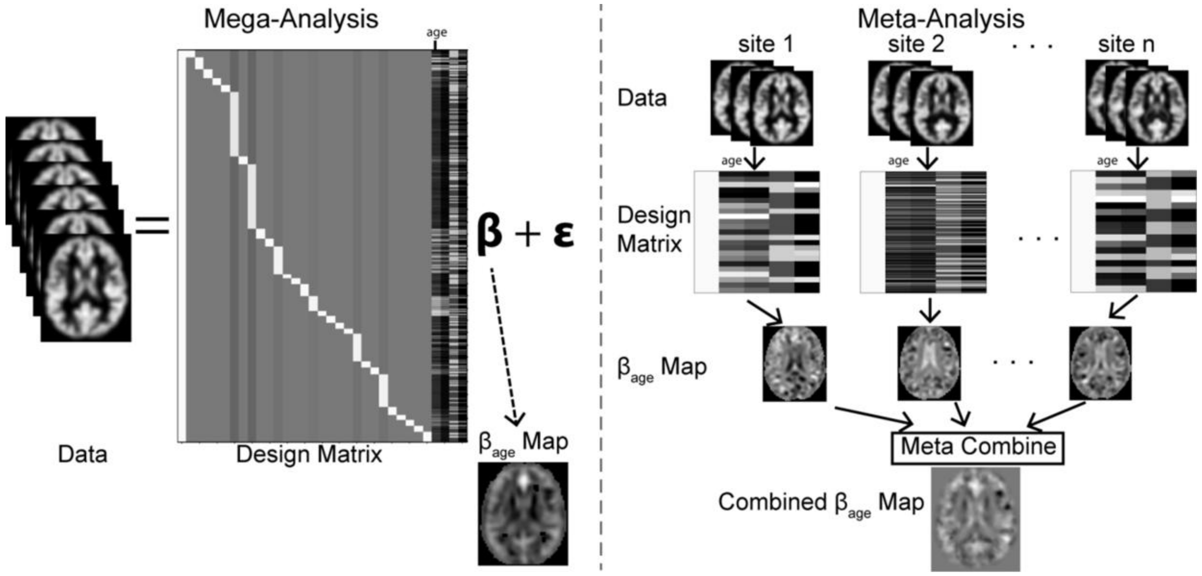

Figure 6.1 Model of mega-analysis and meta-analysis. The left side shows the general linear model for the mega-analysis. The covariates are estimated from regression estimation. The right side shows the framework for meta-analysis. The covariates are estimated for each site, then they are combined to calculate a final estimation.

registration to the same place in the same coordinate system. Since this is a very large scale study, it is possible that the registration methods failed on some data. Principle component analysis (PCA) may be used for semi-automatic data quality assessment. Assuming the large variances across an image represent signals and small variances correspond to noise, PCA can be used for pattern recognition (Turk and Pentland 1991), manifold learning (Gerber, Tasdizen et al. 2010), and noise reduction (Thomas, Harshman et al. 2002). It is impossible to view all images together with thousands of voxels in each image in a large scale study; therefore, we used PCA for dimensionality reduction and explored the mapped data to find out possible outliers. Specifically, in order to assess the data quality after pre-processing, we performed PCA on all pre-processed images, and displayed the projection of the data in two dimensions.

Methods and Results

Data Quality

Within the 1000 Functional Connectome Project, studies conducted in the same center may be different using different imaging parameters. We considered the images acquired under the same parameters in the same center as one site study. All the data we used here are from normal "healthy" people, and we only analyzed the data where the age and sex information are available and the resting state fMRI are acquired for the whole brain. These data information are listed in **Table 6.1**.

The structural brain MRI images were studied through voxel-based morphometry (Ashburner and Friston 2000) analyzing the local concentration of gray matter changes. The structural images were skull stripped by the releasing center. Prior to statistical analysis, the skull stripped structure images were segmented, normalized to MNI-space, and smoothed (8mm Gaussian kernel) using VBM8 (University of Jena, Department of Psychiatry, Germany) and SPM8 (University College London, UK). After these pre-processing steps, we got the gray matter (GM) density maps for each subject, which were used for statistical analysis.

To assess the quality of the normalized GM maps, we performed PCA on the middle axial slice and on the whole brain within the brain mask for all subjects. When doing PCA on the middle slice, the voxels outside the brain mask are not excluded, because we need to account the shape of the registered brain. On the whole brain data assessment, we applied a template brain mask in the MNI-space from SPM8 and performed PCA on the voxels within the brain mask. We used a template brain mask is

Table 6.1. Data from 1000 Functional Connectome Project

ID	Center	PI	N	Parameters
1	Ann Arbor	Monk, C.S./ Seidler, R.D./ Peltier, S.J.	25	22M/3F, ages: 13-40, TR=2, slices=40, timepoints=295
2	Atlanta	Mayberg, H.S.	28	13M/15F, ages: 22-57, TR=2, slices=20, timepoints=205
3	Baltimore	Pekar, J.J./ Mostofsky, S.H.	23	8M/15F, ages: 20-40, TR=2.5, slices=47, timepoints=124
4	Bangor	Colcombe, S.	20	20M/0F, ages: 19-38, TR=2, slices=34, timepoints=265
5	Beijing	Zang, Y.F.	198	76M/122F, ages: 18-26, TR=2, slices=33, timepoints=225
6	Berlin	Margulies, D.	26	13M/13F, ages: 23-44, TR=2.3, slices=34, timepoints=195
7	Cambridge	Buckner, R.L.	198	75M/123F, ages: 18-30, TR=3, slices=47, timepoints=119
8	Cleveland	Lowe, M.J.	31	11M/20F, ages: 24-60, TR=2.8, slices=31, timepoints=127
9	Dallas	Rypma, B.	24	12M/12F, ages: 20-71, TR=2, slices=36, timepoints=115
10	ICBM	Evans, A.C.	86	41M/45F, ages: 19-85, TR=2, slices=23, timepoints=128
11	Leiden	Rombouts, S.A.R.B.	12	12M/0F, ages: 20-27, TR=2.18, slices=38, timepoints=215
12	Leiden	Rombouts, S.A.R.B.	19	11M/8F, ages: 18-28, TR=2.2, slices=38, timepoints=215
13	Leipzig	Villringer, A.	37	16M/21F, ages: 20-42, TR=2.3, slices=34, timepoints=195
14	Milwaukee	Li, S.J.	46	15M/31F, ages: 44-65, TR=2, slices=64, timepoints=175
15	Munchen	Sorg, C./Riedl, V.	16	10M/6F, ages: 63-73, TR=3, slices=33, timepoints=72
16	Newark	Biswal, B.	19	9M/10F, ages: 21-39, TR=2, slices=32, timepoints=135
17	New Haven	Hampson, M	19	10M/9F, ages: 18-48, TR=1, slices=16, timepoints=249
18	New Haven	Hampson, M	16	8M/8F, ages: 18-42, TR=1.5, slices=22, timepoints=181
19	New York	Milham, M.P./ Castellanos,F.X.	84	43M/41F, ages: 7-49, TR=2, slices=39, timepoints=192
20	New York	Milham, M.P./ Castellanos,F.X.	20	8M/12F, ages: 18-46, TR=2, slices=33, timepoints=175
21	Orangeburg	Hoptman, M.	20	15M/5F, ages: 20-55, TR=2, slices=22, timepoints=165
22	Oulu	Kiviniemi, V.J./ Veijiola, J.	103	37M/66F, ages: 20-23, TR=1.8, slices=28, timepoints=245
23	Oxford	Smith, S.M./ Mackay, C.	22	12M/10F, ages: 20-35, TR=2, slices=34, timepoints=175
24	Palo Alto	Greicius, M.	17	2M/15F, ages: 22-46, TR=2, slices=29, timepoints=235
25	Pittsburgh	Siegle, G.	17	10M/7F, ages: 25-54, TR=1.5, slices=29, timepoints=275
26	Queensland	McMahon, K.	19	11M/8F, ages: 20-34, TR=2.1, slices=36, timepoints=190
27	Saint Louis	Schlaggar, B./ Petersen, S.	31	14M/17F, ages: 21-29, TR=2.5, slices=32, timepoints=127

because the whole brain image size is too large and we already assessed the brain shape on the middle slice. The ratios of the sum of the eigenvalues are plotted in **Figure 6.2**. To display the all images together, we plotted the projection of the data to the first two dimensions. One slice of corresponding GM map is shown on some selected subjects. Because we have a lot of observations and very high dimensions, the mapped data on the first two dimensions may not provide enough information. To incorporate the information of more eigenvectors, we viewed the reconstruction errors using these eigenvectors. Because over 50% percent variances can be represented in the first 20 eigenvectors, we explored the reconstruction errors using the first 10 eigenvectors. The choice of the number of eigenvectors is an art that needs further analysis, but it is not our focus here. Here we just chose an arbitrary number that not include eigenvectors corresponding small eigenvalues, which correspond to image noise, and showed how well the data can be reconstructed. The reconstruction errors are also

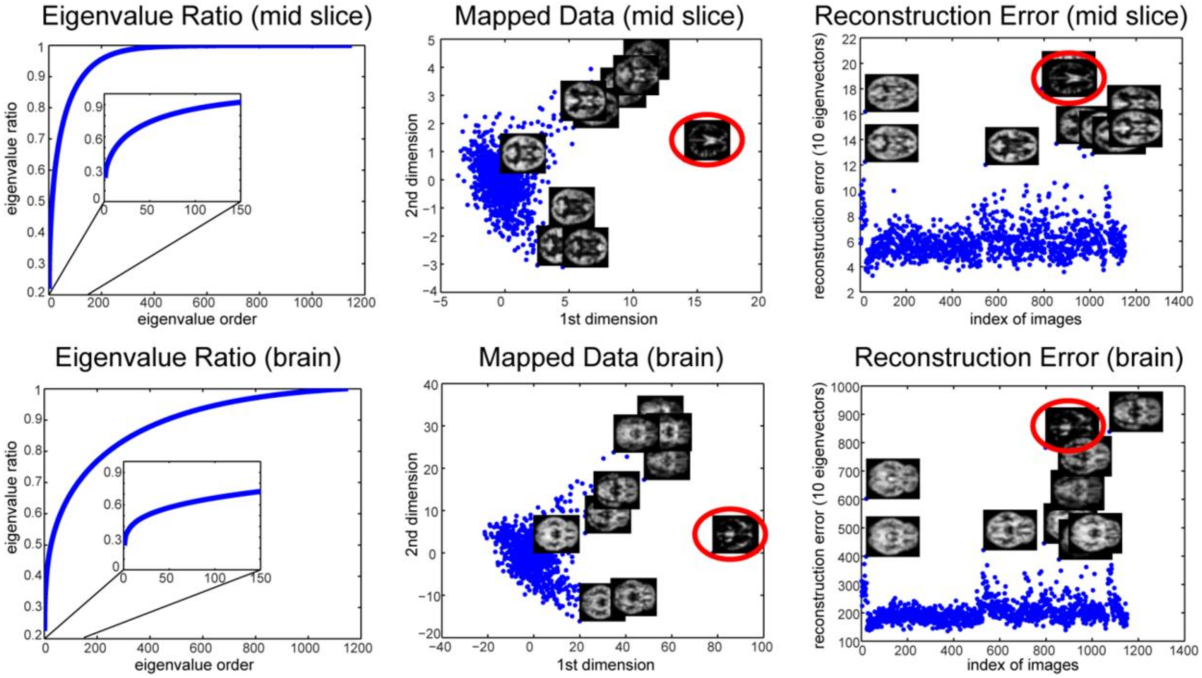

Figure 6.2 PCA results on smoothed Gray Matter density maps. The first row shows PCA results on the middle slice across all subjects without applying brain mask. The second row shows the PCA results on the whole brain within the template brain mask. The left column displays eigenvalue ratio, the middle column are mapped data on the first two dimensions, and the right column are the reconstruction errors using 10 eigenvectors. The red circle indicates some obvious outliers.

displayed in **Figure 6.2** with one slice of GM map on selected subjects.

For the rs-fMRI data, the first 5 time points of each time series were discarded when releasing. The remaining time series were pre-processed using SPM8. The pre-processing steps include temporal realignment, spatially normalized to MNI space, spatially smoothed with an 8 mm FWHM Gaussian kernel, and low pass filtered at 0.1 Hz using a Chebychev Type II filter. We did not do slice timing correction is because the slice order information are not available for every site study.

The pre-processed fMRI data are also underwent PCA analysis on the middle slice and the whole brain within the brain mask. The PCA analysis results are shown in **Figure 6.3**.

From these plots and the representing images of the PCA results, we can easily detect outliers as indicated in **Figure 6.2** and **Figure 6.3**. We explored subjects closed to these outliers and found that most

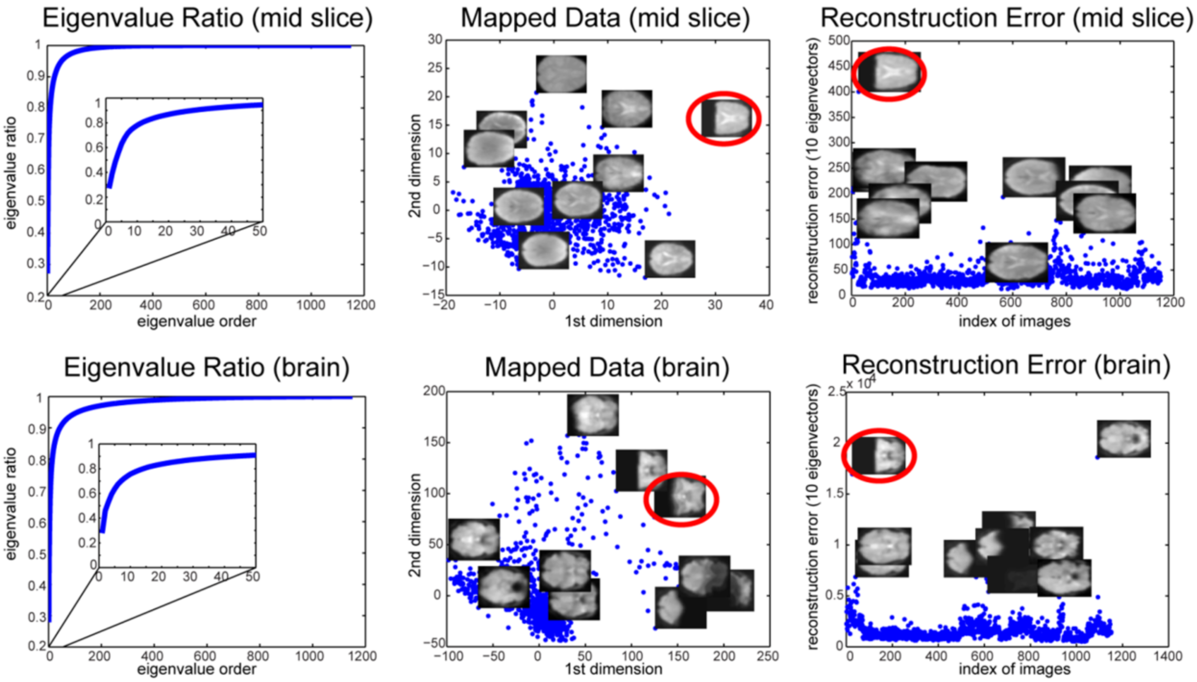

Figure 6.3 PCA results on pre-processed fMRI images. The first row shows PCA results on the middle slice across all subjects without applying brain mask. The second row shows the PCA results on the whole brain within the template brain mask. The left column displays eigenvalue ratio, the middle column are mapped data on the first two dimensions, and the right column are the reconstruction errors using 10 eigenvectors. The red circle indicates some obvious outliers.

fMRI data from site Atlanta and half data from ICBM are missing regions after normalization. So we excluded these data some other obvious outliers from other sites. After the data quality assessment, we used 1086 subjects from 26 sites in the following statistical analysis. Notice that we only applied a typical and simple pre-processing pipeline with algorithms implemented in SPM8 and VBM8. A better registration algorithm may provide better results that some bad observations here become acceptable. Improving data quality is not our focus here; instead, our aim is to show a method that can make the assessment of the data quality in a large scale study easier and demonstrate that we are able to do further statistical analysis with these acceptable data.

Multi-site Inference on Gray Matter

The significance of the site difference is explored in the gray matter density maps. The age and sex related changes have been proved in the gray matter (Chen, Sachdev et al. 2007; Wellington, Bilder et al. 2013). To account for their influence in the site effects analysis, we fitted a GLM on smoothed gray matter density maps adjusted for covariates of age, age^2, sex, and age×sex. The analyses are performed using SPM8 using an implicit mask.

The GLM for mega-analysis is:

$$y = \beta_{mean} + x_{site1}\beta_{site1} + x_{site2}\beta_{site2} + \cdots + x_{age}\beta_{age} + x_{age2}\beta_{age2} + x_{sex}\beta_{sex} + x_{as}\beta_{as} + \epsilon \tag{6.8}$$

The positive effects of the mean and every other covariate are tested using one-sided T-test, and the effect of the site difference is tested using F-test.

In meta-analysis, we applied a GLM model for each site then generalized the estimated statistics. The GLM for each site is:

$$y = \beta_{con} + x_{age}\beta_{age} + x_{age2}\beta_{age2} + x_{sex}\beta_{sex} + x_{as}\beta_{as} + \epsilon \tag{6.9}$$

From the data information we can see that there are two sites are unisex studies, so the sex and age×sex covariates are not in the two studies. When we combine the coefficients for sex and age×sex, we only have 24 sites while other statistics are combined using 26 sites. The effects of the combined statistics are tested using one sided T-test to explore the positive relationship. The effect of the site difference is tested using Chi-squared test.

The results of the mega-analysis and the meta-analysis are shown in **Figure 6.4** and **Figure 6.5**. **Figure 6.4** shows the significant positive mean effect and the significant site difference under the family wise error (FWE) correction threshold at $p < 0.05$. The FWE p-value threshold for each voxel is calculated based on the smoothness estimation of the full width at half maximum (FWHM). Although this parameter is different for each sited study in the meta-analysis, they are not very different. Since we used the same Gaussian kernel in the gray matter smoothness for every image, we used the mean value of the FWHM over all sites for the FWE correction in meta-analysis. The results of the significance can be viewed on a glass brain, which is the significance map projected into three dimensions. Here we showed one dimension of the glass brain with one slice of the significant t-map (t-value exceeds the significant threshold) overlaid with the corresponding smoothed GM slice. The positive effects of age and sex are

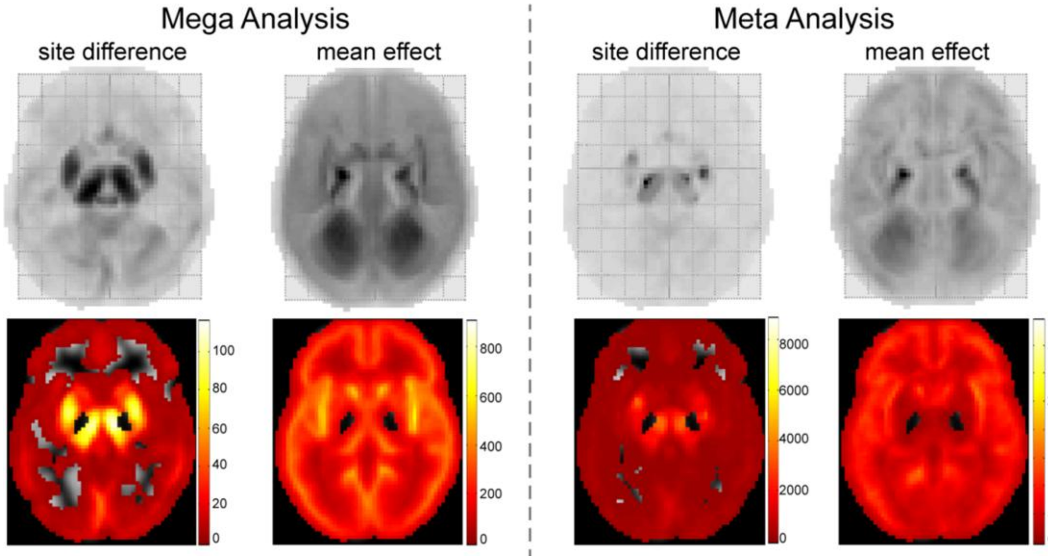

Figure 6.4 Mega- and Meta-analysis results of site difference and mean effect on smoothed GM maps. The top row displays the results in one dimension of a glass brain. The bottom row displays the t-value of the significant voxels overlaid with one slice GM map. The left two columns are results from mega-analysis and the right two columns are results from meta-analysis.

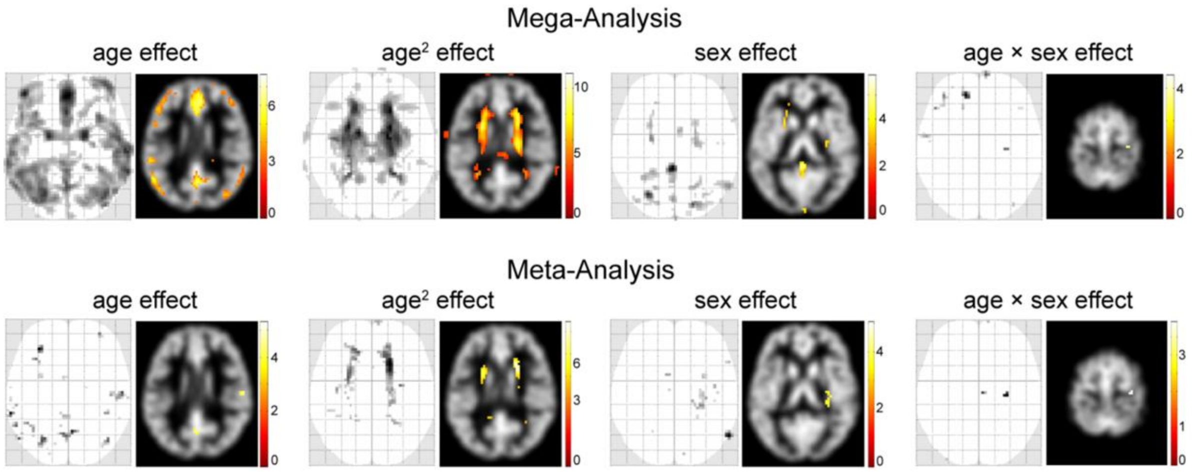

Figure 6.5 Mega-analysis and Meta-analysis results of age, age^2, sex, and age×sex effects on smoothed GM maps. The top row shows the results from mega-analysis and the bottom row displays the results from meta-analysis. For each covariate effect, one dimension of the glasss brain and one slice of the significant t-value map overlaid with the GM map are shown.

much less significant that few voxels show significance under the FWE corrected p-value threshold at 0.05. We showed the significant results for age, age^2, sex, and age×sex coefficients under uncorrected p-value threshold at $p < 0.001$.

The site difference and mean effect from mega-analysis and meta-analysis are similar and exist almost everywhere. The significant site difference region from meta-analysis seems a little larger than from mega-analysis, noting that the resulting brain mask from mega-analysis and meta-analysis are the same. The significant regions of age, age^2, sex, and age×sex effects from mega-analysis are larger than from meta-analysis. This may due to the fact that mega-analysis is a fixed effect analysis ignoring the between-site variance while meta-analysis is a mixed effect analysis accounting the between-site variability. Thus, the same estimated coefficient will have higher t-value from mega-analysis than from meta-analysis.

To explore the relationship of the mega- and meta-analysis, we analyzed the agreement of their statistical maps and significant maps. Their linear relationship is shown by regressing the statistical value from the meta-analysis on the statistical value from the mega-analysis. The correlations on the statistical maps and the Dice coefficients on the displayed significance maps (FWE $p < 0.05$ for site difference and mean effect, uncorrected $p < 0.001$ for other covariates) are calculated. The results are shown in **Figure 6.6**.

The relationship results show that the correlation of the mega- and meta-analysis on the site difference is very high. The correlations for other effects are much lower but all exceed 0.4, and in most cases the scale of the statistical value from mega-analysis are larger than the statistical value from meta-analysis. When it comes to the significance map, the Dice coefficients are high for all statistical tests. It reaches 1 for the positive mean effect test because the mean effects are significant everywhere within the brain mask under mega- or meta-analysis.

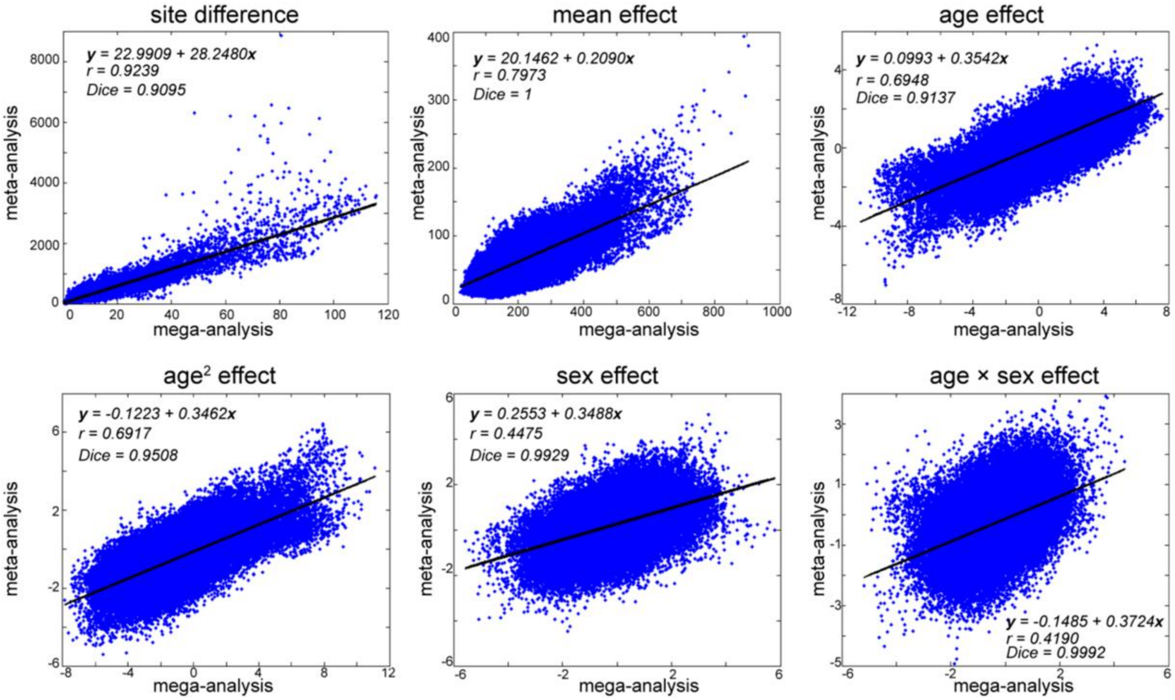

Figure 6.6 Relationship of the mega- and meta-analysis results on smoothed GM maps. The x-axis represents the statistical value from the mega-analysis (F-statistics for site difference, T-statistics for covariates). The y-axis represents the statistical value from the meta-analysis (Chi-squared statistics for site difference, T-statistics for covariates). The blue dots are voxels within the brain mask, and the black lines are linear regression line regressing the meta-analysis results on the mega-analysis results. The r value shown on the plots are the correlation value and the Dice represents the Dice coefficient of the significance maps.

Multi-site Inference on Functional Connectivity

The low frequency correlation of the blood flow under rest can be tested using a seed model with rs-fMRI. In the seed model functional connectivity analysis, a seed region is selected and its connectivity to the rest of the brain is analyzed. The selection of the seed region is different for different purpose and is based on the specific clinical questions. The hippocampus network has been proved to be related to memories in human and in animals (Neves, Cooke et al. 2008; Takashima, Nieuwenhuis et al. 2009) and the age effects were demonstrated in the shape analysis of hippocampus in normal people (Xu, Valentino et al. 2008). Here we studied the site effects on the hippocampus functional connectivity network accounting the covariates of age, age^2, sex, and age×sex using mega- and meta-analysis. The left hippocampus (LH) is selected as the seed region using the atlas in the WFUpickatlab toolbox (fmri.wfubmc.edu/software/PickAtlas). For each pre-processed fMRI, we calculated the average image intensity across all voxels in the LH to get the seed time series for the connectivity analysis. The six estimated motion parameters from realignment estimation were used as confounds. After the functional connectivity analysis we got a t-map of the LH functional connectivity for each subject.

We used the model described in equation (6.8) for mega-analysis and the model in equation (6.9) for each site studies in meta-analysis. The mean and other covariate effects were tested using one-sided T-test to explore the positive relationships and the site difference was tested using F-test and Chi-squared test for mega- and meta-analysis respectively. The results are shown in **Figure 6.7** and **Figure 6.8** on one dimension of the glass brain and one slice of the significant t-map overlaid with the corresponding smoothed gray matter image. **Figure 6.7** shows the significant mean effect and the site difference under the FWE correction threshold at $p < 0.05$. Since both the left and the right hippocampus are in the hippocampus network related to memories, we can expect the LH functional connectivity map is significant on the right hippocampus. The mean effect of the functional connectivity maps analysis is in fact a mean LH functional connectivity map acquired from a group analysis. From **Figure 6.7** we can see that the LH has the highest mean effect t-value for both mega- and meta-analysis, this is because we calculated the seed time course from this region. Besides the left hippocampus, the right hippocampus has

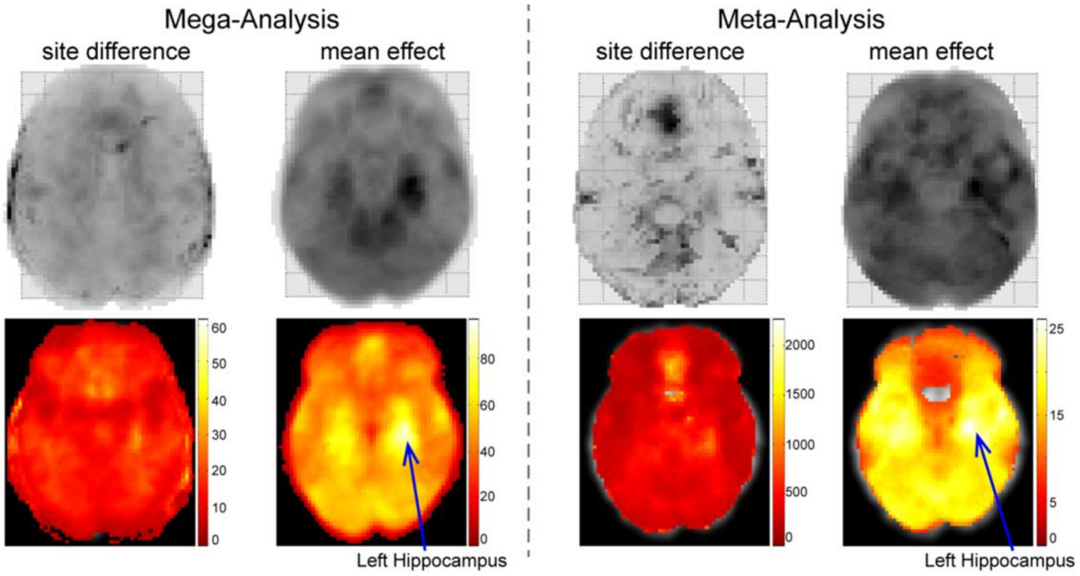

Figure 6.7 Mega- and Meta-analysis results of site difference and mean effect on LH functional connectivity maps. The top row displays the results in one dimension of a glass brain. The bottom row displays one slice of the significant t-value map overlaid with the GM map. The left two columns are results from mega-analysis and the right two columns are results from meta-analysis.

the highest mean effect t-value, which agrees with our expectation. The site difference seems existing everywhere, which agrees with the GM analysis.

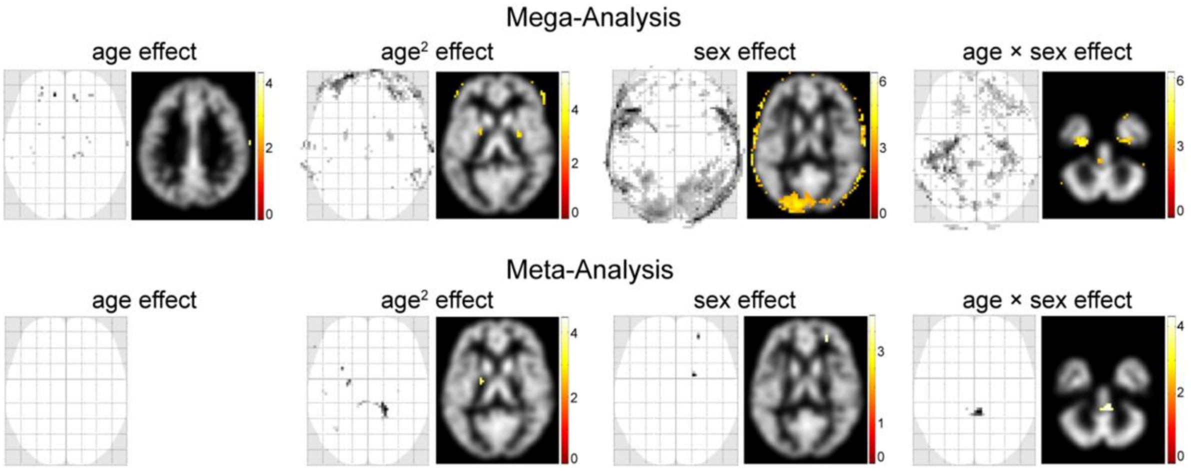

Figure 6.8 Mega- and Meta-analysis results of age, age^2, sex, and age×sex effects on LH functional connectivity maps. The top row shows the results from mega-analysis and the bottom row shows the results from meta-analysis. For each covariate effect, one dimension of the glasss brain and one slice of the significant t-value map overlaid with the GM map are shown. There is no significant age effect from meta-analysis and not shown here.

For age, age^2, sex, and age×sex effects, there are few voxels significant under FWE corrected threshold at $p < 0.05$ so we show the significant results under uncorrected p-value threshold at $p < 0.001$ in **Figure 6.8**. There is no significant age effect under the uncorrected $p < 0.001$ in meta-analysis and nothing was shown. For other covariates effect, the number of significant voxels from the meta-analysis is much smaller than from the mega-analysis. In the mega-analysis results, there are a lot of voxels at the edge of the brain show significance for the age^2 and sex effect. This may because that the covariate has an effect on the shape of the brain some subjects have value on these voxels while subjects not.

The relationships of the mega- and meta-analysis are displayed in **Figure 6.9**. When we performed the analysis we did not provide any explicit brain mask, but only used the implicit brain mask calculated by SPM8. After analysis, SPM8 will output a brain mask. Here the brain mask from the mega-

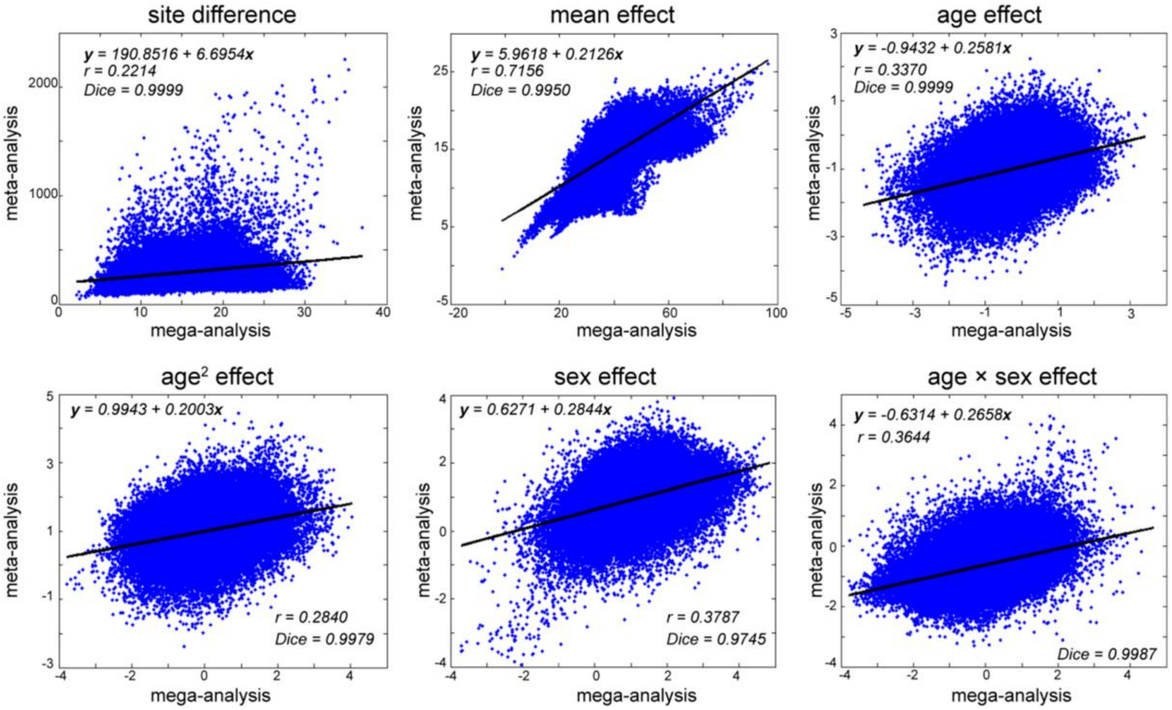

Figure 6.9 Relationship of the results from mega- and meta-analysis on LH functional connectivity maps. The x-axis represents the statistical value from the mega-analysis (F-statistics for site difference, T-statistics for covariates). The y-axis represents the statistical value from the meta-analysis (Chi-squared statistics for site difference, T-statistics for covariates). The blue dots are voxels within the brain mask, and the black lines are linear regression line regressing the meta-analysis statistical value on the mega-analysis statistical value. The r value shown on the plots are the correlation value and the Dice is the Dice coefficient of the significance maps.

analysis is larger than the brain mask calculated from the meta-analysis, thus we explored their relationship within the brain mask calculating from the meta-analysis. The correlations of the mega- and meta-analysis are not high for each statistical test but the Dice coefficients are high for all tests.

Multi-site Inference on Structure-Function Relationships

In recent years, the structure function relationships have attracted more and more attentions in understanding how the human brain works. With the gray matter density maps and functional connectivity maps it is easy to assess their relationship using Biological Parametric Mapping (BPM) (Casanova, Srikanth et al. 2007). Here we use BPM to explore the question that how the gray matter density maps explain the left hippocampus connectivity maps. We analyzed their relationship using similar GLMs described in equation (6.8) and equation (6.9) for mega- and meta-analysis. The LH functional connectivity maps were analyzed as regressand and the GM maps were included as another regressor. BPM enables the analysis of multi-modality brain images; however, BPM is sensitive to outliers. This problem can be overcome through robust regression, the robust version of BPM (rBPM) has been introduced and demonstrated to be reliable to outliers (Yang, Beason-Held et al. 2011). Although obvious outliers are discarded in the data quality assessment, it is very possible some outlier observations are included in the analysis. It is hardly to discard all problematic data automatically. Besides, the mis-registrations in the voxel level are hard to see even if we manually check every registered image. Therefore, the reliability of rBPM to outliers will be very helpful in the structure function relationship studies. Herein, we analyzed the relationships between the smoothed GM maps and LH functional connectivity maps using BPM and rBPM.

The significance of the mean effect and the GM effect are shown in **Figure 6.10**. Other covariates effects are small compared to these two effects and not shown here. The significance maps are calculated under FWE corrected p-value threshold at $p < 0.05$. One dimension of the glass brain and one slice of the significant t-map overlaid with the corresponding GM map are shown. In the BPM and rBPM analysis, we did not provide any explicit brain mask but an implicit brain mask was calculated based on the number of nonzero observations. Because the brain mask calculated from the meta-analysis are much smaller than from the mega-analysis, a lot of significant mean effect voxels in the mega-analysis are missing in the meta-analysis. The left and right hippocampus are the most significant mean effect regions in both mega- and meta-analysis, which is consistent with the functional connectivity analysis. Most of the significant regions from BPM and rBPM analysis are similar but with some difference.

The comparison of the mega- and meta-analysis results on the structure function relationship analysis using BPM and rBPM are shown in **Figure 6.11**. The t-values for each coefficient from the

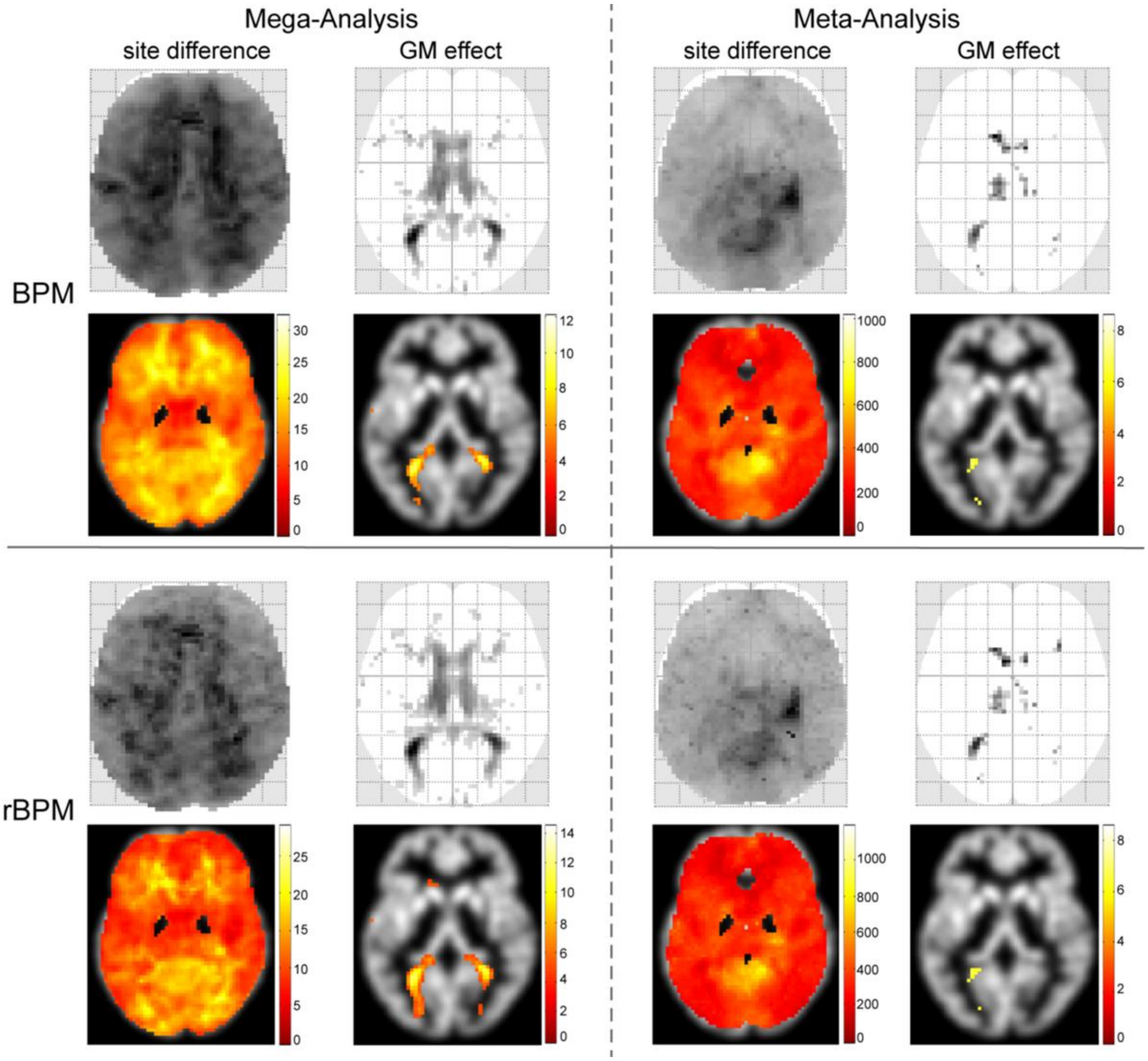

Figure 6.10 Mega- and Meta-analysis results using BPM and rBPM model. The first two rows are the results using BPM and the last two rows are the results using rBPM. The left two columns are the results from mega-analysis and the right two columns are the results from meta-analysis.

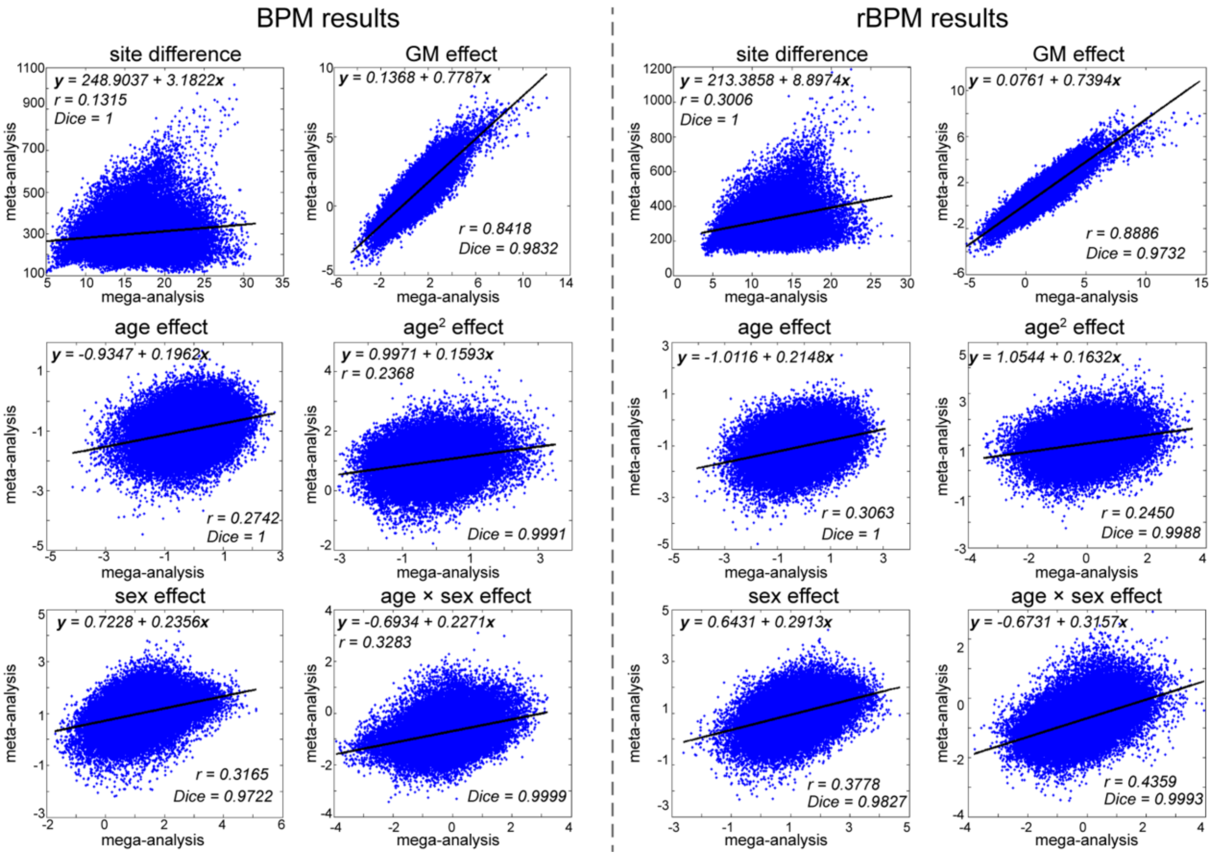

Figure 6.11 Relationship of the results from mega- and meta-analysis on structure function relationship analysis. The left two columns show the results using BPM and the right two columns show the results using rBPM. For each regressor effect, the t-value from mega- and meta-analysis are plotted (blue dots). The black lines show the regression of t-value from mega-analysis on the t-value from meta-analysis. The r value is the correlation of the mega- and meta-analysis and the Dice is the Dice coefficient of their significance maps (FWE threshold at $p < 0.05$ for mean and GM effect, uncorrected $p < 0.001$ for other effects).

mega-analysis are plotted versus the t-values from the meta-analysis within the brain mask calculating in the meta-analysis. The correlations of the mean effect and the GM effect from mega- and meta-analysis are higher than 0.5 while the correlations of other effects are low. The Dice coefficients are high for all effects (under FWE corrected p-value at $p < 0.05$ for mean and GM effects and uncorrected p-value at $p < 0.001$ for other effects). An interesting finding is that the correlations of mega- and meta-analysis results using rBPM are all slightly bigger than the corresponding correlations using BPM.

Discussion

As the sharing of multi-site studies succeeding in the genetics analysis (Mailman, Feolo et al. 2007; Jahanshad, Kochunov et al. 2013), large scale data sharing has attracted more and more attentions in the neuroimaging community (Mennes, Biswal et al. 2012). Besides the concern of protecting privacy and data organization, the challenge of handling rich datasets in an orderly and efficient way has increased. Our work presented here provides a semi-automatic method for assessing the pre-processed data quality, proves the feasibility of analyzing multi-site data using mega- and meta-analysis, and demonstrates the usefulness of robust BPM in large scale structure function relationship studies. The data qualities are varied from subject to subject as well as site to site. After dimensionality reduction using PCA, the failed registered brain images are easily to see and can be removed in following statistical analysis. Although there may still exist some subtle outliers, the data should be acceptable for large scale statistical analysis. Besides, the rBPM is reliable to outliers when the number of failed registered images is small compared to the whole dataset.

Mega-analysis and meta-analysis are two typical widely used methods in combining statistics from multi-site data. The mega-analysis is a fixed effect model ignoring the between-site variance that can be described in a simple GLM. The meta-analysis described here is a mixed effect model accounting the between-site variance that can be used for generalizing inference. From our results, we can see that the site difference exist almost everywhere in both the GM maps and the LH functional connectivity maps. According to this discovery, it seems more reasonable to account the between-site variability in analysis. When it comes to the coefficient inference, the mega-analysis always shows more significance than the meta-analysis. This proves that by accounting the between-site variance the meta-analysis can better control the type I error than the mega-analysis while may lose the power of detection. The correlations between mega- and meta-analysis in our study are high if there are large significant regions in the brain (e.g., site difference, mean effect, and GM effect) but become low if not (e.g., age effect and sex effect). The Dice coefficients, however, stays high under FWE corrected p-value threshold at $p < 0.05$ or uncorrected p-value threshold at $p < 0.001$. These results prove enough agreement between mega-analysis and meta-analysis that the statistical inferences are reliable.

The BPM and rBPM can be used with the mega- and meta-analysis for large scale structure function relationship studies. Our empirical results show higher correlation of the mega- and meta-analysis using rBPM than using BPM, which agrees with its reliability to outliers. The mis-registration problems are hard to address or identify for all data in a large database. With acceptable number of outliers, we are still able to draw inference using multi-site data. The work here proves that with mega- and meta-analysis, we can not only assess the within-modality relationship but also reliable between modality relationships using large scale datasets.

In this study, we only applied typical pre-processing pipelines implemented in SPM, other registration methods or additional process may result in interesting findings but beyond the scope of this paper. The age and sex covariates were included in our three study models because they are common findings associated with brain changes, but we did not aim to hypothesize or prove any age or sex effects. In the functional connectivity analysis, the selection of the seed region will affect results, but here we were not interested in finding or validating any hypothesis. Instead, we aim to show an example of multi-site studies on functional connectivity analysis for mega- and meta-analysis exposition. The left hippocampus was defined as the seed region because the hippocampus networks are widely studied and the age effects have been studied on this region, but other connectivity maps can be studied here. The goal of this paper is to prove that (1) the huge significance of site effect should encourage extreme caution and (2) the increased power with mega- over meta- analysis show encourage full data sharing rather than summary statistics.

CHAPTER VII

CONCLUSIONS AND FUTURE WORK

Summary

This dissertation concerns the robustness and realistic considerations of statistical models in human brain mapping within the general linear model (GLM) framework. The GLM has been widely accepted in the neuroimaging community, but problems occur as these approaches are applied to larger, multi-modal, and/or heterogeneous datasets. We focus on addressing limitations of the GLM within multi-modality brain image analysis and functional connectivity analysis. In **Chapter II**, we provide a robust model that is reliable to outliers in the structure-function relationships analysis. **Chapter III** further addressed issues in the structure-function relationships analysis and introduced models that can account for random regressors. The methods proposed in **Chapter II** and **Chapter III** were implemented in the biological parametric mapping (BPM) framework. We collaborated with neuroscientists on empirical clinical applications. One clinical application is the study of the relationship between resting state functional connectivity and gray matter concentration in temporal lobe epilepsy (Holmes, Yang et al. 2013). Another application is for the Baltimore Longitudinal Study of Aging exploring the relationships between distribution volume ratio and cerebral blood flow (Sojkova, Goh et al. 2013/09).

With the availability of alternative statistical approaches for testing the same fundamental hypotheses, deciding among statistical methods becomes a problem unto itself. Traditionally, methodological decisions have been based on asymptotic theory and simulation experiments; yet, such studies do not provide specific information regarding the appropriateness of a method for any individual dataset. We applied new innovations in finite sample statistics to provide quantitative information on the relative performance of individual (non-repeated) fMRI datasets. The SIMulation and EXtrapolation (SIMEX) approach can estimate the bias of an estimator on finite samples base on the notion that the expected value of an estimator diverges smoothly with increasing noise levels, therefore, the mean degree of corruption can be estimated by extrapolating a trend of divergence when synthetic noise is added to *empirical* data and randomized data subsampling. Motivated by this theory we proposed a quantitative evaluation method that can compare statistical inference models on empirical resting state fMRI data (**Chapter IV**). For single subject studies, ordinary least squares method outperforms robust regression on most clean 3T data while robust regression is better on some 7T data which may have relatively higher physiological noise. As is expected, no one statistical approach dominates, and selection of methods remains a nuanced decision. Yet, we have created a quantitative method to guide domain experts.

In functional connectivity studies, the time series are correlated, which has been routinely considered in statistical GLM models. However, very few models can consider the temporal correlations and the spatial correlations simultaneously in estimation. Ignoring spatial correlations may under-estimate the standard deviations that will increase false positive rates. In **Chapter V**, we extended a ROI-based spatio-spectral mixed-effects model to the whole brain resting state functional connectivity analysis. We also applied the ideas in this model to the voxel-wise models within the statistical parametric mapping (SPM) framework to take both the spatial correlations and temporal correlations into account. The benefits of the ROI-based spatio-spectral and voxel-wise spatio-temporal models for fMRI connectivity analysis were demonstrated in theory and simulations. For empirical studies, this work needs further development and characterize group level analysis for more typical study designs. Moreover, the connectivity structure estimated by this approach is potentially ground breaking, but a deeper analysis of estimatable properties and biological considerations is warranted.

Data sharing has fostered democratization of interpretation of medical images and allowed exploration by a greater pool of scientists. These efforts are typified by the 1000 functional connectomes project. In contrast to traditional small-scale studies, imaging protocols differ from site to site in the public data resources. Hence, there are substantial concerns regarding how one should perform "federated" studies – e.g., should summary measures be combined ("meta-analysis") or should all imaging data be analyzed simultaneously ("mega-analysis"). We studied the site effects using mega- and meta-analysis with 1000 functional connectomes project in **Chapter VI**. The results show substantial and significant site difference over the whole brain and much strong effects observed with mega- analysis opposed to meta-analysis. While the underlying causes of the site difference are relatively unexplored, demonstration of its existence encourages cautions of modeling site effects for multi-site studies. Further efforts are needed to investigate compensation for site difference (e.g., more robust image processing and segmentation) and modeling site differences (e.g., linear modulation versus parametric modeling of acquisition). Nevertheless, the conclusion that sharing of raw data enables more powerful science than sharing of summary statistics is well-justified.

In the following sections we detail the main results of each contribution.

Reliable Statistical Inference in Multi-modality Brain Image Analysis

Unlike traditional statistical parametric mapping, biological parametric mapping (BPM) can explain changes in one modality brain image using information from other modality brain images. During our experiments of structure-function relationship studies, we explored the problems within the traditional statistical estimation methods in the multi-modality brain image analysis. To lower the sensitivity of BPM to outliers, we proposed robust regression and non-parametric mapping methods to in inter modality brain image studies.

Main Results

1. The main difference between inter modality brain image analysis and intra modality brain image analysis is that the design matrix contains other modality brain image information. Because of this difference, (1) the possibility of the appearance of outlier increases and (2) the observation of imaging regressors are not fixed (i.e., should be treated as random variable).

2. We explored possible statistical methods to increase the reliability of BPM analysis: robust regression and non-parametric mapping. Robust regression can provide reliable estimation by lowering the influence of possible outlier observations when outlier occurs and at the same time being 95% efficient if no outliers exist. Non-parametric mapping can be used for estimation when the Gaussian distribution assumption is not reasonable or the sample size is small.
3. We demonstrated that the robust and non-parametric models are compatible with the general linear model framework and multiple comparison correction methods. They are implemented in the same pipeline as the traditional human brain mapping.
4. We evaluated application of these methods in simulation and explaining the use in empirical experiments, illustrating the usefulness in the context of BPM and multi-modality image regression.
5. We released software resources (http://www.nitrc.org/projects/rbpm/) to allow others to use these tools. These have been downloaded over 200 times (October 2013).
6. Use of the software toolbox was evaluated in two hypothesis-driven studies. In the temporal lobe epilepsy study, it was used to explore the relationship between gray matter concentrations and resting functional connectivity (hippocampus and thalamus). In longitudinal aging study, it was used to explore the relationship between distribution volume ratio and cerebral blood flow.

Future Work

The robust regression is reliable to outliers, but there are several robust weight functions, which may result in slightly different inference. The comparison of different robust weight functions can be studied to set up criteria of choice in empirical use. For more robust analysis, a robust smoothness estimation method may be useful. Although we can mitigate smoothness concerns by pooling data across images, exploring the influence for post multiple comparisons could provide more accurate corrected p-value thresholds.

Addressing Random Regressors in Multi-Modality Brain Image Analysis

The multi-modality brain image analysis requires images on images regression, where the regressors are not fixed value as most traditional models (e.g., age, sex). To more accurately model this realistic situation and provide accurate estimation, we introduced Model II regression and regression calibration that can account for the regressors with measurement error.

Main Results

1. We explored statistical models that can account for random regressors in the estimation: regression calibration and Model II regression. In simulation, we demonstrated that the regression calibration can better control the type I error and the type II error than ordinary least squares (OLS) method, but requires replicated measurements of the random regressors. The Model II regression is also better than OLS by using the measurement error ratio of the regressors to the regressand and provides symmetric estimations. In empirical studies, the measurement error ratio can be estimated through signal to noise ratio estimation, which has been widely studied in the MRI imaging community.
2. We demonstrated these models in the statistical parametric mapping framework, evaluated their applications in simulation and empirical experiments, and illustrated the usefulness in the multi-modality image analysis. With empirical data, no ground truth is available, so only differences between analyses were determined.
3. The extended BPM toolbox provides statistical methods that offer robustness to outliers and can account for regressors as random variables (http://www.nitrc.org/projects/rbpm/).

4. These proposed models can not only be used in raw brain image analysis across multiple modalities, but also in the analysis of different brain maps. For example, we can explore the relationship between the structural map and the functional connectivity map or the relationship between the changes and the baseline. With our work here, structural-functional hypothesis may be directly assessed.

Future Work

The proposed statistical model addresses the measurement error of the regressors separately, but does not directly integrate robust regression for outlier exclusion. A further research direction will be combing these two characteristics in an efficient way. For random regressors, we may work on the estimation of measurement errors. Accurately estimating the measurement error of the random regressors will increase the accuracy of the inter modality relationship estimation. Acquiring replicated measurements is a severe constraint in the neuroimaging community, but there may be special study designs for which this is an appropriate solution.

Robust Statistics and Empirical Validation in Functional Connectivity Analysis

We present a new technique to compare statistical methods using non-repeated finite samples of fMRI data. These methods provide the first quantitative data on which to compare potential statistical models using single datasets. The theoretical motivation is the novelty of SIMEX, which can estimate the expectation of an estimator on finite samples. Herein, we showed it is possible to compare statistical methods with finite empirical data where the noise structure is unknown.

Main Results

1. We investigated the model fitting residuals based on two 7T and one 3T protocols. Imaging slices that passed through regions with peak inhomogeneity problems (e.g., mid-brain

acquisitions for the 7T hippocampus) exhibited visually higher degrees of distortion along with extreme values of kurtosis (a measure of non-Gaussianity). Our early error investigation showed that artifacts in the 7T fMRI dataset had greater impact on statistical method than the 3T datasets --- such results are anecdotal, but in line with expected scanner performance given known issues of hardware stability.

2. We implemented the robust regression within the restricted maximum likelihood framework for resting state fMRI (rs-fMRI) functional connectivity analysis.
3. We proposed a novel approach for quantitatively evaluating statistical inference methods based on their resilience in the sense of diminishing data. The core theory there is similar to the SIMEX technique, but instead of adding noise to estimate the bias we diminished data to estimate the resilience. This approach can evaluate the performance on empirical data where noise structure or the truth is unknown and it does not require acquisition of additional data.
4. We demonstrated our proposed evaluation approach is consistent with type I error and type II error in simulation with known truth.
5. The studies confirmed expectations in the limited empirical datasets with known issues. Compared to OLS, the M-estimator robust regression was not needed for the clean single subject 3T fMRI analysis but resulted in superior performance metrics for the 7T dataset with artifacts.

Future Work

Our proposed method is a promising but initial work on comparing statistical inference methods on empirical data. In empirical experiments, both the true relationship and the noise structure are unknown. To satisfy the argument when simulation cannot capture empirical features, a comparison method using empirical data will accelerate the development of statistical models in human brain mapping and bring in more convincing results.

Spatial Temporal Models for Resting State fMRI Analysis

We extended a ROI-based spatio-spectral mixed-effects model for task fMRI analysis to rs-fMRI connectivity analysis. Our proposed ROI-based spatio-spectral mixed-effects model can take within-ROI and between-ROI spatial correlations as well as temporal correlations into account simultaneously. To apply this model to widely used voxel-wise analysis, we proposed a voxel-wise spatio-temporal model using a sliding window to address the within window spatial correlations as well as temporal correlations for each voxel.

Main Results

1. We extended a spatio-spectral mixed-effects model for ROI-based resting state fMRI analysis. We derived an efficient way in estimating spatial correlations and the covariance of estimated coefficients, which extends the use of this model in the whole brain functional connectivity analysis. A pipeline of the whole brain ROI-based functional connectivity analysis using spatio-spectral model was established and demonstrated through simulation and empirical experiments.
2. We proposed two voxel-wise spatio-temporal models that can account for the spatial correlations as well as the temporal correlations in rs-fMRI studies. The temporal correlations are addressed using autoregressive model with restricted maximum likelihood estimation and the spatial correlations are considered within a sliding window and estimated though variogram estimation.
3. In simulation, both the ROI-based spatio-spectral model and the voxel-wise spatio-temporal model prove to work well. Positive spatial correlation may lead to loss of the control of type I error. The proposed model improves control the type I error in such cases.
4. In empirical studies, because of the low contrast to noise ratio in the resting state fMRI data, there were no significant inference from ROI-based analysis using tradition or spatio-spectral

model. In voxel-wise analysis on an unsmoothed 7T dataset, the significant results from traditional methods are very noisy while fewer false positive voxels appear using our spatio-temporal model with voxel-wise test. These results are preliminary and should be considered inconclusive given the limited context.

Future Work

The spatial-spectral analysis demonstrates a feasible theoretical approach for handling multi-ROI analyses. The empirical study presented is exploratory and has not demonstrated the clinical/practical usefulness of this approach. Our proposed models can take the temporal and spatial correlations into account simultaneously and better control the type I error than traditional models ignoring spatial correlations in simulations. To translate these methods for clinical applications, we need to combine statistical results from these models for group analysis and conduct a study of noise sensitivity/specificity.

The voxel-wise spatial-temporal models are interesting re-posing of the estimation problem, but are relatively unexplored. The window size may affect the results and the choice needs further justification. A best window size should be able to balance the need of accurate spatial correlations estimation and the significant size, and an adaptive window for each voxel may be more appropriate. Such approaches may converge with recent perspective on spatially adaptive smoothing and more traditional GLM models.

Multi-Site Brain Image Study

We considered study design for multi-site brain mapping using mega- and meta-analysis. Over 1000 structural and resting state functional brain images were pre-processed under a typical pipeline and the data qualities were accessed using principle component analysis. We explored the site difference accounting the effects of age and sex as covariates in gray matter (GM) density analysis, functional connectivity analysis, and their relationships analysis. The correlations between mega- and meta-analysis are established and the differences are explored.

Main Results

1. This research is exploratory. The statistical methods suggest differences across sites, but we did not specifically seek to explain these differences. Continuing efforts are examining factors that lead to these site effects.
2. We explored the mega-analysis and the meta-analysis in statistical brain mapping using large scale data. The difference between mega and meta analysis are due to the fixed effects and random effects considerations. The mega-analysis is a fixed effects analysis method that can be explained in a simple general linear model. The meta-analysis can be used as a random effects analysis to infer generalized conclusions. Their correlations and differences were established in GM map analysis, left hippocampus functional connectivity map analysis, and their relationships analysis.
3. We proposed a semi-automatic data quality assessment approach to show possible outliers using Principle Component Analysis (PCA). After dimensionality reductions using PCA, the brain imaging data can be viewed together and their reconstruction errors can be evaluated. Based on a two dimensions view of the pre-processed images and their reconstruction errors using first ten eigenvectors, we were able to detect outliers and exclude them in the following statistical analysis.
4. The increased power with mega- over meta-analysis shows encourage of full data sharing rather than summary statistics.
5. We demonstrated the practical performance of our analysis toolbox software for large-datasets and multi-site studies.

Future Work

In addition to data management and organization, heterogeneous data introduces statistical challenges for big-data studies. This work focus on studying the existence of site differences using mega- and meta- inference approaches. However, the reason of the site effects is still unclear that needs further study. The contribution of our work here is drawing the attention of considering site effects in multi-site analysis. Another finding of this work is the increased power with mega- over meta-analysis. To explore more specific neuro-scientific hypotheses, we need to collaborate with neuroscientists in future studies using multi-site data. Another direction of the future work is improving the data quality assessment method to provide a quantitative and more accurate justification.

Overall Perspective

The goal of the presented work in this dissertation is to explore the robustness and accuracy in human brain mapping within a widely used statistical parametric mapping framework. Specifically, we focused on the multi-modality structural functional brain image analysis and resting state functional connectivity analysis. We demonstrated that modern statistics can be compatible with general linear model to provide reliable and accurate estimations. An evaluation method of comparing statistical inference methods on empirical data was proposed for resting state functional connectivity. For analysis using multi-site data, mega- and meta-analysis were explored and site differences were discovered. The statistical methods have shown that the differences between sites are unlikely to have occurred by chance, but the optimal approaches for compensating for such effects (post hoc or during study design) remains a challenging problem for the field. The theme of the work presented in this dissertation is from the perspective of a statistical engineer – i.e., translating statistics into practice (as opposed to statistical theory or basic science). Our contributions are explorations of appropriate statistical theories in detail for medical image analysis and the methods proposed were demonstrated in simulations. The presented empirical studies aim to explain the methods and illustrate how to use them. To gain deeper insight of the application to make our work more biomedically meaningful, we need to work with neuroscientists. To date, we have collaborated with two neuroscientists for multi-modality brain image analyses; other work will be applied in the future. We hope the work in this dissertation can attract attention to using appropriate statistical models in human brain mapping and the toolbox developed here can lead to interesting clinical research findings.

REFERENCES

Afshin-Pour, B., H. Soltanian-Zadeh, et al. (2011). "A mutual information-based metric for evaluation of fMRI data-processing approaches." Human Brain Mapping **32**(5): 699-715.

Altman, D. G. (1991). Practical statistics for medical research, CRC Press.

Antonova, E., T. Sharma, et al. (2004). "The relationship between brain structure and neurocognition in schizophrenia: a selective review." Schizophr Res **70**(2-3): 117-145.

Ashburner, J. and K. J. Friston (1999). "Nonlinear spatial normalization using basis functions." Human Brain Mapping **7**(4): 254-266.

Ashburner, J. and K. J. Friston (2000). "Voxel-based morphometry--the methods." Neuroimage **11**(6 Pt 1): 805-821.

Asman, A. J. and B. A. Landman (2012). "Formulating spatially varying performance in the statistical fusion framework." IEEE Trans Med Imaging **31**(6): 1326-1336.

Asman, A. J. and B. A. Landman (2013). "Non-local statistical label fusion for multi-atlas segmentation." Med Image Anal **17**(2): 194-208.

Bandettini, P. A., A. Jesmanowicz, et al. (1993). "Processing strategies for time-course data sets in functional MRI of the human brain." Magn Reson Med **30**(2): 161-173.

Banerjee, S., B. P. Carlin, et al. (2004). Hierarchical modeling and analysis for spatial data. Boca Raton, Fla., Chapman & Hall/CRC.

Beason-Held, L. L., M. A. Kraut, et al. (2008). "I. Longitudinal changes in aging brain function." Neurobiol Aging **29**(4): 483-496.

Beaton, A. E. and J. W. Tukey (1974). "Fitting of Power-Series, Meaning Polynomials, Illustrated on Band-Spectroscopic Data." Technometrics **16**(2): 147-185.

Becker, B. J. and M. J. Wu (2007). "The synthesis of regression slopes in meta-analysis." Statistical Science **22**(3): 414-429.

Benjamini, Y. and Y. Hochberg (1995). "Controlling the False Discovery Rate - a Practical and Powerful Approach to Multiple Testing." Journal of the Royal Statistical Society Series B-Methodological **57**(1): 289-300.

Benjamini, Y. and D. Yekutieli (2001). "The control of the false discovery rate in multiple testing under dependency." Annals of Statistics **29**(4): 1165-1188.

Biswal, B., F. Z. Yetkin, et al. (1995). "Functional connectivity in the motor cortex of resting human brain using echo-planar MRI." Magn Reson Med **34**(4): 537-541.

Biswal, B. B., M. Mennes, et al. (2010). "Toward discovery science of human brain function." Proc Natl Acad Sci U S A **107**(10): 4734-4739.

Biswal, B. B., J. Van Kylen, et al. (1997). "Simultaneous assessment of flow and BOLD signals in resting-state functional connectivity maps." NMR Biomed **10**(4-5): 165-170.

Bookstein, F. L. (2001). ""Voxel-based morphometry" should not be used with imperfectly registered images." Neuroimage **14**(6): 1454-1462.

Bradley, A. P. (1997). "The use of the area under the roc curve in the evaluation of machine learning algorithms." Pattern Recognition **30**(7): 1145-1159.

Carroll, R. J., H. Kuchenhoff, et al. (1996). "Asymptotics for the SIMEX estimator in nonlinear measurement error models." Journal of the American Statistical Association **91**(433): 242-250.

Carroll, R. J. and D. Ruppert (1996). "The use and misuse of orthogonal regression in linear errors-in-variables models." American Statistician **50**(1): 1-6.

Carroll, R. J., D. Ruppert, et al. (2010). Measurement error in nonlinear models: a modern perspective, CRC press.

Casanova, R., R. Srikanth, et al. (2007). "Biological parametric mapping: A statistical toolbox for multimodality brain image analysis." Neuroimage **34**(1): 137-143.

Chen, C. (2002). "Robust regression and outlier detection with the ROBUSTREG procedure." SUGI Paper(265-27).

Chen, X., P. S. Sachdev, et al. (2007). "Sex differences in regional gray matter in healthy individuals aged 44-48 years: a voxel-based morphometric study." Neuroimage **36**(3): 691-699.

Cook, J. R. and L. A. Stefanski (1994). "Simulation-Extrapolation Estimation in Parametric Measurement Error Models." Journal of the American Statistical Association **89**(428): 1314-1328.

Cordes, D., V. M. Haughton, et al. (2000). "Mapping functionally related regions of brain with functional connectivity MR imaging." AJNR Am J Neuroradiol **21**(9): 1636-1644.

Delong, E. R., D. M. Delong, et al. (1988). "Comparing the Areas under 2 or More Correlated Receiver Operating Characteristic Curves - a Nonparametric Approach." Biometrics **44**(3): 837-845.

Deming, W. E. (1943). "Statistical adjustment of data."

Diedrichsen, J. and R. Shadmehr (2005). "Detecting and adjusting for artifacts in fMRI time series data." Neuroimage **27**(3): 624-634.

Dubin, R. A. (1988). "Estimation of regression coefficients in the presence of spatially autocorrelated error terms." The Review of Economics and Statistics: 466-474.

Dumouchel, W. and F. O'Brien (1991). "Integrating a robust option into a multiple regression computing environment." Institute for Mathematics and Its Applications **36**: 41.

Etkin, A. and T. D. Wager (2007). "Functional neuroimaging of anxiety: a meta-analysis of emotional processing in PTSD, social anxiety disorder, and specific phobia." Am J Psychiatry **164**(10): 1476-1488.

Fisher, R. A. (1925). "Applications of Student's Distribution." Metron **5**: 90-104.

Fox, J. (2002). An R and S-Plus companion to applied regression, Sage.

Fox, P. T., M. A. Mintun, et al. (1986). "Mapping human visual cortex with positron emission tomography." Nature **323**(6091): 806-809.

Friston, K., P. Jezzard, et al. (1994). "Analysis of functional MRI time-series." Human Brain Mapping **1**(2): 153-171.

Friston, K. J., J. T. Ashburner, et al. (2007). Statistical Parametric Mapping: The Analysis of Functional Brain Images, Academic Press.

Friston, K. J., C. D. Frith, et al. (1990). "The Relationship between Global and Local Changes in Pet Scans." Journal of Cerebral Blood Flow and Metabolism **10**(4): 458-466.

Friston, K. J., C. D. Frith, et al. (1991). "Comparing functional (PET) images: the assessment of significant change." J Cereb Blood Flow Metab **11**(4): 690-699.

Friston, K. J., D. E. Glaser, et al. (2002). "Classical and Bayesian inference in neuroimaging: applications." Neuroimage **16**(2): 484-512.

Friston, K. J., A. P. Holmes, et al. (1995). "Analysis of fMRI time-series revisited." Neuroimage **2**(1): 45-53.

Friston, K. J., A. P. Holmes, et al. (1994). "Statistical parametric maps in functional imaging: a general linear approach." Human Brain Mapping **2**(4): 189-210.

Friston, K. J., W. Penny, et al. (2002). "Classical and Bayesian inference in neuroimaging: theory." Neuroimage **16**(2): 465-483.

Friston, K. J., S. Williams, et al. (1996). "Movement-related effects in fMRI time-series." Magn Reson Med **35**(3): 346-355.

Garrett, M. A., H. T. Holmes, et al. (1992). "Selective buffered charcoal-yeast extract medium for isolation of nocardiae from mixed cultures." J Clin Microbiol **30**(7): 1891-1892.

Genovese, C. R., D. C. Noll, et al. (1997). "Estimating test-retest reliability in functional MR imaging. I: Statistical methodology." Magn Reson Med **38**(3): 497-507.

Gerber, S., T. Tasdizen, et al. (2010). "Manifold modeling for brain population analysis." Med Image Anal **14**(5): 643-653.

Gill, P. S. (2000). "A robust mixed linear model analysis for longitudinal data." Stat Med **19**(7): 975-987.

Giove, F., G. Garreffa, et al. (2004). "Issues about the fMRI of the human spinal cord." Magn Reson Imaging **22**(10): 1505-1516.

Grady, C. L., J. M. Maisog, et al. (1994). "Age-related changes in cortical blood flow activation during visual processing of faces and location." J Neurosci **14**(3 Pt 2): 1450-1462.

Greicius, M. D., B. Krasnow, et al. (2003). "Functional connectivity in the resting brain: a network analysis of the default mode hypothesis." Proc Natl Acad Sci U S A **100**(1): 253-258.

Gudbjartsson, H. and S. Patz (1995). "The Rician distribution of noisy MRI data." Magn Reson Med **34**(6): 910-914.

Hedges, L. V. and T. D. Pigott (2004). "The power of statistical tests for moderators in meta-analysis." Psychol Methods **9**(4): 426-445.

Holland, P. W. and R. E. Welsch (1977). "Robust Regression Using Iteratively Re-Weighted Least-Squares." Communications in Statistics Part a-Theory and Methods **6**(9): 813-827.

Holmes, A. and K. Friston (1998). "Generalisability, Random Effects & Population Inference." Neuroimage **7**: S754.

Holmes, A. P. (1994). "Statistical issues in functional brain mapping."

Holmes, A. P., R. C. Blair, et al. (1996). "Nonparametric analysis of statistic images from functional mapping experiments." J Cereb Blood Flow Metab **16**(1): 7-22.

Holmes, M. J., X. Yang, et al. (2013). "Functional networks in temporal-lobe epilepsy: a voxel-wise study of resting-state functional connectivity and gray-matter concentration." Brain Connect **3**(1): 22-30.

Honey, C. J., J. P. Thivierge, et al. (2010). "Can structure predict function in the human brain?" Neuroimage **52**(3): 766-776.

Huber, P. J. (1964). "Robust estimation of a location parameter." The Annals of Mathematical Statistics **35**(1): 73-101.

Huber, P. J. (1973). "1972 Wald Memorial Lectures - Robust Regression - Asymptotics, Conjectures and Monte-Carlo." Annals of Statistics **1**(5): 799-821.

Huber, P. J. (2002). "John W. Tukey's contributions to robust statistics." Annals of Statistics **30**(6): 1640-1648.

Huber, P. J. and E. M. Ronchetti (1981). Robust statistics, Wiley, New York.

Hutchison, R. M., L. S. Leung, et al. (2011). "Resting-state networks in the macaque at 7 T." Neuroimage **56**(3): 1546-1555.

Hutton, C., O. Josephs, et al. (2011). "The impact of physiological noise correction on fMRI at 7 T." Neuroimage **57**(1): 101-112.

Jahanshad, N., P. V. Kochunov, et al. (2013). "Multi-site genetic analysis of diffusion images and voxelwise heritability analysis: A pilot project of the ENIGMA-DTI working group." Neuroimage **81**: 455-469.

Jensen, K. B., P. Srinivasan, et al. (2013). "Overlapping structural and functional brain changes in patients with long-term exposure to fibromyalgia." Arthritis Rheum.

Kang, H., H. Ombao, et al. (2012). "Spatio-Spectral Mixed-Effects Model for Functional Magnetic Resonance Imaging Data." Journal of the American Statistical Association **107**(498): 568-577.

Kang, H., X. Yang, et al. (2013). Whole Brain Functional Connectivity Using Multi-scale Spatio-Spectral Random Effects Model. MICCAI 2013 Workshop of Multimodal Brain Image Analysis. Nagoya, Japan.

Kaufman, J. and D. Charney (2001). "Effects of early stress on brain structure and function: implications for understanding the relationship between child maltreatment and depression." Dev Psychopathol **13**(3): 451-471.

Konstantopoulos, S. (2006). Fixed and mixed effects models in meta-analysis. Discussion paper no 2198. Bonn, Germany, IZA,.

Kruger, G. and G. H. Glover (2001). "Physiological noise in oxygenation-sensitive magnetic resonance imaging." Magn Reson Med **46**(4): 631-637.

Kuchenhoff, H., S. M. Mwalili, et al. (2006). "A general method for dealing with misclassification in regression: the misclassification SIMEX." Biometrics **62**(1): 85-96.

LaConte, S., J. Anderson, et al. (2003). "The evaluation of preprocessing choices in single-subject BOLD fMRI using NPAIRS performance metrics." Neuroimage **18**(1): 10-27.

Landman, B. A., X. Yang, et al. (2012). Do We Really Need Robust and Alternative Inference Methods for Brain MRI? MICCAI 2012 Workshop of Multimodal Brain Image Analysis, Nice, France.

Lark, R. M. and B. R. Cullis (2004). "Model-based analysis using REML for inference from systematically sampled data on soil." European Journal of Soil Science **55**(4): 799-813.

Lauzon, C. B., C. Crainiceanu, et al. (2013). "Assessment of bias in experimentally measured diffusion tensor imaging parameters using SIMEX." Magn Reson Med **69**(3): 891-902.

Lowe, M. J., M. Dzemidzic, et al. (2000). "Correlations in low-frequency BOLD fluctuations reflect cortico-cortical connections." Neuroimage **12**(5): 582-587.

Ludbrook, J. (2010). "Linear regression analysis for comparing two measurers or methods of measurement: But which regression?" Clinical and Experimental Pharmacology and Physiology **37**(7): 692-699.

Lueck, C. J., S. Zeki, et al. (1989). "The colour centre in the cerebral cortex of man." Nature **340**(6232): 386-389.

Luerding, R., T. Weigand, et al. (2008). "Working memory performance is correlated with local brain morphology in the medial frontal and anterior cingulate cortex in fibromyalgia patients: structural correlates of pain-cognition interaction." Brain **131**(Pt 12): 3222-3231.

Luo, W. L. and T. E. Nichols (2003). "Diagnosis and exploration of massively univariate neuroimaging models." Neuroimage **19**(3): 1014-1032.

Mailman, M. D., M. Feolo, et al. (2007). "The NCBI dbGaP database of genotypes and phenotypes." Nat Genet **39**(10): 1181-1186.

Matthews, P. M., G. D. Honey, et al. (2006). "Applications of fMRI in translational medicine and clinical practice." Nat Rev Neurosci **7**(9): 732-744.

Meier, T. B., A. S. Desphande, et al. (2012). "Support vector machine classification and characterization of age-related reorganization of functional brain networks." Neuroimage **60**(1): 601-613.

Mennes, M., B. B. Biswal, et al. (2012). "Making data sharing work: The FCP/INDI experience." Neuroimage.

Neves, G., S. F. Cooke, et al. (2008). "Synaptic plasticity, memory and the hippocampus: a neural network approach to causality." Nat Rev Neurosci **9**(1): 65-75.

Newton, A. T., B. P. Rogers, et al. (2012). "Improving measurement of functional connectivity through decreasing partial volume effects at 7 T." Neuroimage **59**(3): 2511-2517.

Nichols, T. E. and A. P. Holmes (2002). "Nonparametric permutation tests for functional neuroimaging: a primer with examples." Human Brain Mapping **15**(1): 1-25.

Oakes, T. R., A. S. Fox, et al. (2007). "Integrating VBM into the General Linear Model with voxelwise anatomical covariates." Neuroimage **34**(2): 500-508.

Press, W. H. (2007). Numerical recipes: The art of scientific computing, Cambridge university press.

Rajan, J., D. Poot, et al. (2010). "Noise measurement from magnitude MRI using local estimates of variance and skewness." Phys Med Biol **55**(16): N441-449.

Resnick, S. M., A. F. Goldszal, et al. (2000). "One-year age changes in MRI brain volumes in older adults." Cereb Cortex **10**(5): 464-472.

Ripke, S., N. R. Wray, et al. (2013). "A mega-analysis of genome-wide association studies for major depressive disorder." Mol Psychiatry **18**(4): 497-511.

Rousseeuw, P. J. (1984). "Least Median of Squares Regression." Journal of the American Statistical Association **79**(388): 871-880.

Rousseeuw, P. J. and V. J. Yohai (1984). Robust regression by means of S-estimators. Robust and nonlinear time series analysis, Springer**:** 256-272.

Rowe, D. B. (2005). "Parameter estimation in the magnitude-only and complex-valued fMRI data models." Neuroimage **25**(4): 1124-1132.

Rubinov, M. and O. Sporns (2011). "Weight-conserving characterization of complex functional brain networks." Neuroimage **56**(4): 2068-2079.

Rubinov, M., O. Sporns, et al. (2009). "Symbiotic relationship between brain structure and dynamics." BMC Neurosci **10**: 55.

Scheffe, H. (1999). The analysis of variance, Wiley. com.

Seifuddin, F., P. B. Mahon, et al. (2012). "Meta-analysis of genetic association studies on bipolar disorder." Am J Med Genet B Neuropsychiatr Genet **159B**(5): 508-518.

Serretti, A., C. Cusin, et al. (2006). "Pooling pharmacogenetic studies on the serotonin transporter: a mega-analysis." Psychiatry Res **145**(1): 61-65.

Shehzad, Z., A. M. Kelly, et al. (2009). "The resting brain: unconstrained yet reliable." Cereb Cortex **19**(10): 2209-2229.

Sojkova, J., J. Goh, et al. (2013/09). "Voxel-wise relationships between Distribution Volume Ratio and cerebral blood flow: implications for interpretation of β-amyloid images." Journal of Nuclear Medicine.

Street, J. O., R. J. Carroll, et al. (1988). "A Note on Computing Robust Regression Estimates Via Iteratively Reweighted Least-Squares." American Statistician **42**(2): 152-154.

Strother, S., S. La Conte, et al. (2004). "Optimizing the fMRI data-processing pipeline using prediction and reproducibility performance metrics: I. A preliminary group analysis." Neuroimage **23 Suppl 1**: S196-207.

Strother, S. C., J. Anderson, et al. (2002). "The quantitative evaluation of functional neuroimaging experiments: the NPAIRS data analysis framework." Neuroimage **15**(4): 747-771.

Takashima, A., I. L. Nieuwenhuis, et al. (2009). "Shift from hippocampal to neocortical centered retrieval network with consolidation." J Neurosci **29**(32): 10087-10093.

Thomas, C. G., R. A. Harshman, et al. (2002). "Noise reduction in BOLD-based fMRI using component analysis." Neuroimage **17**(3): 1521-1537.

Tomasi, D. and N. D. Volkow (2011). "Functional connectivity hubs in the human brain." Neuroimage **57**(3): 908-917.

Triantafyllou, C., R. D. Hoge, et al. (2005). "Comparison of physiological noise at 1.5 T, 3 T and 7 T and optimization of fMRI acquisition parameters." Neuroimage **26**(1): 243-250.

Turk, M. and A. Pentland (1991). "Eigenfaces for recognition." J Cogn Neurosci **3**(1): 71-86.

Van de Moortele, P. F., B. Cerf, et al. (1997). "Latencies in fMRI time-series: effect of slice acquisition order and perception." NMR Biomed **10**(4-5): 230-236.

van den Heuvel, M. P. and H. E. Hulshoff Pol (2010). "Exploring the brain network: a review on resting-state fMRI functional connectivity." Eur Neuropsychopharmacol **20**(8): 519-534.

Van Horn, J. D. and M. S. Gazzaniga (2002). "Opinion: Databasing fMRI studies towards a 'discovery science' of brain function." Nat Rev Neurosci **3**(4): 314-318.

Van Horn, J. D., S. T. Grafton, et al. (2004). "Sharing neuroimaging studies of human cognition." Nat Neurosci **7**(5): 473-481.

Van Horn, J. D., J. S. Grethe, et al. (2001). "The Functional Magnetic Resonance Imaging Data Center (fMRIDC): the challenges and rewards of large-scale databasing of neuroimaging studies." Philos Trans R Soc Lond B Biol Sci **356**(1412): 1323-1339.

van Houwelingen, H. C., L. R. Arends, et al. (2002). "Advanced methods in meta-analysis: multivariate approach and meta-regression." Stat Med **21**(4): 589-624.

Wellington, R. L., R. M. Bilder, et al. (2013). "Effects of age on prefrontal subregions and hippocampal volumes in young and middle-aged healthy humans." Human Brain Mapping **34**(9): 2129-2140.

Wink, A. M. and J. B. Roerdink (2006). "BOLD Noise Assumptions in fMRI." Int J Biomed Imaging **2006**: 12014.

Worsley, K. J. (1994). "Local Maxima and the Expected Euler Characteristic of Excursion Sets of Chi(2), F and T Fields." Advances in Applied Probability **26**(1): 13-42.

Worsley, K. J., A. C. Evans, et al. (1992). "A three-dimensional statistical analysis for CBF activation studies in human brain." J Cereb Blood Flow Metab **12**(6): 900-918.

Worsley, K. J. and K. J. Friston (1995). "Analysis of fMRI time-series revisited--again." Neuroimage **2**(3): 173-181.

Worsley, K. J., C. H. Liao, et al. (2002). "A general statistical analysis for fMRI data." Neuroimage **15**(1): 1-15.

Worsley, K. J., S. Marrett, et al. (1996). "A unified statistical approach for determining significant signals in images of cerebral activation." Human Brain Mapping **4**(1): 58-73.

Worsley, K. J., J. E. Taylor, et al. (2004). "Unified univariate and multivariate random field theory." Neuroimage **23 Suppl 1**: S189-195.

Xu, Y., D. J. Valentino, et al. (2008). "Age effects on hippocampal structural changes in old men: the HAAS." Neuroimage **40**(3): 1003-1015.

Yan, C. G., R. C. Craddock, et al. (2013). "Standardizing the intrinsic brain: Towards robust measurement of inter-individual variation in 1000 functional connectomes." Neuroimage **80**: 246-262.

Yang, X., L. Beason-Held, et al. (2011). "Biological parametric mapping with robust and non-parametric statistics." Neuroimage **57**(2): 423-430.

Yang, X., L. Beason-Held, et al. (2011). Robust Biological Parametric Mapping: An Improved Technique for Multimodal Brain Image Analysis. SPIE Medical Imaging Conference, Lake Buena Vista, Florida.

Yang, X., M. J. Holmes, et al. (2012). A Comparison of Distributional Considerations with Statistical Analysis of Resting State fMRI at 3T and 7T. SPIE Medical Imaging Conference, San Diego, California.

Yang, X., H. Kang, et al. (2012). "Quantitative evaluation of statistical inference in resting state functional MRI." Med Image Comput Comput Assist Interv **15**(Pt 2): 246-253.

Yang, X., H. Kang, et al. (2013). "Evaluation of Statistical Inference on Empirical Resting State fMRI." IEEE Transactions on Biomedical Engineering.

Yang, X., C. B. Lauzon, et al. (2011). Accounting for Random Regressors: A Unified Approach to Multi-modality Imaging. MICCAI 2011 Workshop of Multimodal Brain Image Analysis. Toronto, Canada.

Yang, X., C. B. Lauzon, et al. (2012). "Biological parametric mapping accounting for random regressors with regression calibration and model II regression." Neuroimage **62**(3): 1761-1768.

Yekutieli, D. and Y. Benjamini (1999). "Resampling-based false discovery rate controlling multiple test procedures for correlated test statistics." Journal of Statistical Planning and Inference **82**(1-2): 171-196.

Yohai, V. J. (1987). "High Breakdown-Point and High-Efficiency Robust Estimates for Regression." Annals of Statistics **15**(2): 642-656.

York, D. (1966). "Least-Squares Fitting of a Straight Line." Canadian Journal of Physics **44**(5): 1079-&.

Zatorre, R. J., P. Belin, et al. (2002). "Structure and function of auditory cortex: music and speech." Trends Cogn Sci **6**(1): 37-46.

Zhu, H., Y. Li, et al. (2009). "Regression Models for Identifying Noise Sources in Magnetic Resonance Images." Journal of the American Statistical Association **104**(486): 623-637.

Zweig, M. H. and G. Campbell (1993). "Receiver-operating characteristic (ROC) plots: a fundamental evaluation tool in clinical medicine." Clin Chem **39**(4): 561-577.